

# UC Berkeley

## UC Berkeley Electronic Theses and Dissertations

### Title

Highly Mismatched Semiconductor Alloys with Extreme Compositions

### Permalink

<https://escholarship.org/uc/item/6r31n76m>

### Author

Levander, Alejandro X.

### Publication Date

2012

Peer reviewed|Thesis/dissertation

Highly Mismatched Semiconductor Alloys with Extreme Compositions

By

Alejandro Xavier Levander

A dissertation submitted in partial satisfaction of the

requirements for the degree of

Doctor of Philosophy

in

Engineering – Materials Science and Engineering

in the

Graduate Division

of the

University of California, Berkeley

Committee in charge:

Professor Junqiao Wu, Co-chair  
Professor Oscar D. Dubon, Co-chair  
Professor Peter Hosemann

Spring 2012



## Abstract

### Highly Mismatched Semiconductor Alloys with Extreme Compositions

by

Alejandro Xavier Levander

Doctor of Philosophy in Engineering – Materials Science and Engineering

University of California, Berkeley

Professor Junqiao Wu, Co-chair

Professor Oscar D. Dubon, Co-chair

Semiconductor alloying is a common method for tailoring material properties such as band gap and lattice constant for specific applications. The most common semiconductor alloys are composed of elements that are relatively well matched in terms of atom size and electronegativity. However, there is a class of semiconductors known as highly mismatched alloys (HMAs), which contain elements with very different properties. These alloys are generally difficult to synthesize due to large miscibility gaps, but can have useful and interesting properties. Recently, the HMA  $\text{GaN}_{1-x}\text{As}_x$  has been grown across the entire composition range by low-temperature molecular beam epitaxy. Over a large composition range ( $0.15 < x < 0.75$ ) these alloys are amorphous with band gaps spanning from 0.7 to 3.4 eV for the entire alloy system. Here, the thermal stability, electrical properties, and local structure of a- $\text{GaN}_{1-x}\text{As}_x$  are investigated. In addition, the extensibility of low-temperature molecular beam epitaxy is tested in the context of the significantly more mismatched  $\text{GaN}_{1-x}\text{Bi}_x$  system.

Thermal annealing experiments show that the a- $\text{GaN}_{1-x}\text{As}_x$  alloys demonstrate remarkable stability. Control of the electronic properties was difficult to attain without creating a mixed phase material. The disordered local structure of a- $\text{GaN}_{1-x}\text{As}_x$  determined by extended x-ray absorption fine structure analysis revealed a significant concentration of As dangling bonds compared to N dangling bonds. The extremely mismatched alloy GaN<sub>1-x</sub>Bi<sub>x</sub> has been grown and a significant monotonic band gap shift occurred with increasing Bi content. Soft x-ray absorption and emission reveal the hybridization of N states with Bi resulting in a density of states modification suggesting that an alloy has indeed been synthesized.

# Table of Contents

<b>List of Figures .....</b>	<b>ii</b>
<b>List of Tables.....</b>	<b>vii</b>
<b>List of Symbols and Abbreviations .....</b>	<b>viii</b>
<b>1 Introduction .....</b>	<b>1</b>
1.1 Highly mismatched semiconductor alloys.....	1
1.2 Amorphous highly mismatched alloys.....	2
<b>2 Thermal stability of amorphous GaNAs .....</b>	<b>7</b>
2.1 Furnace and rapid thermal annealing .....	7
2.2 Laser annealing .....	13
<b>3 Electronic properties of amorphous GaNAs.....</b>	<b>22</b>
<b>4 Local structure of GaNAs.....</b>	<b>33</b>
<b>5 Amorphous GaN<sub>1-x</sub>Bi<sub>x</sub>.....</b>	<b>44</b>
5.1 Growth and structure.....	44
5.2 Optical and electrical properties .....	50
<b>6 Conclusions and Outlook.....</b>	<b>60</b>
<b>7 Appendix .....</b>	<b>61</b>
7.1 Effects of point defects on thermal and thermoelectric properties of InN.....	61
7.2 Mathematica calculations for thermal conductivity modeling .....	66
7.3 Junction thermoelectrics: silicon-nickel superlattice .....	69
<b>8 References .....</b>	<b>73</b>

## List of Figures

- Fig 1.1 Band gap of  $\text{GaN}_{1-x}\text{As}_x$  as a function of GaAs mole fraction,  $x$ . Experimental values on the dilute end points of the alloy system are shown by blue or red dots. Dashed lines show theoretical calculations using the VCA theory and a quadratic fit forced to the experimental values with a fitting parameter of  $b = 16.2$  eV. The solid red line is the band anti-crossing model fit to experimental values with the dashed red corresponding to a linear interpolation of the BAC model across the composition range (Uesugi, 1999; Wu, 2004; Yu, 2009). 2
- Fig 1.2 SAD patterns for a series of  $\text{GaN}_{1-x}\text{As}_x$  alloy samples across the composition range grown at different temperatures. In the intermediate composition range, the diffuse rings correspond to an amorphous material (Yu, 2009). 3
- Fig 1.3 Photomodulated reflectance spectra of a- $\text{GaN}_{1-x}\text{As}_x$  samples with different compositions. The inset compares a PR and UV-Vis absorption spectra showing the coincidence of the PR signal and absorption edge onset (Yu, 2010). 4
- Fig 1.4 The intensity of solar irradiance as a function of energy (left). The band gap of  $\text{GaN}_{1-x}\text{As}_x$  as a function of composition across the composition range with multiple data sets including crystalline and amorphous  $\text{GaN}_{1-x}\text{As}_x$  grown on sapphire, Pyrex glass, or silicon substrates. 5
- Fig 1.5 The conduction and valence band edges of crystalline and amorphous  $\text{GaN}_{1-x}\text{As}_x$  as a function of composition as determined by XAS and SXE, plotted with the predictions for these values from the band anti-crossing and virtual crystal approximation models. The  $\text{H}_2/\text{O}_2$  redox potentials are included due to their importance for applications in water splitting (Yu, 2010). 6
- Fig 2.1 RBS spectra for as-grown  $\text{GaN}_{0.43}\text{As}_{0.57}$  (black) and 850°C-20sec RTA  $\text{GaN}_{0.43}\text{As}_{0.57}$  (red). The RTA resulted in a reduction of As in the surface region and an overall reduction in film thickness. 8
- Fig 2.2 XRD patterns from an a- $\text{GaN}_{0.64}\text{As}_{0.36}$  film after successive RTA treatments at increasing temperature for 20 sec each, with GaAs and GaN standards. The GaAs:N (111) and GaN:As (0002) peak positions indicate phase segregation of the amorphous ternary alloy into the corresponding binary crystalline phases. 9
- Fig 2.3 SAD patterns for a- $\text{GaN}_{0.64}\text{As}_{0.36}$  as grown (a); after 850°C – 20 sec RTA (b), and after 950°C – 20 sec RTA taken close to the interface (c) (black spots from  $\text{Al}_2\text{O}_3$  substrate). Note the strong dotted pattern within the second ring due to (0002) GaN planes. (d) Cross-section of the film showing the formation of randomly distributed grains; (e) High resolution image showing formation of GaAs (larger lattice spacings) and GaN (smaller lattice spacings) crystals; (f) Z-contrast microscopy image of a GaAs grain (brighter contrast from heavier As atoms). Note twinning within the GaAs crystals in (e) and (f). 11
- Fig 2.4 Absorption spectra from as-grown and 850°C – 20 sec RTA  $\text{GaN}_{0.70}\text{As}_{0.30}$ . The shift of the absorption edge indicates the formation of a higher band gap phase. 12
- Fig 2.5 RBS spectra for a- $\text{GaN}_{0.35}\text{As}_{0.65}$  as grown (black) and subjected to different laser or thermal annealing. Note the lower intensity of the surface As signal for the 850°C – 30 sec RTA (green) sample. The laser annealed samples have a similar composition profile to the as-grown sample. 14

- Fig 2.6 Synchrotron diffraction patterns from a) as-grown a-GaN<sub>0.35</sub>As<sub>0.65</sub>, b) a-GaN<sub>0.35</sub>As<sub>0.65</sub> subject to a 850°C – 30 sec RTA, and c) a-GaN<sub>0.35</sub>As<sub>0.65</sub> laser annealed with a fluence of 0.40 J/cm<sup>2</sup>. Red indicates a high diffracted intensity. 15
- Fig 2.7 Integrated diffraction patterns for a-GaN<sub>0.35</sub>As<sub>0.65</sub> as-grown and subjected to various annealing conditions. Vertical dashed lines are given to reference the angles at which diffraction conditions are satisfied for zinc blende GaAs, wurtzite GaN, and the expected location for zinc blende GaN<sub>0.35</sub>As<sub>0.65</sub> assuming a linear interpolation of lattice constants. 16
- Fig 2.8 Integrated diffraction patterns for a-GaN<sub>0.68</sub>As<sub>0.32</sub> as grown and subjected to various annealing conditions. The large broad feature at 12-16° is due to the amorphous glass substrate. Dashed lines reference the angles at which the diffraction conditions are satisfied for zinc blende GaAs and wurtzite GaN. 17
- Fig 2.9 Integrated diffraction patterns for wurtzite GaN<sub>0.95</sub>As<sub>0.05</sub> as grown and subjected to various annealing conditions. If the material is already crystalline, the laser annealing or RTA does not have a significant affect. 18
- Fig 2.10 Low-resolution TEM images and corresponding SAD patterns (indicated by arrows) of a-GaN<sub>0.68</sub>As<sub>0.32</sub> laser annealed at a fluence of 0.38 J/cm<sup>2</sup>. Only the top ~100 nm of the thin film was melted and recrystallized by the laser annealing process. 19
- Fig 2.11 Low-resolution TEM image shown in Fig 2.10 with a corresponding high-resolution TEM image of the melted and subsequently recrystallized region of a-GaN<sub>0.68</sub>As<sub>0.32</sub>. Nanosized grains of zinc blende GaAs:N are visible with larger grains closer to the surface. 20
- Fig 2.12 Low-resolution TEM image shown in Fig 2.10 with a corresponding high-resolution TEM image of the region that was not melted by the laser annealing. Very small nanograins with diameters on the order of ~2nm are visible. 20
- Fig 3.1 Conductivity as a function of temperature for GaN<sub>0.35</sub>As<sub>0.65</sub>:Mg samples with varying Mg content given in atomic percents. The inset table gives activation energies calculated from the linear low temperature region of the curve to the right side of the dashed line (50-6K). 23
- Fig 3.2 Thermopower as a function for temperature for GaN<sub>0.35</sub>As<sub>0.65</sub>:Mg samples with varying Mg content (same samples as shown in Fig 3.1). The positive sign for Mg doped samples shows Mg behaving as an acceptor. The error bars signify the standard deviation from three measurements at a given average temperature. Higher resistance samples have larger errors due to the uncertainties in measuring small voltages across large resistances. 24
- Fig 3.3 Structural analysis of GaN<sub>0.35</sub>As<sub>0.65</sub>:Mg samples. Representative x-ray diffraction pattern of samples discussed in Fig 3.1 & Fig 3.2 (dashed) and sample grown under lower As BEP to reduce crystallinity (solid) (a). Low magnification Z-contrast transmission electron micrograph, selected area diffraction, and high-resolution TEM images of a sample discussed in Fig 3.1 & Fig 3.2 (b), (c), (d), and (e) respectively. In (b), the bright contrast is the c-GaAs:N phase shown in (e) and the dark contrast is the amorphous GaN<sub>1-x</sub>As<sub>x</sub> phase shown in (d). The diffraction pattern (c) shows a superposition of c-GaAs:N rings from (111), (220), and (311) planes indicated by 1, 2, and 3 and two broad amorphous rings indicated by arrows. 26

Fig 3.4 Arsenic content in GaN <sub>1-x</sub> As <sub>x</sub> :Mg as a function of growth temperature (blue) and As BEP (red).	27
Fig 3.5 XRD patterns from GaN <sub>1-x</sub> As <sub>x</sub> :Mg grown at different temperatures.	28
Fig 3.6 Resistivity of GaN <sub>1-x</sub> As <sub>x</sub> :Mg as a function of growth temperature.	28
Fig 3.7 XRD patterns of GaN <sub>1-x</sub> As <sub>x</sub> :Mg grown using different As BEPs. The pressures given in the legend are in Torr.	29
Fig 3.8 Resistivity of GaN <sub>1-x</sub> As <sub>x</sub> :Mg as a function of As BEP. The dashed line indicates pressures below which the samples were semi-insulating.	30
Fig 3.9 Arsenic content and III:V ratio of GaN <sub>1-x</sub> As <sub>x</sub> :Mg as a function of Ga BEP.	31
Fig 3.10 XRD patterns of GaN <sub>1-x</sub> As <sub>x</sub> :Mg as a function of Ga BEP.	32
Fig 3.11 Resistivity of GaN <sub>1-x</sub> As <sub>x</sub> :Mg as a function of Ga BEP.	32
Fig 4.1 Raw absorption coefficient data collected in transmission mode for powder c-GaAs at the As <i>K</i> edge at T = 20 K.	35
Fig 4.2 Raw absorption coefficient data collected in fluorescence mode for a thin film of a-GaN <sub>0.55</sub> As <sub>0.45</sub> on a glass substrate at the As <i>K</i> edge at T = 20 K.	35
Fig 4.3 EXAFS function data (points) extracted from absorption coefficient data weighted by $k^2$ along with fits (lines) for c-GaAs and a-GaN <sub>1-x</sub> As <sub>x</sub> at different compositions from As <i>K</i> edge data. For amorphous samples 50% of data points are shown to enhance clarity.	36
Fig 4.4 Magnitude of Fourier transform of $k^2\chi(k)$ for c-GaAs and a-GaN <sub>0.55</sub> As <sub>0.45</sub> for data (points) and fits (lines). Fitted region in <i>r</i> -space was 1-4.8 Å for c-GaAs and 1.6-2.6 Å for a-GaN <sub>0.55</sub> As <sub>0.45</sub> . For the amorphous sample, no EXAFS is detected beyond the first coordination shell.	37
Fig 4.5 Magnitude and real part of the Fourier transform of $k^2\chi(k)$ for a-GaN <sub>0.55</sub> As <sub>0.45</sub> to show quality of fit.	37
Fig 4.6 Graphical representation of key structural parameters determined by EXAFS analysis for As atom local environment.	39
Fig 4.7 EXAFS function data (points) extracted from absorption coefficient data weighted by $k^2$ along with fits (lines) for c-GaAs, c-GaN, and a-GaN <sub>1-x</sub> As <sub>x</sub> at different compositions from Ga <i>K</i> edge data. For amorphous samples 30% of data points are shown to enhance clarity.	40
Fig 4.8 Magnitude and real part of Fourier transform of $k^2\chi(k)$ for a-GaN <sub>0.55</sub> As <sub>0.45</sub> for data (points) and fits (lines). Fitted region in <i>r</i> -space was 0.8-3.1 Å. (Inset) Magnitude of Fourier transform of $k^2\chi(k)$ for c-GaN for data (points) and fit (line). Fitted region in <i>r</i> -space was 1.2-3.2 Å.	41
Fig 4.9 Graphical representation of Ga coordination number determined by EXAFS analysis for first nitrogen shell (squares) and first arsenic shell (circles). The coordination number shown is multiplied by the alloying content to determine the actual number of nitrogen or arsenic atoms bonded to a given Ga atom.	43
Fig 4.10 Graphical representation of Ga $\sigma^2$ determined by EXAFS analysis for first nitrogen shell (squares) and first arsenic shell (circles). The results suggest that there are fewer dangling bonds and less bond length disorder due to nitrogen in the amorphous alloy.	43
Fig 5.1 The bismuth composition in GaN <sub>Bi</sub> measured by RBS as a function of LT-MBE growth temperature. The III-V ratio was approximately 1:1 and the films were homogeneous in the growth direction within the resolution limit of RBS. Inset	

- contains a representative RBS spectrum for a film with  $\sim 5$  at% Bi. The blue, green, and red lines correspond to the Bi, Ga, and total simulated contributions to the spectrum. 45
- Fig 5.2 XRD patterns from the GaNBi films grown at various temperatures. Crystalline GaN with no Bi incorporated is present even at the lowest growth temperature. GaN Crystallite size as a function of growth temperature determined from peak breadth contained in inset. 46
- Fig 5.3 Cross-sectional TEM images of GaNBi films grown at 400°C or 200°C. The morphology of the crystalline GaN in the film transitions from columnar to granular as the temperature decreases. 46
- Fig 5.4 III:V ratio in GaNBi layers, defined as the atomic concentration of Ga divided by the sum of the atomic concentration of Bi and N measured by RBS as a function of Ga BEP during growth. 48
- Fig 5.5 The oxygen content in the bulk of the film as determined by resonance RBS. Note that oxygen incorporation is suppressed when RBS determined III:V  $\geq 1$ . 48
- Fig 5.6 The change in bismuth concentration as a function of Bi BEP. Even at high Bi at%, the composition profile is uniform indicating minimal segregation of Bi to the surface. 49
- Fig 5.7 (a) XRD patterns for different GaNBi samples grown at low temperature, each with a different Bi flux and therefore Bi content. No incorporation of Bi into c-GaN was detected. At higher Bi contents the GaN (0002) peak was not visible. The (b) SAD pattern shows diffuse rings, but (c) HR-TEM imaging revealed nanocrystallites  $< 5$  nm in diameter. For comparison, a (d) SAD and (e) HR-TEM image of amorphous GaN<sub>0.55</sub>As<sub>0.45</sub> grown on a glass substrate by LT-MBE is shown. Note the “salt/pepper” contrast of the HR-TEM image that is indicative of the amorphous phase. 50
- Fig 5.8 The absorption spectra for GaNBi films grown at different growth temperatures. The composition of each film is given in the figure. 51
- Fig 5.9 Optical absorption spectra as a function of Ga BEP for a series of samples grown under similar Bi BEP and growth temperature. The circles represent the absorption spectra for a LT-MBE grown GaN film. As the Ga BEP increases, the incorporation of Bi into GaNBi increases until a III:V ratio of unity is reached for the left most spectrum (triangles). 52
- Fig 5.10 Temperature dependence of the conductivity of GaNBi with varying Bi content. The room temperature conductivity increases and the conductivity temperature dependence decreases with increasing Bi content. 54
- Fig 5.11 Temperature dependence of the thermopower of GaNBi with varying Bi content. The positive value indicates holes are the majority carrier. The data for the sample with 6.5 at% Bi has more variation due to the higher resistance of the sample. 55
- Fig 5.12 The nitrogen *K*-edge SXE (left side) and total fluorescence yield XAS (right side) of GaNBi films with various Bi contents. The threshold-excited elastic emission peak near 398.5 eV was used to align the SXE spectra to the XAS. 57
- Fig 5.13 Magnified view of the SXE and XAS of GaNBi with various Bi contents highlighting the changes to the band edge positions. 57
- Fig 7.1 Thermal conductivity of InN as a function of He<sup>2+</sup> irradiation dose compared to theoretical prediction from Eq.(1). A fitting parameter of  $\beta=0.13$  was used to

correlate the SRIM-predicted indium point defect concentration and the actual phonon-scattering defect concentration. Previously reported thermal conductivities of GaN, AlN and InN are included as a reference. Inset is SRIM calculated In and N vacancy concentration as a function of depth.	62
Fig 7.2 Free electron concentration and mobility of InN as a function of He <sup>2+</sup> irradiation dose.	64
Fig 7.3 Seebeck coefficient of irradiated InN as a function of free electron concentration. The dashed lines are calculated from a non-parabolic band model of the Seebeck coefficient in the degenerate doping approximation with different <i>r</i> values.	65
Fig 7.4 Schematic of electron energy filtering in <i>n</i> -type semiconductor.	69
Fig 7.5 Energy diagram for electron energy filtering superlattice (left). <i>k</i> -space diagram showing various key energies in <i>k</i> -space and the concept of lateral momentum conservation (right).	70
Fig 7.6 Schematic of 2D top-down fabricated Si/Ni junction structure using SOI (top). SEM image of SOI trench filled with sputter deposited nickel.	71
Fig 7.7 I-V curves from S-D of Si/Ni junction structures with varying numbers of periods.	72
Fig 7.8 I-V curves of two different Si/Ni junction structures measured from S-D (filled) and S-G (empty).	72

## List of Tables

Table 2.1 A comparison of the interplanar distances measured by selected area diffraction (SAD) and XRD for  $\text{GaN}_{0.64}\text{As}_{0.36}$  after  $850^\circ\text{C}$ -20 sec RTA with the calculated power diffraction data from GaAs and GaN. The double arrow indicates one broad ring measured from the inner diameter, the strongly dotted pattern, and the outer diameter.

Table 4.1 Structural and statistical fit parameters from As *K* edge data for As-Ga distance in c-GaAs, and a- $\text{GaN}_{1-x}\text{As}_x$  at  $T = 20$  K.  $S_0^2 = 1.01$

Table 4.2 Structural and statistical fit parameters from Ga *K* edge data for Ga-N distance in c-GaN, and a- $\text{GaN}_{1-x}\text{As}_x$  at  $T = 20$  K.  $S_0^2 = 0.63$

Table 4.3 Structural and statistical fit parameters from Ga *K* edge data for Ga-As distance in c-GaAs, and a- $\text{GaN}_{1-x}\text{As}_x$  at  $T = 20$  K. Statistical parameters listed in Table II.  $S_0^2 = 0.63$

## List of Symbols and Abbreviations

$\propto$	proportional to
$\alpha_v$	volume thermal expansion coefficient
Å	angstrom
$a$	interatomic spacing
a-	amorphous phase
atm	atmosphere, unit of pressure
at%	atomic percent
$\beta$	fitting parameter used in thermal conductivity modeling
BAC	band anticrossing model
BEP	beam equivalent pressure
BZ	Brillouin zone
$\chi$	EXAFS function
$ \chi $	magnitude of EXAFS function
$\chi_v^2$	reduced chi-squared statistical parameter
c	centi-, prefix meaning $10^{-2}$
c-	crystalline phase
$C$	coupling constant
$C_v$	specific heat, volumetric
$C_{vac}$	defect concentration per unit cell volume
°C	degree centigrade, unit of temperature
CB	conduction band
CBE	conduction band edge
$\Delta$	range of values
D	dimension
$\Delta M/M$	relative change in mass for one defect per unit cell
DOS	density of states
$d\mu(E)/dE$	energy derivative of x-ray absorption coefficient
$dk$	increment of $k$
$e$	fundamental charge
eV	electronvolt
$E$	energy of incident beam (EXAFS)
$E_0$	energy of absorption edge (EXAFS)
$E_a$	activation energy
$E_b$	energy of electron-filtering barrier
$E_{Bi}$	energy of bismuth level
$E_f$	Fermi level
$E_{FS}$	Fermi stabilization energy
$E_g$	optical band gap
EXAFS	extended x-ray absorption fine structure
Fig	figure
$\gamma$	Grüneisen parameter
$\Gamma$	origin of reciprocal space
Hz	hertz, 1/sec

$\hbar$	Planks constant reduced by $2\pi$
HR-TEM	high resolution transmission electron microscopy
II-VI	compound semiconductor compound of group II and VI elements
III-V	compound semiconductor compound of group III and V elements
IV	semiconductor composed of group IV element(s)
I-V	graph with current on y-axis and voltage on x-axis
J	Joule, unit of energy
$\kappa$	thermal conductivity
$k$	electron wave vector
$k_b$	Boltzmann constant
$k_b$	Wave vector corresponding to energy barrier height
$k_f$	Fermi wave vector
$k_{x,y,z}$	$k$ -space vector in x, y, or z direction
K	Kelvin, unit of temperature
$K$	core electron shell
$\lambda$	wavelength
$l$	phonon mean free path
$\ln()$	natural log
LT-MBE	low temperature molecular beam epitaxy
$\mu$	micro, prefix meaning $10^{-6}$
$\mu(E)$	x-ray absorption coefficient as a function of energy (EXAFS)
m	meter
$m$	effective electron mass
MBE	molecular beam epitaxy
mol%	mole percent
n	nano-, prefix meaning $10^{-9}$
n	electron concentration
$N$	coordination number
$N_N$	coordination number for Ga-N bonds (EXAFS)
$N_{As}$	coordination number for Ga-As bonds (EXAFS)
$N_I$	number of independent points (EXAFS)
$\omega$	phonon frequency
$\omega_D$	Debye phonon frequency
$\Omega$	Ohm
$\Omega$	unit cell volume
$\phi$	phi, angle
$\Phi$	irradiation dose
PLM	pulsed laser melting
PLA	pulsed laser annealing
PR	photomodulated reflectance spectroscopy
q	fundamental charge
$r$	bond length (EXAFS)
$r$	power law index relating relaxation time to energy for free carriers (InN)
$R_e$	electron generation rate
$r$ -space	real space
RBS	Rutherford backscattering spectrometry

RTA	rapid thermal anneal
$\sigma$	conductivity
$\sigma^2$	Debye-Waller disorder parameter
$\sigma(T)$	conductivity as a function of temperature
S	siemens
$S_0^2$	amplitude reduction factor (EXAFS)
SAD	selected area diffraction
S-D	electrical measurement using source and drain as contacts
sec	seconds
SEM	scanning electron microscopy
S-G	electrical measurement using source and gate as contacts
SOI	silicon-on-insulator
SOS	silicon-on-sapphire
SRIM	stopping range of ions in matter, software
$S(T)$	thermopower as a function of temperature
SXE	soft x-ray emission spectroscopy
$\tau$	point defect scattering relaxation time
T	temperature
$T_g$	growth temperature
TEM	transmission electron microscopy
TDTR	time-domain thermoreflectance
$v$	acoustic phonon velocity
V	Volt
VB	valence band
VBE	valence band edge
W	watt
XRD	x-ray diffraction
XAS	x-ray absorption spectroscopy
$\xi$	Fermi energy (Seebeck calculations)
Z	atomic number
ZT	thermoelectric figure of merit

# 1 Introduction

## 1.1 Highly mismatched semiconductor alloys

Semiconductor alloying is a common method for tailoring material properties such as the lattice constant and the optical band gap for specific applications. Tuning the lattice constant allows for growth on different substrates or epilayers whereas controlling the band gap adjusts the energy at which the semiconductor absorbs or emits light. The most common semiconductor alloys are composed of elements that are relatively well matched in terms of atom size, ionicity, and electronegativity. The band gap of these well matched semiconductor alloys can be rather accurately predicted by using a linear interpolation of the end point values. This simple linear model is known as the virtual crystal approximation (VCA) (Nordheim, 1931). For less well matched semiconductor alloys, the VCA model can be modified with a quadratic bowing parameter term (Richardson, 1972; Thompson, 1967). However, there is a class of semiconductors known as highly mismatched alloys (HMAs), which contain elements with very different properties. These alloys are not well described by the VCA or bowing parameter modified models.

Over the last decade it has been well established in semiconductor science that the formation of HMAs through the isoelectronic substitution of anions with very different ion size and/or electronegativity can result in dramatic restructuring of the electronic bands. Prominent examples include dilute As-rich and N-rich  $\text{GaN}_{1-x}\text{As}_x$ ,  $\text{Ga}_{1-x}\text{In}_x\text{N}_y\text{As}_{1-y}$ , and II-VI compound semiconductor alloys  $\text{ZnTe}_{1-x}\text{S}_x$  and  $\text{ZnTe}_{1-x}\text{O}_x$  (Walukiewicz, 2000; Shan, 1999; Uesugi, 1999; Wu, 2004; Yu, 2003b). These HMAs are an important part of the overall picture of semiconductor alloys in which controlling the band gap, conduction and valence band edges, and the lattice constant for various applications is the task of semiconductor scientists and engineers. These materials are difficult to synthesize due to large miscibility gaps owing to the inherent mismatch of the anion alloying elements. For example, the equilibrium solubility of nitrogen in GaAs is in the range of  $\sim 10^{14}$  N atoms/cm<sup>3</sup> at temperatures of  $\sim 650$  °C prior to the formation of a relaxed secondary GaN phase (Ho, 1997; Zhang, 2001).

The  $\text{GaN}_{1-x}\text{As}_x$  material system is a particularly well-studied HMA. Both the As-rich and N-rich crystalline alloys have been grown and characterized. On the As-rich side, there is a very rapid decrease in the band gap at room temperature from 1.42 eV to  $\sim 0.95$  eV for  $\text{GaAs}_{0.90}\text{N}_{0.10}$ . On the N-rich side, there is an abrupt jump in the band gap from 3.4 eV to  $\sim 2.8$  eV for  $\text{GaN}_{0.99}\text{As}_{0.01}$  due to the higher absolute energy level of the As-derived valence band. The band gap continues to decrease with increasing As content to  $\sim 2.5$  eV for  $\text{GaN}_{0.93}\text{As}_{0.07}$ . As can be seen in Fig 1.1, these changes in band gap with composition are not well described by the VCA or quadratic band bowing model (with  $b=16.2$  eV providing the best fit). However, the band anti-crossing model, developed by Walukiewicz *et al.*, does provide an accurate fit. Attempts to grow  $\text{GaN}_{1-x}\text{As}_x$  in the intermediate composition ranges result in phase segregation into GaAs and GaN. The dotted red line in Fig 1.1 is a linear interpolation of the BAC model across the

composition range and provides an estimate for the expected band gap if it were possible to grow the alloy in the intermediate composition ranges.

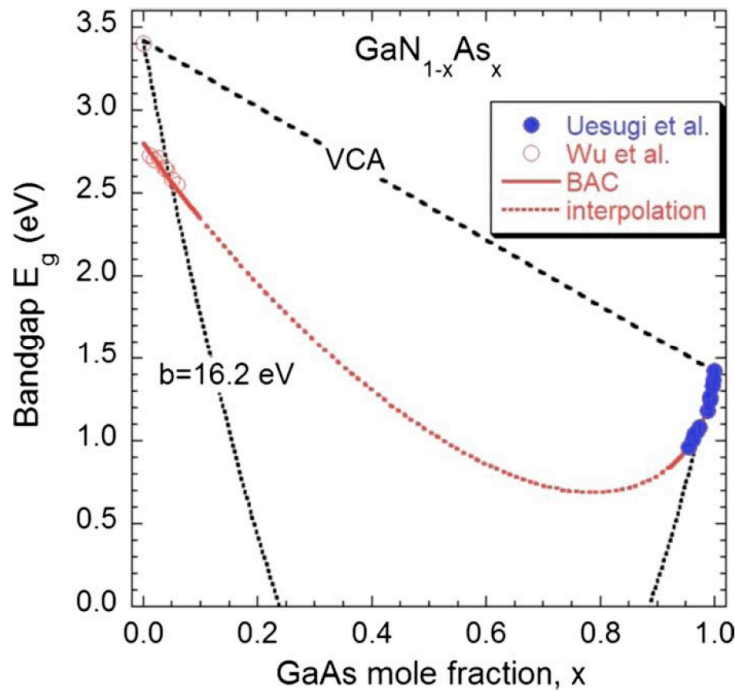


**Fig 1.1** Band gap of  $\text{GaN}_{1-x}\text{As}_x$  as a function of GaAs mole fraction,  $x$ . Experimental values on the dilute end points of the alloy system are shown by blue or red dots. Dashed lines show theoretical calculations using the VCA theory and a quadratic fit forced to the experimental values with a fitting parameter of  $b = 16.2$  eV. The solid red line is the band anti-crossing model fit to experimental values with the dashed red corresponding to a linear interpolation of the BAC model across the composition range (Uesugi, 1999; Wu, 2004; Yu, 2009).

## 1.2 Amorphous highly mismatched alloys

Due to the mismatch between As and N atoms, attempting to grow  $\text{GaN}_{1-x}\text{As}_x$  at intermediate compositions (e.g.  $x \sim 0.50$ ) at typical temperatures for high quality GaN ( $\sim 800^\circ\text{C}$ ) results in phase segregation into GaN and GaAs. However, recently it has been demonstrated that the miscibility gap of the  $\text{GaN}_{1-x}\text{As}_x$  system can be overcome by using low-temperature molecular beam epitaxy (LT-MBE) (Novikov, 2009 & 2010; Yu, 2009 & 2010). This process features a lower temperature than what is typically used for the growth of high quality nitrides. The low substrate temperature quenches adsorbed atoms and prevents them from moving to lower energy sites (e.g. phase segregated c-GaAs and c-GaN sites). For growth temperatures as low as  $\sim 100^\circ\text{C}$ , the  $\text{GaN}_{1-x}\text{As}_x$  system can be grown across the entire composition range on crystalline and amorphous substrates. Selected-area electron diffraction and high-resolution transmission electron microscopy has revealed that for  $0.10 < x < 0.75$  the resulting alloy is amorphous. Fig 1.2 shows a

series of SAD patterns from samples grown at different temperatures. The structure evolves from single crystal wurtzite GaN to polycrystalline wurtzite for dilute  $\text{GaN}_{1-x}\text{As}_x$ , to amorphous for the lowest growth temperatures and intermediate compositions. Increasing the Ga flux provides a driving force for the formation of crystalline  $\text{GaAs}_{1-x}\text{N}_x$ , and the resulting dominant structure is dilute zinc blende  $\text{c-GaAs}_{1-x}\text{N}_x$ .

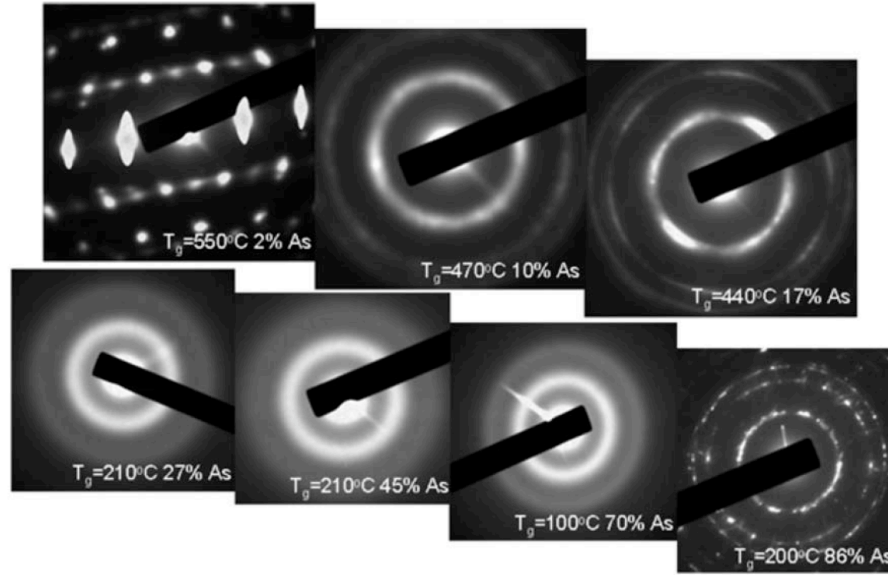


**Fig 1.2** SAD patterns for a series of  $\text{GaN}_{1-x}\text{As}_x$  alloy samples across the composition range grown at different temperatures. In the intermediate composition range, the diffuse rings correspond to an amorphous material (Yu, 2009).

Despite the structural changes in the material system, the optical band gap of the  $\text{GaN}_{1-x}\text{As}_x$  system changes monotonically with composition. The  $E_g$  can be determined using UV/Vis optical absorption spectroscopy and photo-modulated reflectance spectroscopy. Fig 1.3 shows the PR spectra from several  $\text{a-GaN}_{1-x}\text{As}_x$  with different compositions. As the arsenic content increases, the band gap shifts to lower energy as expected. The inset compares the PR and UV/Vis absorption spectra for the same sample, showing the agreement between the two techniques to determine the optical band gap. The monotonic change in band gap and the evidence for band gaps between the end point band gaps for GaN (3.4 eV) and GaAs (1.4 eV) suggest that a homogeneous ternary alloy is formed, instead of phase segregated clusters of the binary compounds.

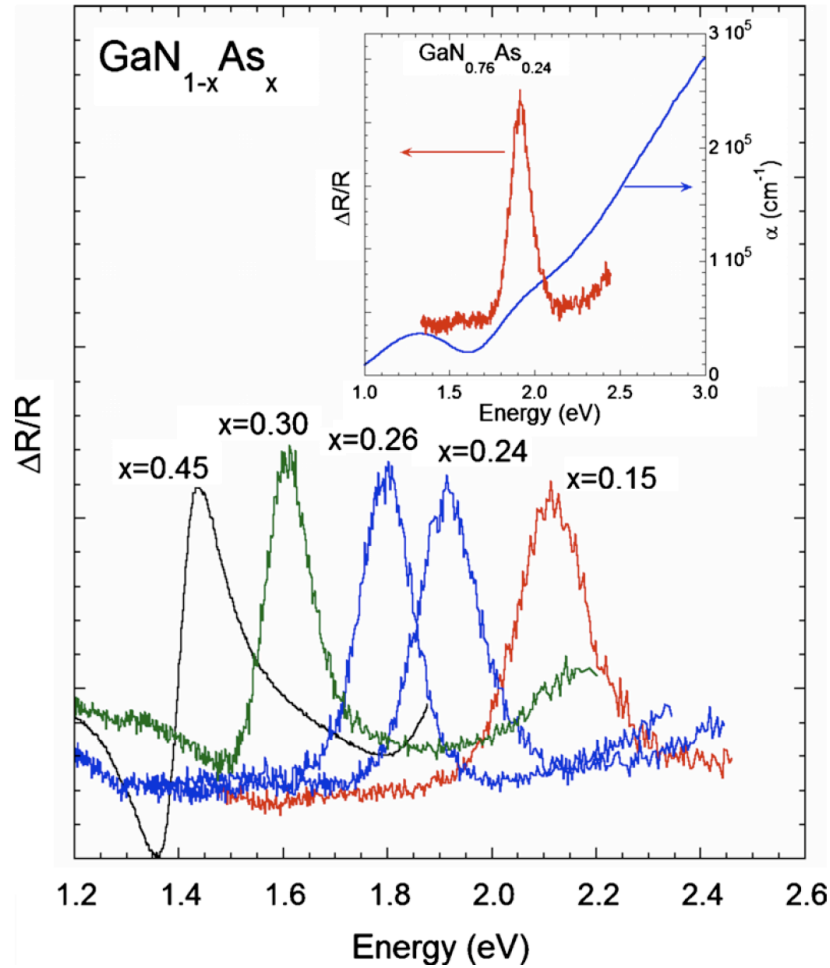


**Fig 1.3** Photomodulated reflectance spectra of a-GaN<sub>1-x</sub>As<sub>x</sub> samples with different compositions. The inset compares a PR and UV-Vis absorption spectra showing the coincidence of the PR signal and absorption edge onset (Yu, 2010).

The band gap across the entire composition range covers a wide spectral range of 0.8 eV – 3.4 eV, varying systematically with composition as shown in the right side of Fig 1.4. The band gaps accessible to the GaN<sub>1-x</sub>As<sub>x</sub> system align well with the solar spectrum, shown in the left side of Fig 1.4, which is important for potential applications to solar energy conversion. Data for As-rich and N-rich GaN<sub>1-x</sub>As<sub>x</sub> from literature (also presented in Fig 1.1) is included in Fig 1.4 for comparison. A linear interpolation of the BAC model developed to explain the dramatic band gap change for dilute As-rich and N-rich GaN<sub>1-x</sub>As<sub>x</sub> is superimposed on the E<sub>g</sub> vs. composition plot to demonstrate the qualitative agreement between the BAC model and the experimental values of the band gap across the composition range. Although the BAC model does not explicitly apply to amorphous semiconductors due to the lack of long-range order and resulting breakdown of k-space, the qualitative agreement between experimental and theoretical values demonstrates the robustness of the BAC model.

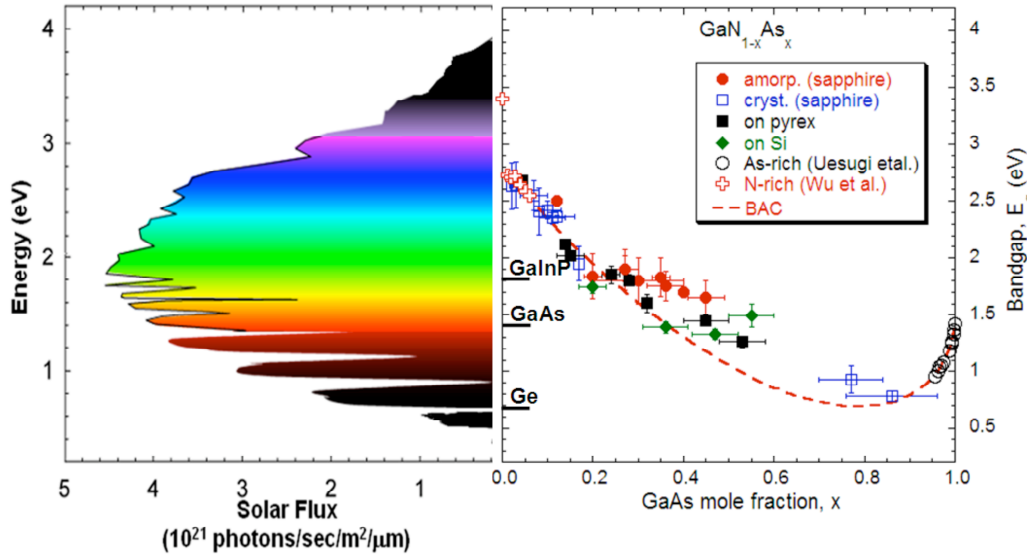


**Fig 1.4** The intensity of solar irradiance as a function of energy (left). The band gap of  $\text{GaN}_{1-x}\text{As}_x$  as a function of composition across the composition range with multiple data sets including crystalline and amorphous  $\text{GaN}_{1-x}\text{As}_x$  grown on sapphire, Pyrex glass, or silicon substrates.

The wide spectral range covered by the a- $\text{GaN}_{1-x}\text{As}_x$  alloy system lends itself to applications in multi-junction photovoltaics using a single material system. The high absorption coefficient, shown in the inset of Fig 1.3, means that only a  $\sim 1 \mu\text{m}$  thick film of material would be required for efficient light absorption. The amorphous structure and low growth temperature of the material would allow the thin films to be deposited on low cost glass or even flexible plastic substrates. Combining multiple layers of different compositions and therefore different band gaps, multi-junction photovoltaics could be fabricated to achieve higher efficiencies than a single layer cell with one band gap. For example, a two-junction cell with a 1.6 eV ( $x \sim 0.4$ ) and 0.8 eV ( $x \sim 0.8$ ) would have a theoretical efficiency of  $\sim 42\%$  under 1.5 AMO irradiation (Luque, 1997).

A different potential application for the  $\text{GaN}_{1-x}\text{As}_x$  alloy system converts solar energy into a storable fuel – hydrogen. Photoelectrochemical hydrolysis involves the absorption of solar energy to provide a driving force for the splitting of water into hydrogen and oxygen gas. A photoelectrochemical cell must meet specific requirements in order to split water efficiently: a band gap between 1.8 – 2.2 eV, corrosion stability, and band edges that straddle the hydrogen and oxygen redox potentials for spontaneous water splitting (Sorrell, 2005). Specific compositions of  $\text{GaN}_{1-x}\text{As}_x$  meet the first criteria, however in order to determine the band edges, a specific characterization technique must be used. Soft x-ray emission and x-ray absorption spectroscopies probe the valence band and conduction band edges respectively and have been performed on  $\text{GaN}_{1-x}\text{As}_x$  across the composition range (Yu, 2010). The results are shown in Fig 1.5, along with the  $\text{H}_2/\text{O}_2$  redox potentials (dotted line) and predictions for the valence band (VB) and conduction band (CB) edges from two different models (VCA and BAC). As can be seen from Fig 1.5, the composition of  $\text{GaN}_{1-x}\text{As}_x$  near  $x \sim 0.10$  meets the band gap criterion whilst

straddling the redox potentials making this material a good candidate for the study of photoelectrochemical water splitting.

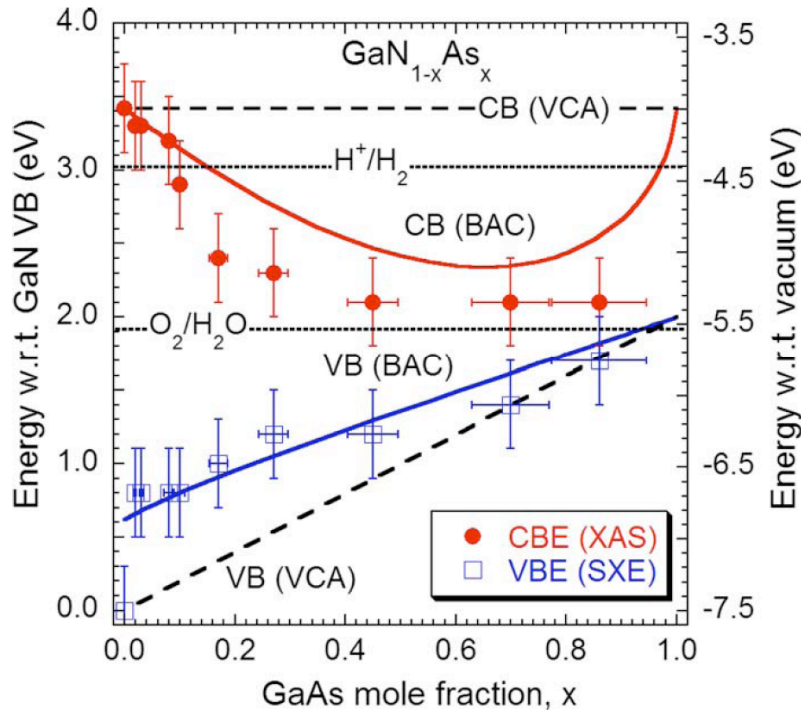


**Fig 1.5** The conduction and valence band edges of crystalline and amorphous  $\text{GaN}_{1-x}\text{As}_x$  as a function of composition as determined by XAS and SXE, plotted with the predictions for these values from the band anti-crossing and virtual crystal approximation models. The  $\text{H}_2/\text{O}_2$  redox potentials are included due to their importance for applications in water splitting (Yu, 2010).

The amorphous structure of these LT-MBE grown alloys presents unique challenges to application due to the metastability of the amorphous phase and due to an abundance of defects. Theoretical work has predicted that amorphous GaN could be a technologically useful electronic material due to the lack of deep gap states, which generally impede the ability to tune electrical properties (Stumm, 1997). Therefore, given the availability of band gap engineering over a wide spectral range, the amorphous nitride-based HMAs could have technological potential, especially in solar energy conversion devices. Subsequent chapters discuss the study of a- $\text{GaN}_{1-x}\text{As}_x$  thermal stability and control of electrical properties through doping.

A key advantage of the LT-MBE technique is the ability to apply it to other highly mismatched alloy systems. This extensibility has allowed for the study of  $\text{GaN}_{1-x}\text{Bi}_x$  alloys, which is the most mismatched III-V semiconductor alloy. The examination of the growth and fundamental properties of this alloy will be discussed in subsequent chapters.

## 2 Thermal stability of amorphous GaNAs

### 2.1 Furnace and rapid thermal annealing

The thermal stability of electronic materials is important due to the high temperatures of some semiconductor processing techniques (e.g. high-quality dielectric deposition) and due to the above-room-temperature operation of many electronic devices. These highly non-equilibrium, amorphous, highly mismatched alloys are likely to be particularly prone to phase segregation due to the very low equilibrium solubility of As in GaN and N in GaAs (Zhang, 2001). When similar species fluxes are used to attempt growing amorphous  $\text{GaN}_{1-x}\text{As}_x$  at intermediate compositions, raising the substrate temperature above  $400^\circ\text{C}$  results in phase segregation into GaAs and GaN. The thermal stability of amorphous  $\text{GaN}_{1-x}\text{As}_x$  was examined using both rapid thermal annealing (RTA) processing, used in the semiconductor industry to minimize the thermal budget, and also conventional furnace annealing. The RTA experiments examined the thermal stability of a- $\text{GaN}_{1-x}\text{As}_x$  for short anneals on the order of seconds, whereas furnace annealing was used to examine long term stability on the order of hours.

The RTA process was conducted in a nitrogen ambient with a GaN wafer proximity cap in the temperature range of  $300\text{-}950^\circ\text{C}$  for 10-60 sec. For films with low arsenic contents ( $< 0.35$ ) negligible composition redistribution of the Ga and As elements was observed within the resolution limit of RBS. For films with higher initial arsenic contents, more significant decomposition in the form of reduced arsenic surface concentration and reduced overall thickness was observed. For example, Fig 2.1 shows the RBS spectra of a 510 nm thick  $\text{GaN}_{0.43}\text{As}_{0.57}$  film before and after a  $850^\circ\text{C} - 20$  sec RTA. The annealing process reduced the As content in the top 280 nm of the film to  $x \sim 0.17$ . This decomposed region was also contaminated with up to 10 at% residual oxygen detected using the  $3.04 \text{ MeV } ^{16}\text{O}(\alpha,\alpha)^{16}\text{O}$  nuclear resonance reaction in RBS. Since RBS determines an areal density which requires the material density to calculate the thickness, the thickness reduction resulting from the RTA cannot be accurately determined because of the unknown density of the annealed material. The overall areal density was reduced by  $9 \times 10^{16} \text{ atoms/cm}^2$  to  $3.38 \times 10^{18} \text{ atoms/cm}^2$  after RTA.

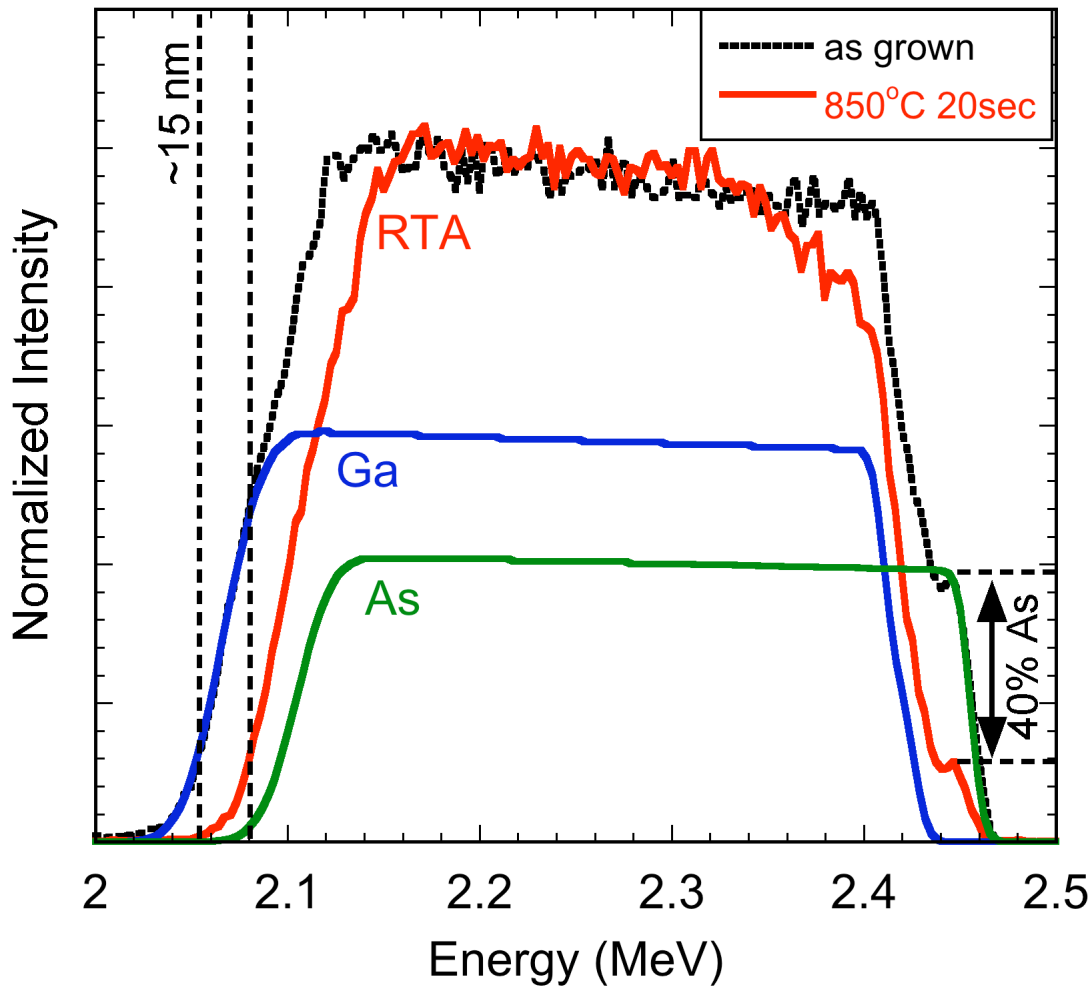


**Fig 2.1** RBS spectra for as-grown  $\text{GaN}_{0.43}\text{As}_{0.57}$  (black) and 850°C-20sec RTA  $\text{GaN}_{0.43}\text{As}_{0.57}$  (red). The RTA resulted in a reduction of As in the surface region and an overall reduction in film thickness.

The XRD patterns in Fig 2.2 show the effect of RTA on the crystallinity of a  $\text{GaN}_{0.64}\text{As}_{0.36}$  film. No crystalline peak can be observed for the film annealed at 700°C for 20 sec. After RTA at 850°C both GaAs:N (111) and GaN:As (0002) diffraction peaks are present. The intensity of the two peaks was dependent on the initial film composition, with a high initial As content resulting in a more intense GaAs:N (111) peak. In low As-content films after 850°C – 20 sec RTA (Fig 2.2), the GaN:As peak shifts to lower angle from that of pure GaN while the GaAs:N peak shows no shift. This suggests that GaN:As is more thermally stable than GaAs:N. After annealing at higher temperatures (950°C), the GaN:As peak agrees with pure GaN indicating further out diffusion of the remaining arsenic. The maximum As fraction in the crystalline GaN:As formed is estimated to be 3.5 at%. We have performed similar RTA processing on films in the range of  $0.30 < x < 0.70$  and found similar behavior. The RTA results suggest that amorphous  $\text{GaN}_{1-x}\text{As}_x$  HMA films are stable up to 700°C for short periods with phase segregation into GaAs:N and GaN:As occurring at around 800°C.

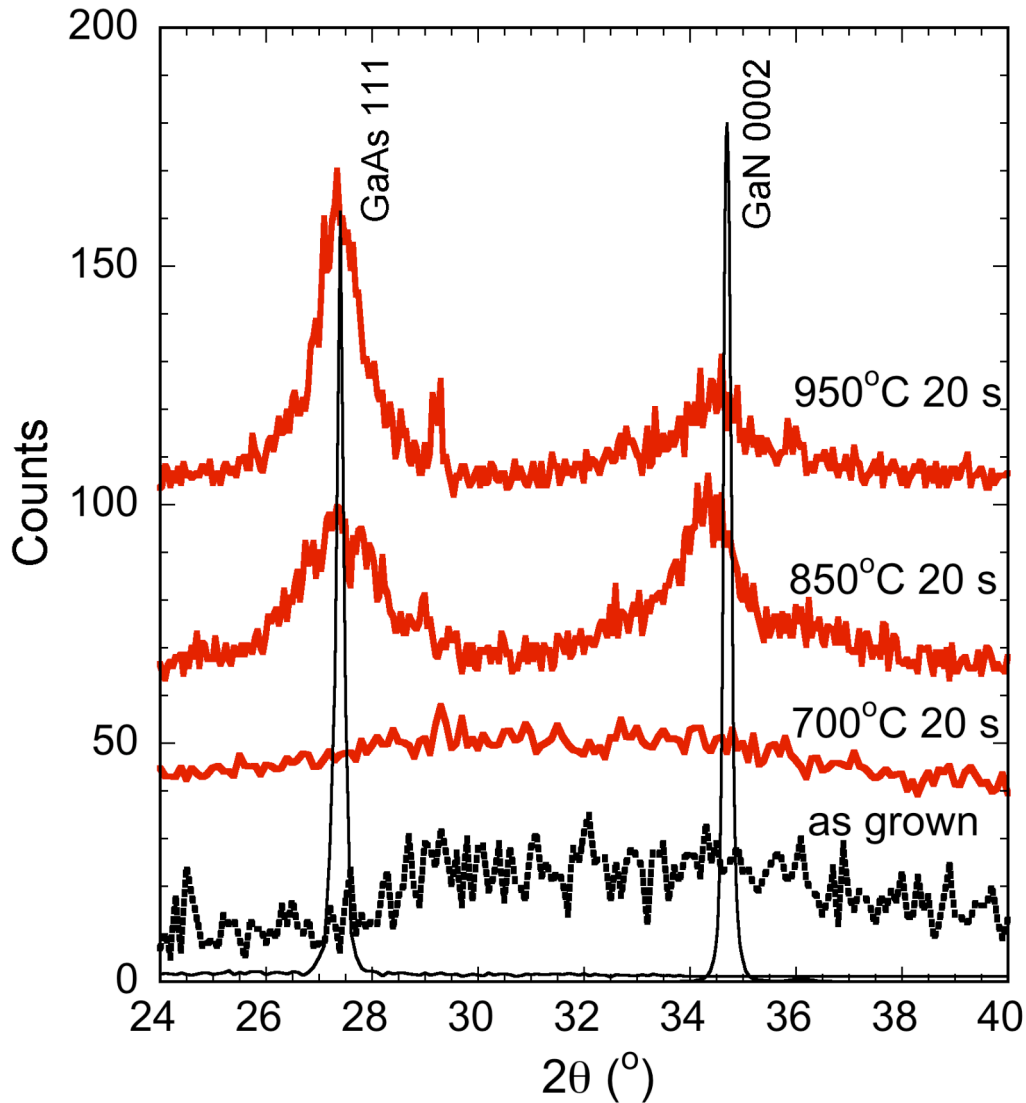


**Fig 2.2** XRD patterns from an a-GaN<sub>0.64</sub>As<sub>0.36</sub> film after successive RTA treatments at increasing temperature for 20 sec each, with GaAs and GaN standards. The GaAs:N (111) and GaN:As (0002) peak positions indicate phase segregation of the amorphous ternary alloy into the corresponding binary crystalline phases.

Furnace anneals were conducted to determine the long-term thermal stability of the alloys. For GaN<sub>1-x</sub>As<sub>x</sub> films with intermediate As compositions, we observed that, for one hour anneals up to 600°C in 1 atm nitrogen ambient, phase segregation did not occur and the films were still amorphous. After annealing for one hour at 700°C, the film was completely decomposed due to the high partial pressures of the anions in the GaN<sub>1-x</sub>As<sub>x</sub> films. These results suggest that the thermal stability of a-GaN<sub>1-x</sub>As<sub>x</sub> alloy films is exceptional considering that crystallization of ion implantation amorphized GaAs and GaN occurs at temperatures as low as 200°C and 500°C, respectively (Kucheyev, 2001). Moreover, for MBE growth of GaNAs alloys with As content higher than ~5 mol%,

phase segregation occurs at growth temperatures above 400°C, but the alloys become amorphous below 400°C (Novikov, 2009). The stability of the amorphous phase also suggests that the cations and anions in the as grown a-GaN<sub>1-x</sub>As<sub>x</sub> alloys are indeed randomly distributed so that long-range diffusion at higher temperatures or long time periods is needed for the kinetically driven crystallization or decomposition to occur. This randomly, homogeneously distributed cation-anion configuration may also present a thermodynamic energy barrier against phase segregation.

The average crystallite size of annealed films was estimated by analyzing the XRD diffraction patterns using the Scherrer equation (Cullity, 2001). The average GaAs:N and GaN:As crystallite sizes for a GaN<sub>0.64</sub>As<sub>0.36</sub> sample are 10.5 nm and 16 nm, respectively after 850°C – 20 sec RTA. RTA at 950°C – 20 sec results in a larger GaAs:N crystal size of ~22 nm while the GaN:As grain size is unchanged. A higher arsenic content ( $x \sim 0.70$ ) in the initial GaN<sub>1-x</sub>As<sub>x</sub> film resulted in larger GaAs (29 nm) and smaller GaN (12.7 nm) grain sizes for 850°C – 20 sec RTA.

The as-grown films have been characterized by TEM and have been shown to have diffuse electron diffraction ring patterns and “pepper/salt” diffraction contrast on high-resolution micrographs, characteristic of an amorphous material (Yu, 2009). TEM results from a GaN<sub>0.64</sub>As<sub>0.36</sub> sample as grown and after 850°C – 20 sec RTA is shown in Fig 2.3a,b. Using Al<sub>2</sub>O<sub>3</sub> as an internal standard, the interplanar distances from the selected area diffraction (SAD) pattern have been calculated. A comparison of the interplanar distances measured by SAD and XRD with the calculated powder diffraction data from GaAs and GaN is shown in Table 2.1. The SAD pattern clearly shows both GaN:As and GaAs:N rings indicating phase segregation in the annealed sample. The first and second rings from the center correspond to the GaAs (111) plane and a superposition of the (1100), (0002), and (1011) planes of GaN. For a sample annealed at 950°C, the spotty pattern from the GaN (0002) ring at a specific arc (marked by arrows in Fig 2.3c) may suggest a preferential crystallization direction, especially close to the substrate.

Bright-field images from cross-section samples show the formation of small crystals distributed uniformly throughout the film (Fig 2.3d). The high-resolution image (Fig 2.3e) taken using a JOEL CM300 Sub-Angstrom TEM with 300keV accelerating voltage shows both GaAs (larger lattice spacings) and GaN (smaller lattice spacings) nanocrystals. Using Z-contrast imaging (Philips Tecnai – 300keV) the crystals with larger lattice spacings were identified as GaAs. Some of the GaAs crystals are twinned, possibly due to nitrogen incorporation. Amorphous-like contrast is visible in high-resolution images suggesting the nanocrystals are embedded in an a-GaN<sub>1-x</sub>As<sub>x</sub> matrix although small grains not satisfying the diffraction condition may cause this contrast.

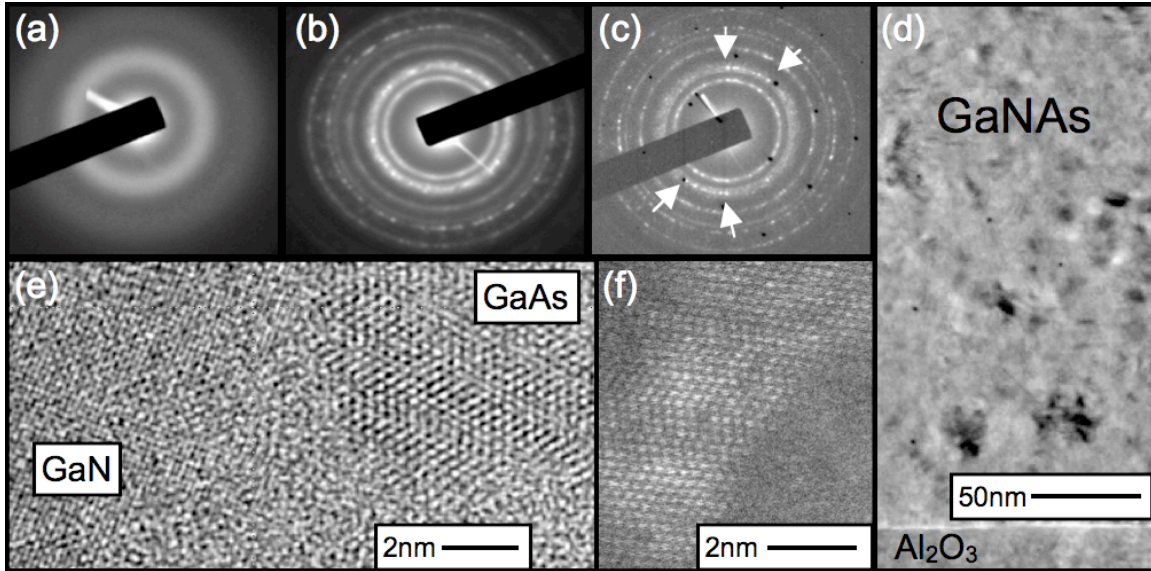


**Fig 2.3** SAD patterns for a-GaN<sub>0.64</sub>As<sub>0.36</sub> as grown (a); after 850°C – 20 sec RTA (b), and after 950°C – 20 sec RTA taken close to the interface (c) (black spots from Al<sub>2</sub>O<sub>3</sub> substrate). Note the strong dotted pattern within the second ring due to (0002) GaN planes. (d) Cross-section of the film showing the formation of randomly distributed grains; (e) High resolution image showing formation of GaAs (larger lattice spacings) and GaN (smaller lattice spacings) crystals; (f) Z-contrast microscopy image of a GaAs grain (brighter contrast from heavier As atoms). Note twinning within the GaAs crystals in (e) and (f).

**Table 2.1** A comparison of the interplanar distances measured by SAD and XRD for GaN<sub>0.64</sub>As<sub>0.36</sub> after 850°C – 20 sec RTA with the calculated power diffraction data from GaAs and GaN. The double arrow indicates one broad ring measured from the inner diameter, the strongly dotted pattern, and the outer diameter.

d-spacing (Å) (experimental)		Calc. powder diffraction standard	
SAD	XRD	GaN (hkl)	GaAs (hkl)
3.28	3.252		3.26 (111)
2.75		2.75 (1 $\bar{1}$ 00)	
2.55	2.60	2.58 (0002)	
2.4		2.43 (10 $\bar{1}$ 1)	
1.98		1.88 (10 $\bar{1}$ 2)	1.998 (220)
1.68 (weak)			1.70 (311)
1.58		1.58 (2 $\bar{1}$ 10)	
1.47		1.46 (10 $\bar{1}$ 3)	1.413 (400)
1.35		1.38 (2 $\bar{2}$ 00)	1.297 (331)

The optical bandgap ( $E_g$ ) of the alloys was characterized by optical absorption spectroscopy using a Perkin-Elmer Lambda 950 Spectrophotometer at room temperature. Fig 2.4 shows absorption spectra of an a-GaN<sub>0.70</sub>As<sub>0.30</sub> film as grown and after 850°C –

20 sec RTA. A shift in the alloy bandgap from 1.57 to 1.87 eV is observed after RTA. This suggests that after RTA, more GaAs:N than GaN:As nanocrystals are formed so that the remaining amorphous matrix has less As. From the higher bandgap of the  $\text{GaN}_{1-x}\text{As}_x$  alloy an As content of  $x \sim 0.25$  after RTA can be estimated (Yu, 2010). This is consistent with the XRD results showing the formation of crystals of GaAs:N and GaN:As in the nanometer scale. Although small GaAs:N crystals are formed after RTA, no significant absorption greater than the magnitude of Fabry-Perot oscillations at 1.4 eV is expected due to the relatively small volume fraction of GaAs:N. This band edge shift to higher energy after RTA was also observed for  $\text{GaN}_{1-x}\text{As}_x$  alloys with different compositions and as grown alloy band gap spanning  $1.55 \text{ eV} < E_g < 2.2 \text{ eV}$ .

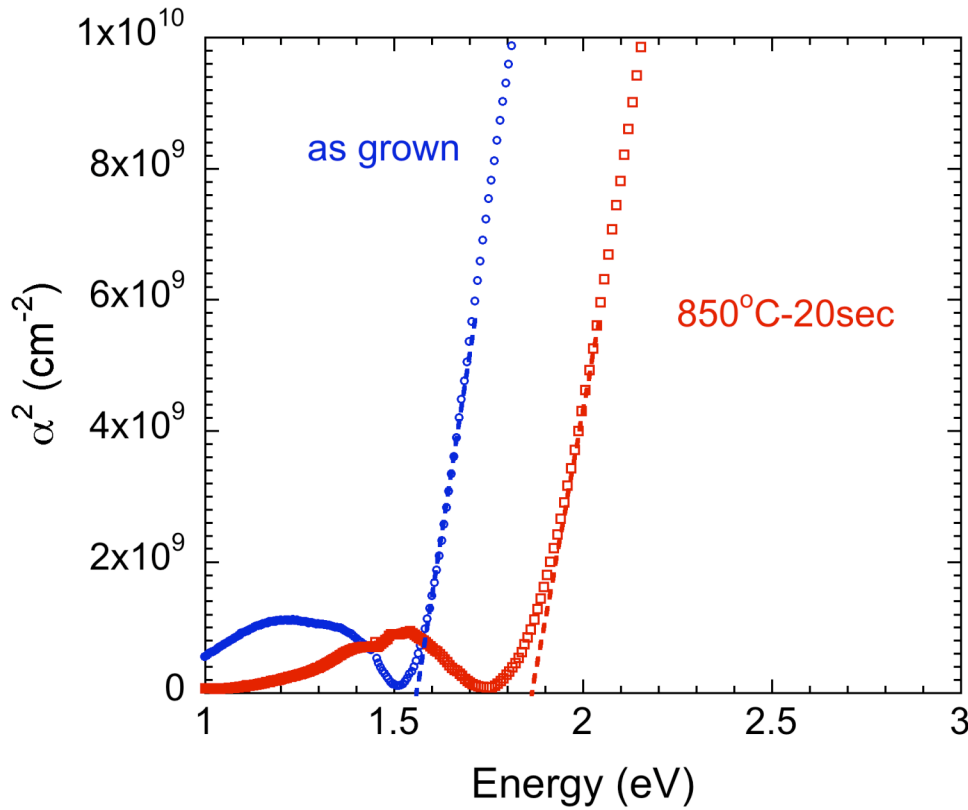


**Fig 2.4** Absorption spectra from as-grown and 850°C – 20 sec RTA  $\text{GaN}_{0.70}\text{As}_{0.30}$ . The shift of the absorption edge indicates the formation of a higher band gap phase.

In summary, the amorphous HMA  $\text{GaN}_{1-x}\text{As}_x$  alloys display unexpectedly high thermal stability with phase segregation occurring for short excursions above 700°C, and was stable in the amorphous phase for long-term anneals at 600°C. Upon phase segregation, GaAs:N and GaN:As nanocrystals nucleated remaining embedded within an amorphous matrix. The resulting size of the nanocrystalline GaAs:N and GaN:As was dependent on the initial film composition and RTA conditions.

## 2.2 Laser annealing

Pulsed lasers allow for the deposition of short, concentrated bursts of energy. Semiconductors can rapidly absorb the optical energy when their band gap is less than the energy of the laser photons, but two photon absorption can also occur. The thermal energy absorbed can be significant enough to form a melt front that extends into the material. As the heat is dissipated through the substrate, the melt front is reversed, and a solidification front moves towards the surface. The solidification front can move as fast as 3 m/sec, trapping solute atoms that would be segregated under slower solidification conditions. Using a pulsed laser with a pulse width of  $\sim 30$  ns, melt times of less than a microsecond can be achieved. The resulting material can be in a highly metastable state due to the rapid kinetics of the pulsed laser melting process (Williams, 1982).

The ability to trap solutes in concentrations far beyond their equilibrium values is a unique advantage of pulsed-laser melting/annealing. This technique has been applied to synthesize various HMAs, including  $\text{ZnTe}_{1-x}\text{O}_x$  and  $\text{GaAs}_{1-x}\text{N}_x$  (Yu, 2002 & 2007). To synthesize these materials, the light, highly mismatched element (e.g. O or N in these cases) is implanted into a substrate of the host material (e.g. ZnTe or GaAs). At this point, although the solute atoms are in the film, they are mainly occupying interstitial sites, or are randomly embedded in an amorphous film. The substrate is then irradiated with a pulsed-laser, allowing for the incorporation of the solute onto crystalline sites. When compared to rapid thermal annealing treatments, using a pulsed laser has orders of magnitude faster kinetics and therefore higher incorporation efficiency. For example, when implanting 2 mol% N into GaAs, an optimized RTA treatment results in  $\sim 0.3$  mol% substitutional N whereas an optimized PLM treatment results in  $\sim 0.8$  mol% substitutional N (Yu, 2003). Pulsed-laser annealing and melting of a- $\text{GaN}_{1-x}\text{As}_x$  were investigated to study the affect of such an ultra-fast annealing process and attempt to recrystallize intermediate compositions of  $\text{GaN}_{1-x}\text{As}_x$  which cannot be synthesized by conventional means (e.g. molecular beam epitaxy).

For these experiments, a KrF excimer laser ( $\lambda \sim 248$  nm) with a  $\sim 30$  ns pulse width was used. Since both GaN and GaAs are direct gap semiconductors and the band gaps of  $\text{GaN}_{1-x}\text{As}_x$  across the composition range are significantly less than the 5 eV energy of the laser, the incident laser photons should be absorbed rapidly. Of primary concern was whether or not the laser would ablate the a- $\text{GaN}_{1-x}\text{As}_x$  film. To mitigate the potential outgassing of nitrogen or oxidation by the ambient the laser annealing experiments were conducted in a 2 atm  $\text{N}_2$  environment. RBS spectra of the films were collected before and after laser annealing. A set of representative spectra for a- $\text{GaN}_{0.35}\text{As}_{0.65}$  is shown in Fig 2.5. Due to the larger mass of As compared to Ga, the onset of the As edge occurs at higher energy. As has been mentioned in the previous section, RTA treatments (green line) at conditions required for recrystallization (e.g.  $850^\circ\text{C} - 30$  sec) tend to significantly decrease the concentration of As in the surface region. However, for pulsed-laser annealing at laser fluences of  $0.20 \text{ J/cm}^2$  (blue line) and  $0.40 \text{ J/cm}^2$  (red line) the composition profile did not change significantly. This confirms that due to the rapid kinetics of the laser annealing process, there is less redistribution of atoms compared to RTA treatments.

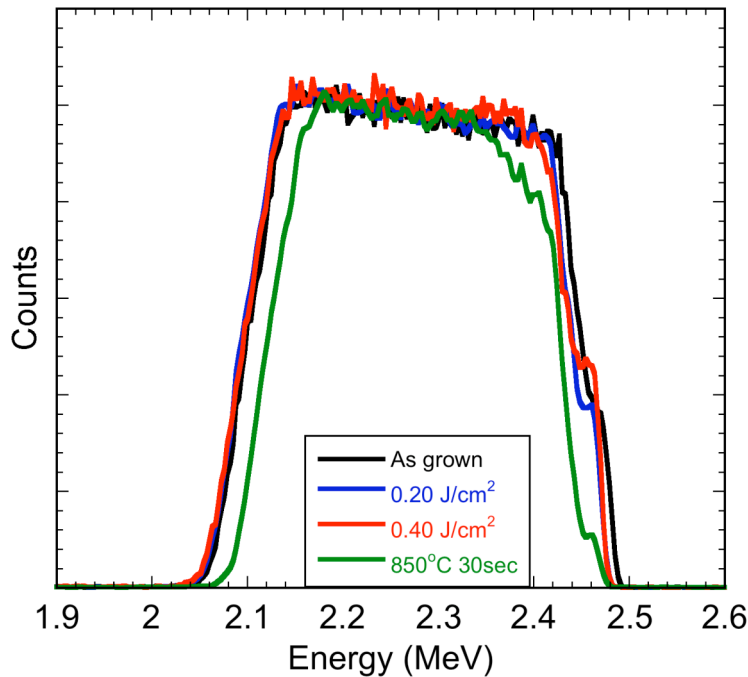


**Fig 2.5** RBS spectra for a-GaN<sub>0.35</sub>As<sub>0.65</sub> as grown (black) and subjected to different laser or thermal annealing. Note the lower intensity of the surface As signal for the 850°C – 30 sec RTA (green) sample. The laser annealed samples have a similar composition profile to the as-grown sample.

The resulting structure of the laser-annealed films could not be accurately investigated using a lamp source x-ray diffractometer. The brightness of the Cu  $K_{\alpha}$  source tube was not sufficient to generate enough diffracted intensity. Instead, these films were characterized using synchrotron radiation at the Stanford Synchrotron Radiation Laboratory at beamline 11-3. The beam energy was 12.735 keV with a resolution ( $dE/E$ ) of  $5 \times 10^{-4}$  and an area detector was used for rapid data collection. Representative results from the area detector for a-GaN<sub>0.35</sub>As<sub>0.65</sub> as grown and subjected to various annealing conditions are shown in Fig 2.6. The areas of high diffracted intensity are red whereas the blue regions indicate areas of low diffracted intensity. The amorphous, as-grown sample (Fig 2.6a) has a characteristically broad diffraction pattern. The diffraction patterns from the RTA 850°C – 30 sec (Fig 2.6b) sample and the pulsed laser annealed at a fluence of 0.40 J/cm<sup>2</sup> (Fig 2.6c). The high-intensity spots in (Fig 2.6b) are due to unintended alignment to the single-crystal sapphire substrate. The unbroken rings of diffracted intensity suggest that the crystalline phases formed are not textured.

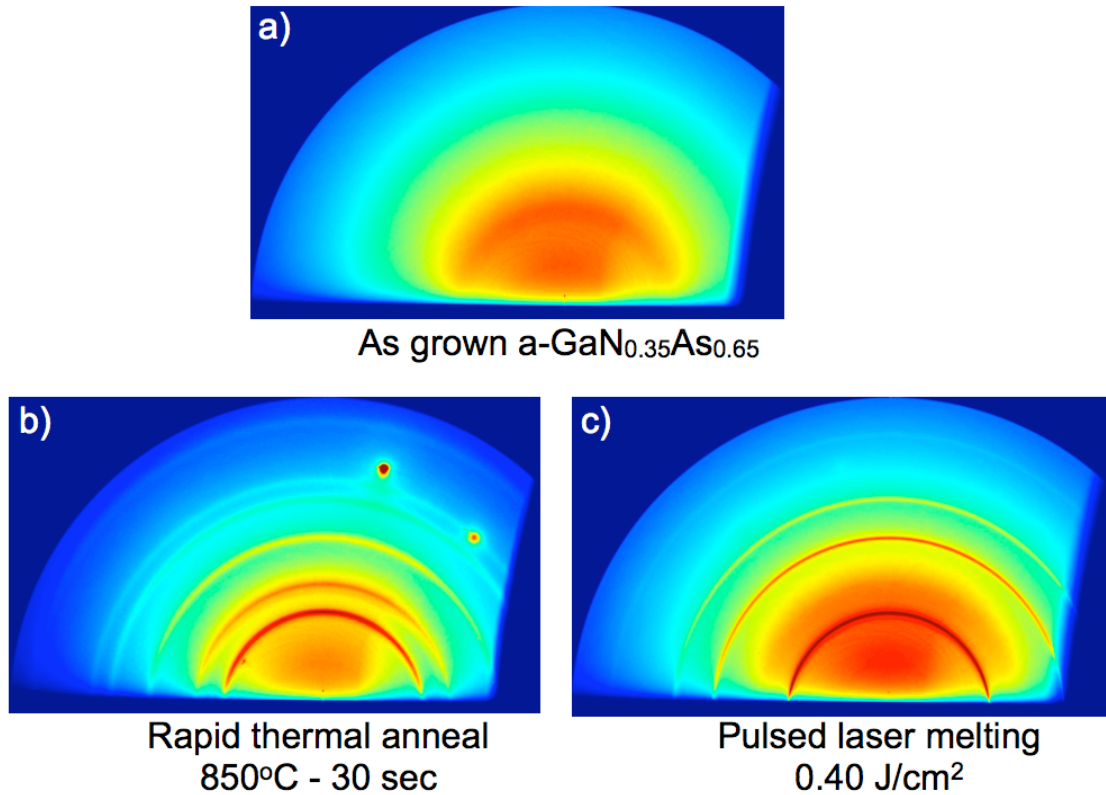


**Fig 2.6** Synchrotron diffraction patterns from a) as-grown a-GaN<sub>0.35</sub>As<sub>0.65</sub>, b) a-GaN<sub>0.35</sub>As<sub>0.65</sub> subject to a 850°C – 30 sec RTA, and c) a-GaN<sub>0.35</sub>As<sub>0.65</sub> laser annealed with a fluence of 0.40 J/cm<sup>2</sup>. Red indicates a high diffracted intensity.

Integrating the diffraction patterns allows for the plotting of conventional line scans (intensity vs.  $2\theta$ ) shown in Fig 2.7 and Fig 2.8 for two different compositions of GaN<sub>1-x</sub>As<sub>x</sub>. Three of the line scans from GaN<sub>0.35</sub>As<sub>0.65</sub> shown in Fig 2.7 correspond to the diffraction patterns in Fig 2.6. Using the line scans, the diffraction patterns can be easily interpreted. Vertical dashed lines are a reference for the expected positions of zinc blende GaAs (dark gray lines) and wurtzite GaN (light gray lines) diffraction intensity. The purple dashed line indicates the expected position of zinc blende GaN<sub>0.35</sub>As<sub>0.65</sub> diffraction intensity. A peak would be expected at that position ( $\sim 18.7^\circ$ ) if the material recrystallized into a zinc blende structure with the same composition as the original amorphous film.

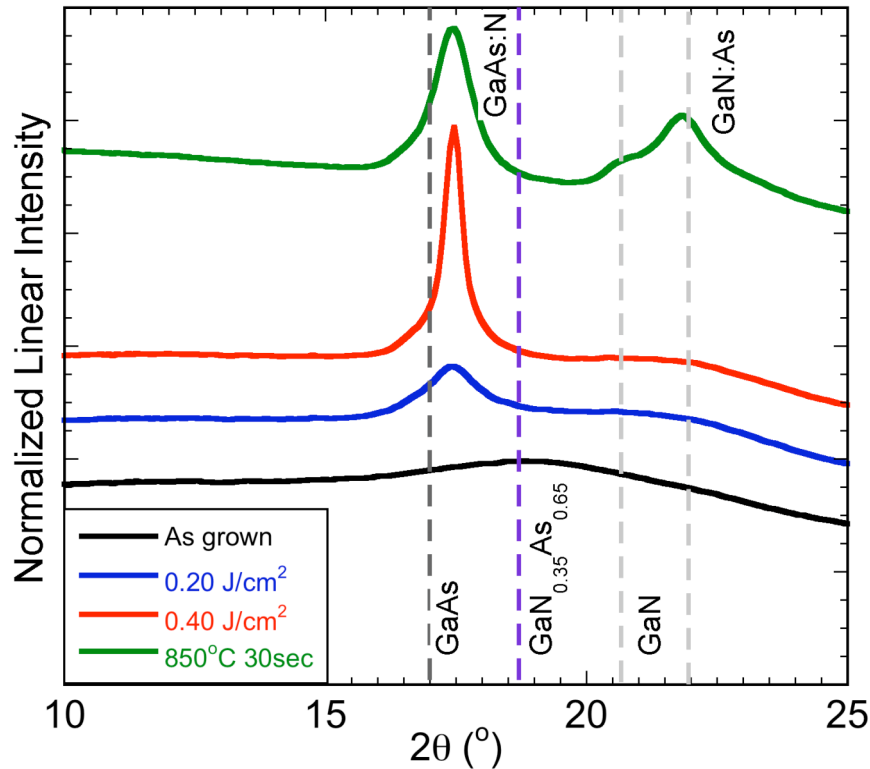


**Fig 2.7** Integrated diffraction patterns for a-GaN<sub>0.35</sub>As<sub>0.65</sub> as-grown and subjected to various annealing conditions. Vertical dashed lines are given to reference the angles at which diffraction conditions are satisfied for zinc blende GaAs, wurtzite GaN, and the expected location for zinc blende GaN<sub>0.35</sub>As<sub>0.65</sub> assuming a linear interpolation of lattice constants.

It is evident in the data shown in Fig 2.7 that the highly mismatched composition was not maintained after the various annealing treatments. However, c-GaAs:N is formed with ~8 at% N. This represents the largest amount of N incorporated into GaAs from a PLM or RTA process. As the laser fluence increases, the intensity of the GaAs:N peak increases. This is attributed to a longer melt time and larger melt volume creating larger grains and a higher density of GaAs:N grains. The full-width half max of the GaAs:N peak for highest laser fluence annealed sample is significantly narrower than the corresponding peak in the RTA case. This is due to a narrower composition and/or grain size distribution in the laser-annealed case.

In addition, an interesting consequence of the laser annealing is that GaN formation is suppressed for both laser fluences tested in contrast with the RTA treatment. This may be caused by differences in diffusion rates. For GaAs to be formed, N must diffuse out of As-rich areas. However, for GaN to be formed, As must diffuse out of N-rich areas. The larger As atom may not have sufficient time to diffuse out of the way of GaN crystallite formation during the ultra-fast laser annealing process.

For samples with a lower initial As content, similar trends are observed. The synchrotron diffraction results for GaN<sub>0.68</sub>As<sub>0.32</sub> grown on a glass substrate and subjected to various annealing treatments are summarized in Fig 2.8. The high intensity “hump” at

low angle is a characteristic of the amorphous glass substrate used in this sample growth. Observing the diffraction peaks above the noise from the amorphous substrate is challenging. As in the previous case, GaN:As formation is suppressed in the laser annealed samples.

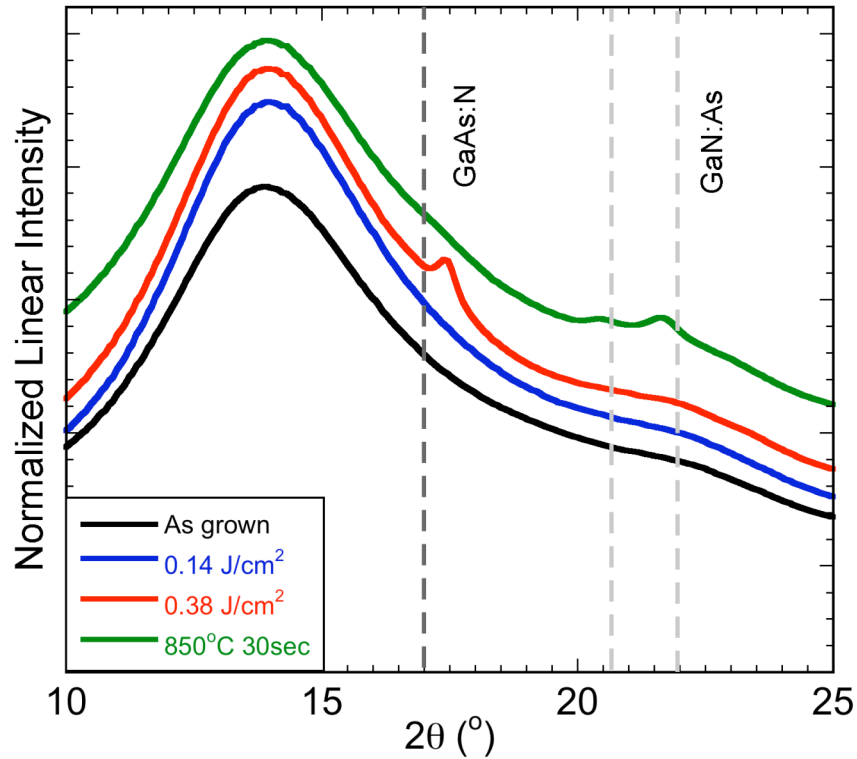


**Fig 2.8** Integrated diffraction patterns for a-GaN<sub>0.68</sub>As<sub>0.32</sub> as grown and subjected to various annealing conditions. The large broad feature at 12-16° is due to the amorphous glass substrate. Dashed lines reference the angles at which the diffraction conditions are satisfied for zinc blende GaAs and wurtzite GaN.

Samples that were crystalline as-grown were also tested to determine the effect of annealing conditions. The diffraction patterns shown in Fig 2.9 are representative of wurtzite GaN<sub>0.95</sub>As<sub>0.05</sub> as-grown and subjected to RTA and laser-annealed treatments. The RTA has very little effect on the GaN:As peak height. However, the laser-annealed sample peak height intensity is reduced by about half. This reduction in peak height is most likely attributed to laser damage of the crystalline material.

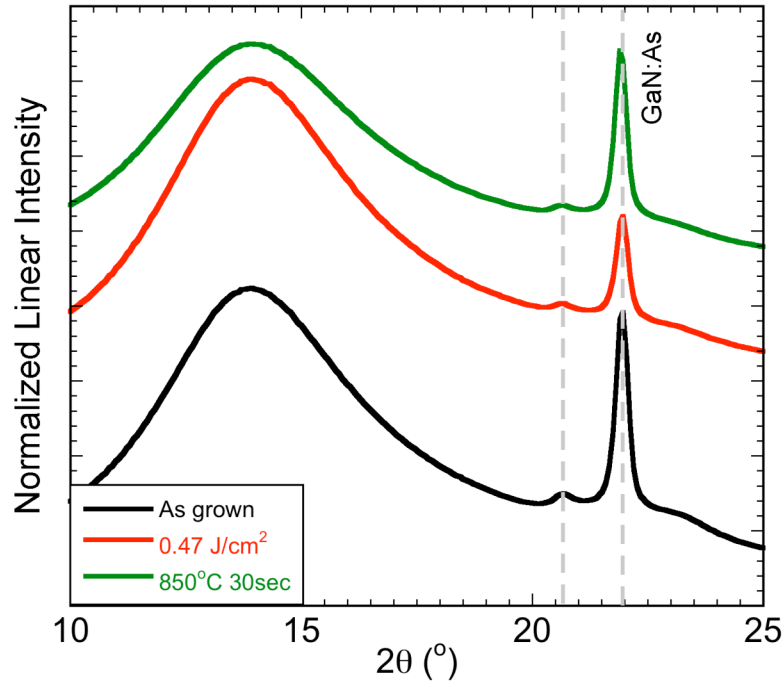


**Fig 2.9** Integrated diffraction patterns for wurtzite  $\text{GaN}_{0.95}\text{As}_{0.05}$  as grown and subjected to various annealing conditions. If the material is already crystalline, the laser annealing or RTA does not have a significant affect.

The microstructure of a  $\text{GaN}_{0.68}\text{As}_{0.32}$  thin film grown on glass and annealed with a laser fluence of  $0.38 \text{ J/cm}^2$  was closely examined using transmission electron microscopy. Three regions can be identified in the low-resolution image shown in Fig 2.10 and a corresponding diffraction pattern is given for each region. The top  $\sim 100 \text{ nm}$  of the epilayer was melted by the laser shot and recrystallized into predominantly  $\text{GaAs:N}$ , along with some trace  $\text{GaN:As}$  according to the SAD pattern. Below this layer, about  $100 \text{ nm}$  of material was not melted by the laser. The diffraction pattern reveals that the layer is still predominantly amorphous. Lastly, the glass substrate has a diffuse amorphous diffraction pattern unaffected by the laser shot as expected.

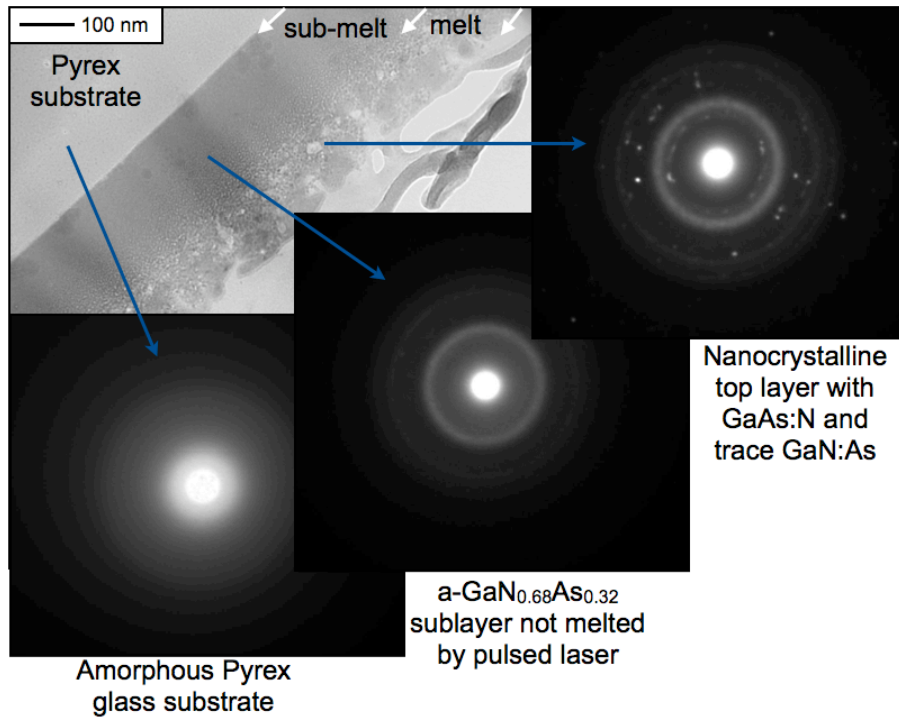


**Fig 2.10** Low-resolution TEM images and corresponding SAD patterns (indicated by arrows) of  $a\text{-GaN}_{0.68}\text{As}_{0.32}$  laser annealed at a fluence of  $0.38 \text{ J/cm}^2$ . Only the top  $\sim 100$  nm of the thin film was melted and recrystallized by the laser annealing process.

High-resolution TEM was conducted to examine both the melted and recrystallized layer and the layer that was not melted by the laser shot. The HR-TEM image in Fig 2.11 is taken from the top of the layer and features nanograins of GaAs:N with diameters on the order of 4-7 nm. There is little amorphous material remaining. Larger grains are found even closer to the surface, corresponding with longer melt times. Below this layer is a section that was not melted by the pulsed laser. However, the HR-TEM image in Fig 2.12 reveals that instead of being homogeneously amorphous like the as-grown material, there are small nanograins on the order of  $\sim 2$  nm in diameter. Essentially, this microstructure is similar to the RTA-ed microstructure shown in Fig 2.3. Thus, the layer of  $a\text{-GaN}_{0.68}\text{As}_{0.32}$  that was not melted was effectively subjected to an ultra-fast thermal anneal resulting in very small crystallites embedded in an amorphous matrix.

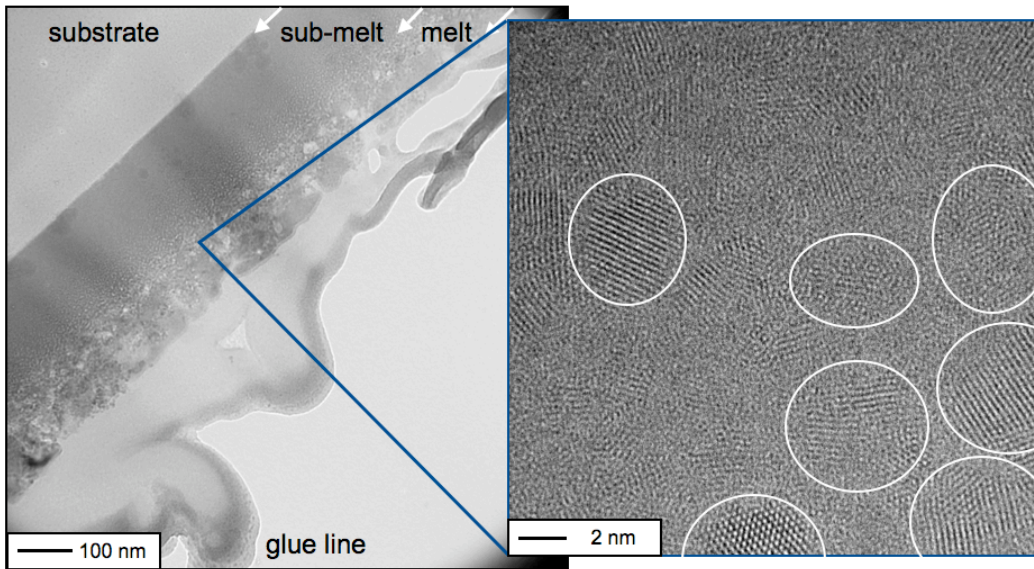


**Fig 2.11** Low-resolution TEM image shown in Fig 2.10 with a corresponding high-resolution TEM image of the melted and subsequently recrystallized region of a- $\text{GaN}_{0.68}\text{As}_{0.32}$ . Nanosized grains of zinc blende GaAs:N are visible with larger grains closer to the surface.

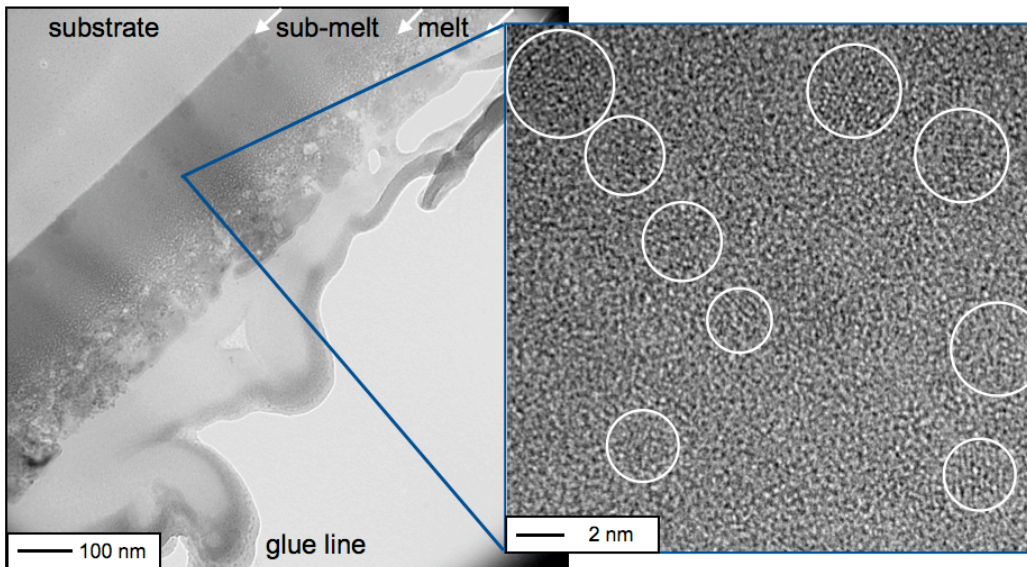


**Fig 2.12** Low-resolution TEM image shown in Fig 2.10 with a corresponding high-resolution TEM image of the region that was not melted by the laser annealing. Very small nanograins with diameters on the order of  $\sim 2\text{nm}$  are visible.

Laser annealing and melting provides a unique route to the synthesis of highly non-equilibrium material compositions and structures. The rapid kinetics can overwhelm the thermodynamics of a system, allowing for the trapping of highly mismatched solutes. In the case of laser annealing  $\alpha$ -GaN<sub>1-x</sub>As<sub>x</sub> at intermediate compositions, the kinetics of the ultra-fast laser annealing process were not sufficient to cause the homogeneous nucleation of a crystalline phase at the intermediate composition. However, significant concentrations of nitrogen, on the order of 8 at%, were trapped in the resulting zinc blende GaAs grains. This amount of N incorporation is larger than the maximum N incorporation achieved in single crystal material (~ 4 at%) using advanced MBE growth techniques (Pulzara-Mora, 2006; Zhukov, 2001).

### 3 Electronic properties of amorphous GaNAs

The key advance in amorphous silicon (a-Si) leading to its applications in thin film electronics and photovoltaics was the ability to dope the material both *p*-type and *n*-type (Spear, 1976 & 1977; Carlson, 1976). As a point of reference, typical conductivities for hydrogenated a-Si are in the range of  $10^{-2} - 10^{-1}$  S/cm (Kakalios, 1986). a-Si photovoltaic technology has since advanced by taking advantage of a range of band gaps accessible through alloying with germanium or carbon (Yang, 1997; Tawada, 1981). Alloying of a-Si has led to multi-junction solar cells with somewhat higher efficiencies, but it also causes reduced electrical performance due to higher defect densities (Paul, 1993; Morimoto, 1982). The poor conductivity and the limited bandgap range of a-Si alloys severely hinder the widespread applications of a-Si alloys despite their potential advantages of lower cost and ability to deposit on flexible substrates. To overcome these deficiencies, amorphous compound semiconductors such as a-GaAs grown either by sputtering or plasma-enhanced chemical vapor deposition were extensively researched (Hargreaves, 1980; Segui, 1982). However, the inability to dope these compound semiconductors, explained theoretically by a self-compensation mechanism, reduced the interest in amorphous compound semiconductors (Street, 1989; Robertson, 1986). The ability to control the electrical properties of amorphous  $\text{GaN}_{1-x}\text{As}_x$  alloys that exhibit a wide bandgap range of 0.8-3.4 eV could lead to exciting applications in electronics and photovoltaics.

To test the ability to dope these alloys,  $\text{GaN}_{1-x}\text{As}_x$  thin films were grown by plasma-assisted molecular beam epitaxy on *c*-plane sapphire at temperatures between 200-320°C. Typical beam equivalent pressures (BEPs) for homogeneously amorphous material are  $1.5 \times 10^{-5}$  Torr for N,  $7.7 \times 10^{-6}$  Torr for As, and  $1.1 \times 10^{-7}$  Torr for Ga. For *p*-type doping, the Mg content in the film was controlled by the Mg BEP. The composition and thickness of the alloy and the total amount of Mg incorporated in the films was determined by RBS with a 3.04 MeV  $\text{He}^{2+}$  beam. Due to the uncertainty in the bonding configuration of the dopants in the disordered structure, the atomic percentage of the dopant is reported. The composition and thickness of  $\text{GaN}_{1-x}\text{As}_x$  films discussed for doping are  $x \sim 0.55-0.65$  and  $\sim 1 \mu\text{m}$ , respectively. The  $\text{GaN}_{1-x}\text{As}_x:\text{Mg/Te}$  films are stoichiometric with a (III+II)/(V+VI) atomic ratio of unity +/- 3%.

Electrical conductivity measurements were conducted in the van der Pauw geometry using a liquid-helium cryostat and pressed indium contacts made after a brief HCl rinse. The ohmic behavior of the contacts was verified by the linear trend of the current-voltage curve. The result of the Mg incorporation on the direct-current conductivity of a series of  $\text{GaN}_{0.35}\text{As}_{0.65}$  films is shown in Fig 3.1. The conductivity increased monotonically with increasing magnesium content, up to a maximum value of 4.86 S/cm at room temperature for 8 at% Mg. The low temperature region (50-6K) of the Arrhenius plot of  $\ln(\sigma)$  versus  $1/T$  remains linear, and from this an activation energy ( $E_a$ ) for the conduction was determined (Fig 3.1 inset). With increased magnesium doping, the  $E_a$  decreased from 215 meV to 0.32 meV.

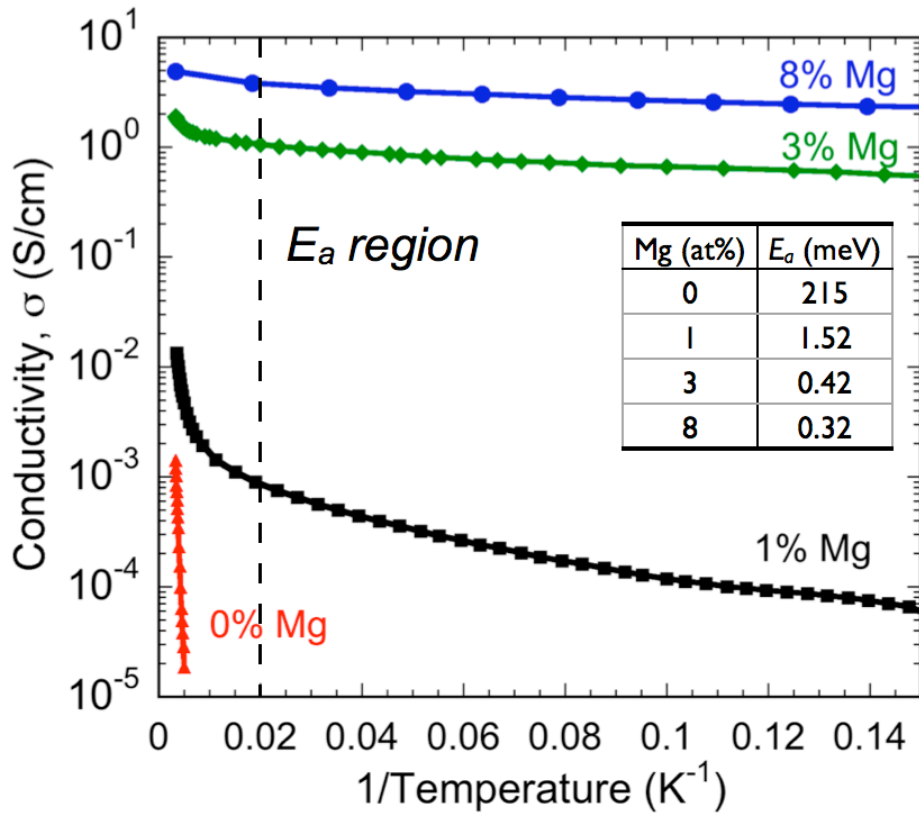


**Fig 3.1** Conductivity as a function of temperature for  $\text{GaN}_{0.35}\text{As}_{0.65}:\text{Mg}$  samples with varying Mg content given in atomic percents. The inset table gives activation energies calculated from the linear low temperature region of the curve to the right side of the dashed line (50-6K).

Ionization energies for acceptors in GaAs and GaN are in the range of 10-100s meV; so the low energy thermally activated transport provides a clear evidence for the hopping conduction, indicating the presence of large local fluctuation of the valence band edge (Mireles, 1998). The reduction of  $E_a$  with increasing Mg content can be attributed to an increase in the hole concentration and associated moving of the Fermi energy,  $E_f$ , toward the valence band. At low concentrations the holes are localized in isolated low energy valleys and the transport is determined by the thermal activation over energy barriers. The effective barrier height decreases as  $E_f$  moves deeper into the valence band and for high enough hole concentrations the holes regain their extended character and the material shows nearly metallic, weakly temperature dependent conductivity. According to Hall measurements performed in a 7 Tesla field, the room-temperature Hall mobility of the sample with 1% Mg was approximately  $1 \text{ cm}^2/\text{V sec}$  with a carrier concentration of  $\sim 1 \times 10^{17} \text{ cm}^{-3}$ . The sample with the highest conductivity had a Hall mobility of approximately  $0.3 \text{ cm}^2/\text{V sec}$  with a carrier concentration of  $\sim 1 \times 10^{20} \text{ cm}^{-3}$ . The low mobility is attributed to the disordered structure and indicates a strong alloy disorder scattering in this HMA. Although the hole concentration is high, it is still much lower

than the concentration of Mg atoms. However, such low doping efficiency is typical of amorphous semiconductor materials (Stutzmann, 1987).

In order to confirm that magnesium was indeed behaving as an acceptor, donating holes to the valence band, the thermopower was measured for both doped and undoped films. Thermopower measurements were conducted using a home-built, liquid-nitrogen cryostat setup (Ager III, 2008) with a thermal gradient of  $2^{\circ}\text{C}$  at each average temperature point. The thermopower as a function of average temperature are shown in Fig 3.2. The undoped films had a negative thermopower, indicating electrons as the majority carrier in the material. Upon incorporation of 1 at% Mg, the thermopower sign inverted to a positive value of  $\sim 187 \mu\text{V/K}$  indicating holes as the majority carrier, confirming that Mg was behaving as an acceptor. The decrease in the magnitude of the thermopower to  $\sim 88 \mu\text{V/K}$  with increased magnesium content indicates a movement of the Fermi level ( $E_f$ ) towards the valence band, which would result in a higher hole concentration in the valence band. This result agrees with the  $\sigma(T)$  shown in Fig 3.1.

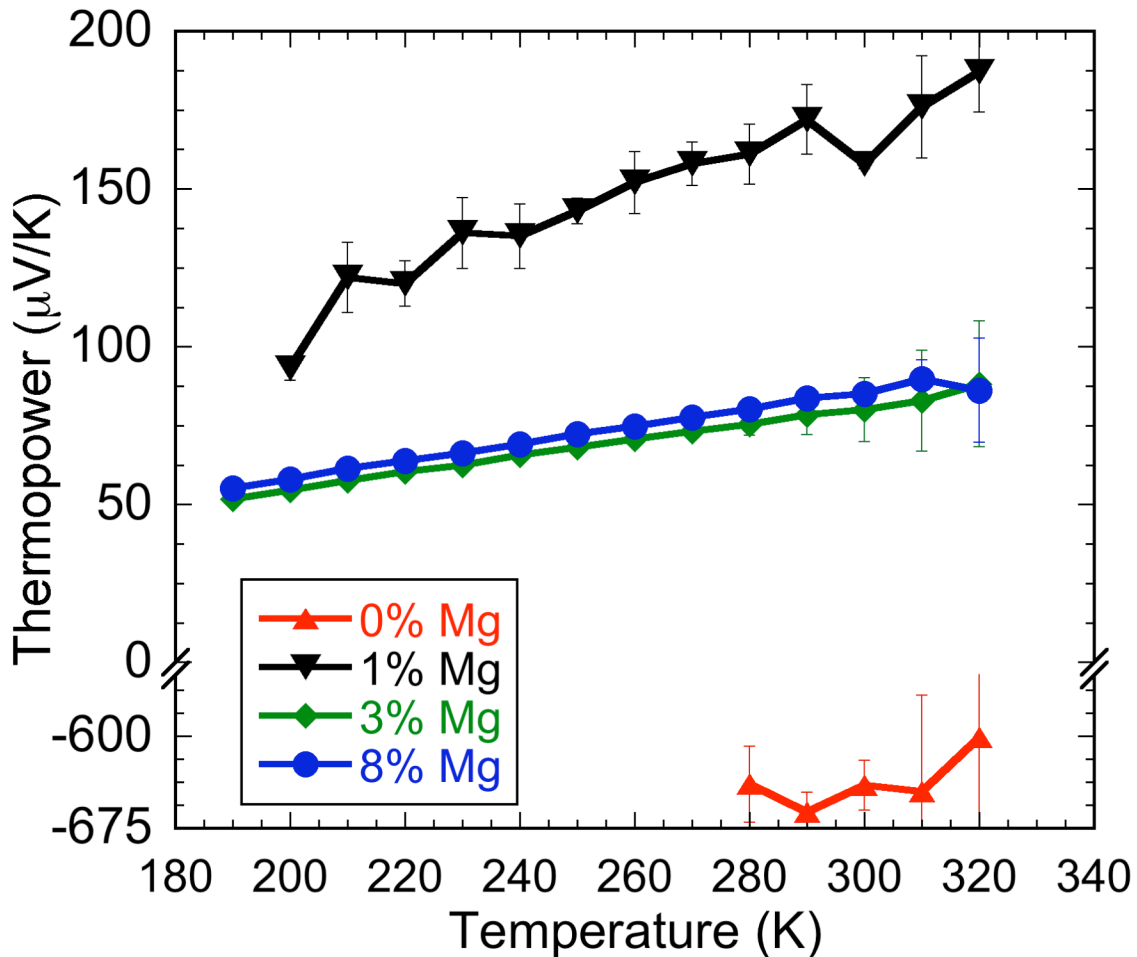


**Fig 3.2** Thermopower as a function for temperature for  $\text{GaN}_{0.35}\text{As}_{0.65}\text{:Mg}$  samples with varying Mg content (same samples as shown in Fig 3.1). The positive sign for Mg doped samples shows Mg behaving as an acceptor. The error bars signify the standard deviation

from three measurements at a given average temperature. Higher resistance samples have larger errors due to the uncertainties in measuring small voltages across large resistances.

In addition to demonstrating the *p*-type doping, we also doped the material *n*-type. The group VI element tellurium was used to dope the material *n*-type. Tellurium doping was achieved by heating a PbTe source during growth. The PbTe decomposes on the substrate at the growth temperature resulting in the uniform incorporation of Te and rejection of Pb. RBS measurements confirmed that no Pb was present and only Te atoms were incorporated in the film. For a Te concentration of 0.25 at% the conductivity increased to 0.25 S/cm and the thermopower remained negative while decreasing in magnitude to -180  $\mu\text{V/K}$ . Again, the decrease in magnitude indicates a shift of  $E_f$ , but this time the shift is towards the conduction band for a higher free electron concentration.

In order to achieve control over the electronic properties of  $\text{GaN}_{1-x}\text{As}_x$  in the intermediate composition range, the gallium BEP was increased above typical values for the deposition of uniform homogeneously amorphous material. This results in a driving force for the formation of c-GaAs:N clusters; this can be observed in the XRD and TEM shown in Fig 3.3. The dashed line XRD pattern in Fig 3.3(a) is from a representative  $\text{GaN}_{0.35}\text{As}_{0.65}\text{:Mg}$  sample grown on a sapphire substrate with electrical properties described in Fig 3.1 & Fig 3.2. From the c-GaAs:N (111) XRD peak shift, the N incorporation fraction in the c-GaAs:N is estimated to be 7-8 mol%. The low magnification Z-contrast TEM image (TEAM 0.5 – 300 keV) shown in Fig 3.3(b) reveals the distribution of the two phases: As-rich polycrystalline GaAs:N (bright), and intermediate As content amorphous  $\text{GaN}_{1-x}\text{As}_x$  with a low density of nanocrystallites (dark). The two phases contribute to the average nominal composition of  $\text{GaN}_{0.35}\text{As}_{0.65}$  determined by RBS. The density of the respective phases is not dependent on the Mg concentration but instead is a result of the higher Ga BEP. The rings with spots (1, 2 and 3) indexed in the selected area diffraction pattern (JEOL 3010 – 300 keV) in Fig 3.3(c) correspond to c-GaAs:N. They are superimposed on two broad rings (marked by black arrows) that are typical for amorphous material. The high-resolution TEM images (JEOL CM300 – 300 keV) in Fig 3.3(d) & (e) show the amorphous regions [dark contrast in Fig 3.3(b)] and polycrystalline grains [bright contrast in Fig 3.3(b)], respectively. By adjusting the growth conditions, the relative intensity of the c-GaAs:N XRD peak intensity can be reduced, as seen in the solid line of Fig 3.3(a). For this sample, the As flux was reduced from  $5.5 \times 10^{-6}$  to  $2.0 \times 10^{-6}$  Torr in order to minimize the formation of c-GaAs:N while maintaining a relatively high conductivity of 0.17 S/cm. Due to the higher Ga BEP, these  $\text{GaN}_{1-x}\text{As}_x$  alloys are mixed phase with polycrystalline GaAs:N phase present in an amorphous  $\text{GaN}_{1-x}\text{As}_x$  matrix.

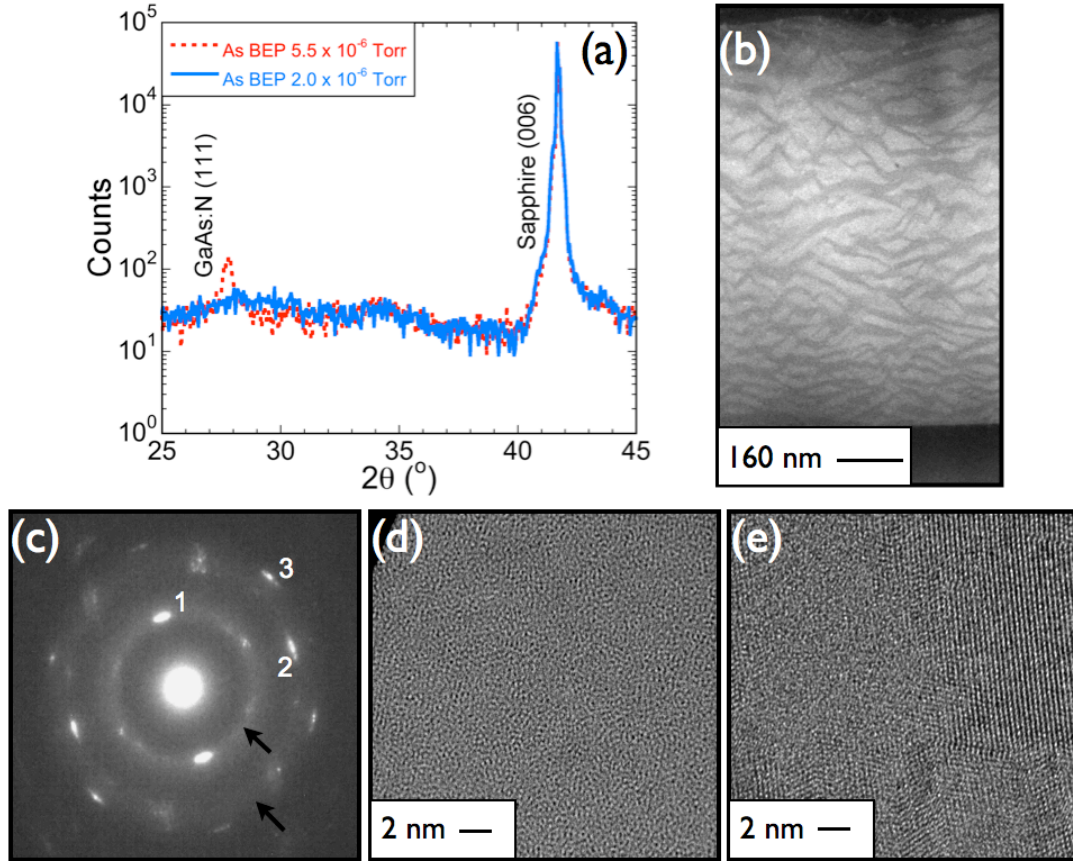


**Fig 3.3** Structural analysis of  $\text{GaN}_{0.35}\text{As}_{0.65}\text{:Mg}$  samples. Representative x-ray diffraction pattern of samples discussed in Fig 3.1 & Fig 3.2 (dashed) and sample grown under lower As BEP to reduce crystallinity (solid) (a). Low magnification Z-contrast transmission electron micrograph, selected area diffraction, and high-resolution TEM images of a sample discussed in Fig 3.1 & Fig 3.2 (b), (c), (d), and (e) respectively. In (b), the bright contrast is the c-GaAs:N phase shown in (e) and the dark contrast is the amorphous  $\text{GaN}_{1-x}\text{As}_x$  phase shown in (d). The diffraction pattern (c) shows a superposition of c-GaAs:N rings from (111), (220), and (311) planes indicated by 1, 2, and 3 and two broad amorphous rings indicated by arrows.

Despite the crystallinity in the samples for which electrical data is presented, the c-GaAs:N phase are embedded in an amorphous  $\text{GaN}_{1-x}\text{As}_x$  matrix, and it is not possible to determine which phase dominates the electrical properties. However, if the amorphous phase were highly insulating, the hopping between conductive c-GaAs:N would not result in the high conductivities and low conduction  $E_a$  observed.

To summarize, control over the electrical properties of mixed phase  $\text{GaN}_{1-x}\text{As}_x$  has been demonstrated. Both *p*-type and *n*-type doping was achieved as confirmed by conductivity and thermopower measurements. However, the ultimate goal is to have a conducting homogeneous amorphous alloy of  $\text{GaN}_{1-x}\text{As}_x$ . The wide range of band gaps accessible using this material makes it promising for solar conversion devices. In order to achieve this goal, numerous experiments were conducted using these original growth parameters as a baseline in an attempt to validate that the amorphous phase was

conducting. Various growth parameters were tested, including the growth temperature, As flux, and Ga flux. Decreasing the temperature, As flux, and Ga flux should all drive the system towards the amorphous phase. However, the resistivity must be kept low for applications in electronics.

Both the growth temperature and As BEP have an affect on the resulting film. As the temperature decreases, the arsenic content increases due to more of the adsorbed atoms sticking instead of desorbing (Fig 3.4). As expected, increasing the arsenic BEP also results in an increased As content (Fig 3.4). Interestingly, despite significant changes in the incorporated As content, both of these variables have no affect on the III:V ratio, which remains near unity. In addition, the magnesium content remained constant at ~9 at% irrespective of growth temperature or As BEP, corresponding to the highest conductivity achieved.

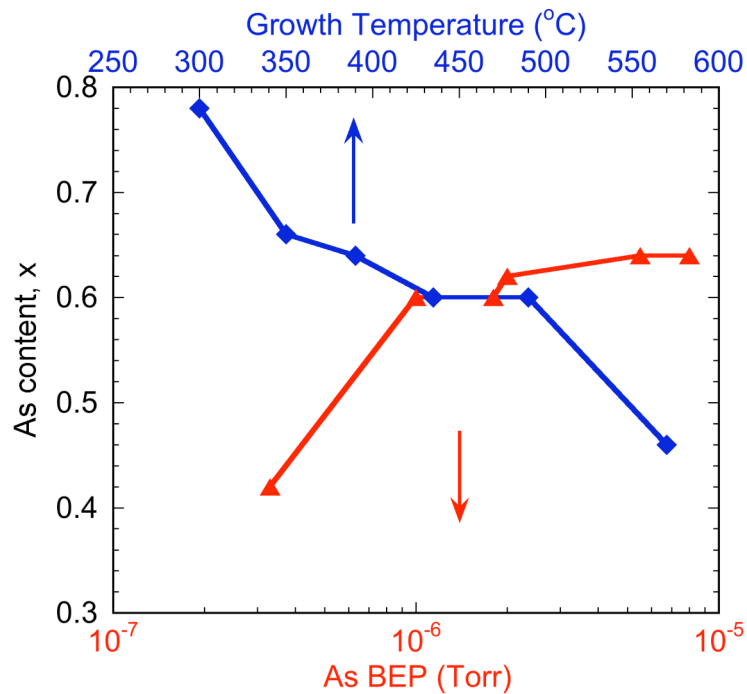


**Fig 3.4** Arsenic content in  $\text{GaN}_{1-x}\text{As}_x\text{:Mg}$  as a function of growth temperature (blue) and As BEP (red).

At high growth temperatures, the  $\text{GaN}_{1-x}\text{As}_x$  system phase segregates. However, at the elevated Ga flux used for achieving conductivity and Mg activation, c-GaAs is present at much lower growth temperatures. Decreasing the temperature reduces both the GaAs (111) and GaN (0002) peak heights (Fig 3.5), indicating a reduction of crystallite size and a trend towards becoming amorphous. As the crystallite size decreases, there is a weak trend towards lower resistivity (Fig 3.6). The film grown at 300°C does not have any significant peaks in XRD, but HR-TEM is required to determine if the film is completely amorphous. This last film was semi-insulating despite an incorporation of Mg equal to the other films.

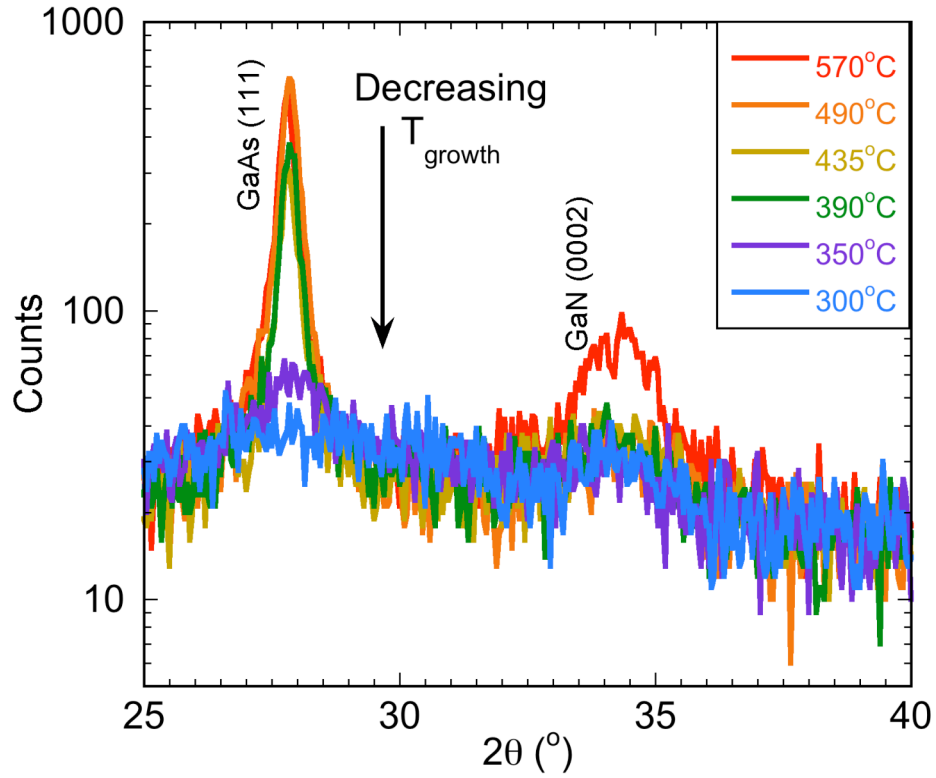


**Fig 3.5** XRD patterns from  $\text{GaN}_{1-x}\text{As}_x:\text{Mg}$  grown at different temperatures.

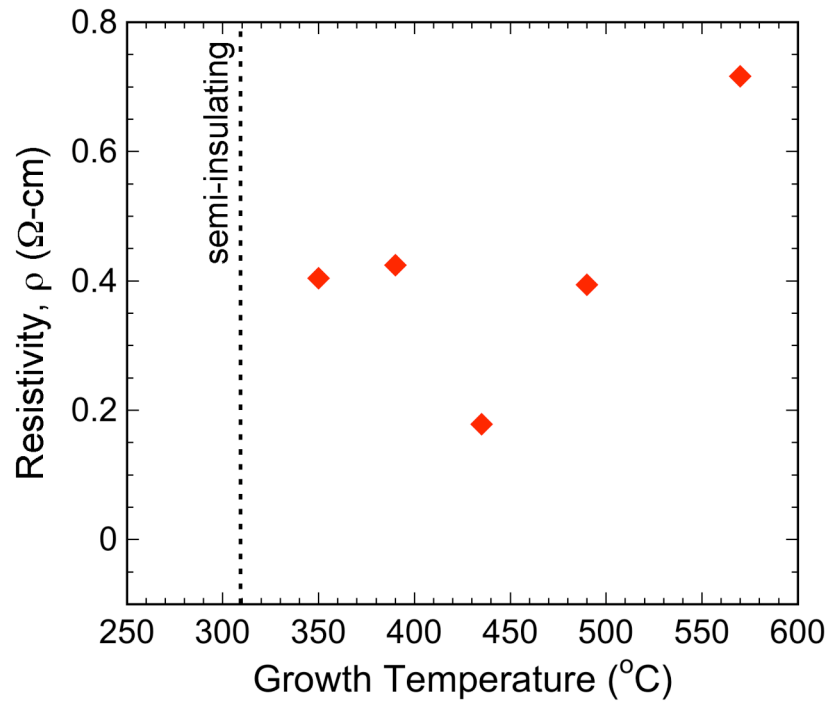


**Fig 3.6** Resistivity of  $\text{GaN}_{1-x}\text{As}_x:\text{Mg}$  as a function of growth temperature.

Increasing the As BEP at a constant temperature of 390°C decreases the crystal quality of the phase segregated c-GaN (Fig 3.7). This is expected due to the significant mismatch between arsenic and nitrogen. At intermediate As BEPs, both the GaAs (111) and GaN (0002) peak are suppressed. It is possible that these films are predominantly amorphous, however weak broad humps are still present and HR-TEM would be needed to confirm the fraction of amorphous phase. At high As BEPs, the GaAs (111) peak increases in height due to the formation of larger GaAs grains. The resistivity tends to decrease with higher As BEPs (Fig 3.8). The *p*-type doping of GaN with Mg is challenging and these low temperature growth conditions are not ideal for GaN growth. This explains why the samples grown at very low As BEPs are semi-insulating. As the film becomes more As-rich, the resistivity decreases.

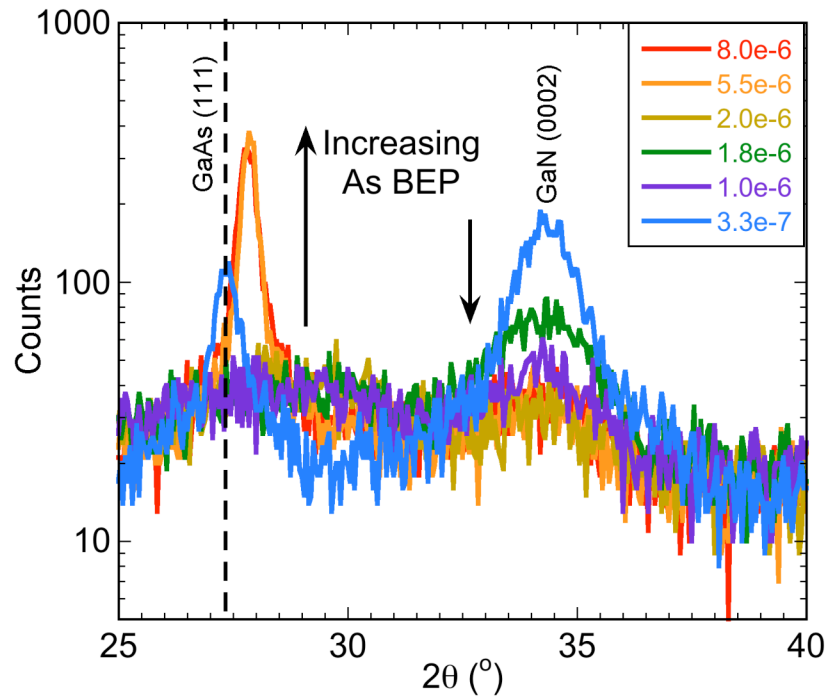


**Fig 3.7** XRD patterns of  $\text{GaN}_{1-x}\text{As}_x:\text{Mg}$  grown using different As BEPs. The pressures given in the legend are in Torr.

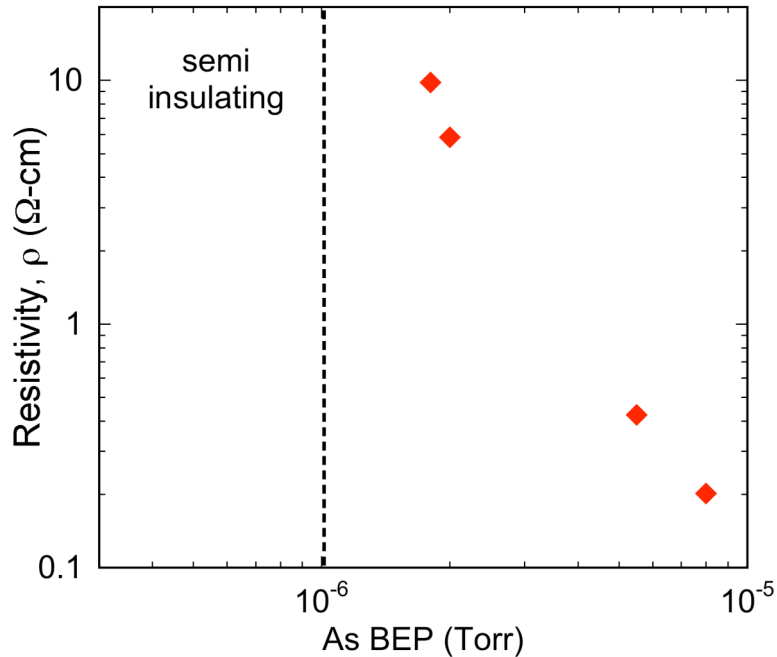


**Fig 3.8** Resistivity of  $\text{GaN}_{1-x}\text{As}_x\text{:Mg}$  as a function of As BEP. The dashed line indicates pressures below which the samples were semi-insulating.

Increasing the Ga BEP was required in order to enhance incorporation of Mg and cause an enhancement of conductivity. However, the increase in Ga BEP also provided a driving force for the formation of c-GaAs making a mixed phase system. The Ga BEP was varied while keeping other growth conditions constant in order to determine if the conductivity could be maintained while removing the remnant crystallinity. High Ga BEPs increased the incorporation of arsenic, likely due to the formation of c-GaAs (Fig 3.9). For the lowest Ga BEP the As content dropped off, but for intermediate Ga BEPs the As content was relatively insensitive to minor changes in the BEP. High Ga BEPs made the films metal rich with III:V ratios > unity (Fig 3.9). Oddly, decreasing the Ga BEP from intermediate values also caused an increase in the III:V ratio. This is due to the the Mg concentration increases to 15 at% and 20 at% for these two films and the assumption that Mg is on a Ga site when calculating the III:V ratio.

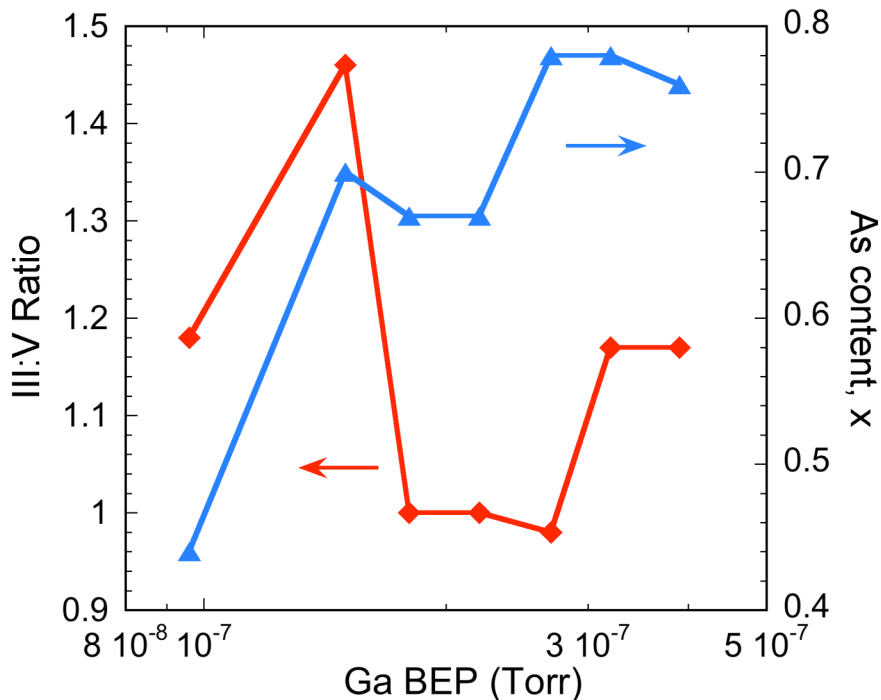


**Fig 3.9** Arsenic content and III:V ratio of  $\text{GaN}_{1-x}\text{As}_x\text{:Mg}$  as a function of Ga BEP.

Decreasing the Ga BEP resulting in decreased grain sizes for both GaAs and GaN according to the XRD patterns shown in Fig 3.10. For the two lowest Ga BEPs, the XRD peaks completely disappear with no residual broad humps observed in Fig 3.5 and Fig 3.7. These films are most likely amorphous, although HR-TEM is required to confirm. As the Ga BEP is decreased, the resistivity increases until the films become semi-insulating for the two lowest Ga BEPs (Fig 3.11). The transition from reasonable conductivity to semi-insulating is very abrupt and occurs within a small shift in the Ga BEP from  $\sim 1.8 \times 10^{-7}$  Torr to  $\sim 1.5 \times 10^{-7}$  Torr. This could be the critical Ga BEP range in the growth phase space where the film transitions from polycrystalline to amorphous.

The simultaneous disappearance of the XRD peaks and the conductivity is highly suspicious of the crystalline phase being responsible for the conductivity in the mixed phase  $\text{GaN}_{1-x}\text{As}_x$ . However, it is still possible that the change in the III:V ratio or other unknown variables affect the conductivity of these films. Hydrogenation of these films is a logical next step for determining whether incorporating hydrogen to passivate dangling bonds can enhance the conductivity of the amorphous phase.

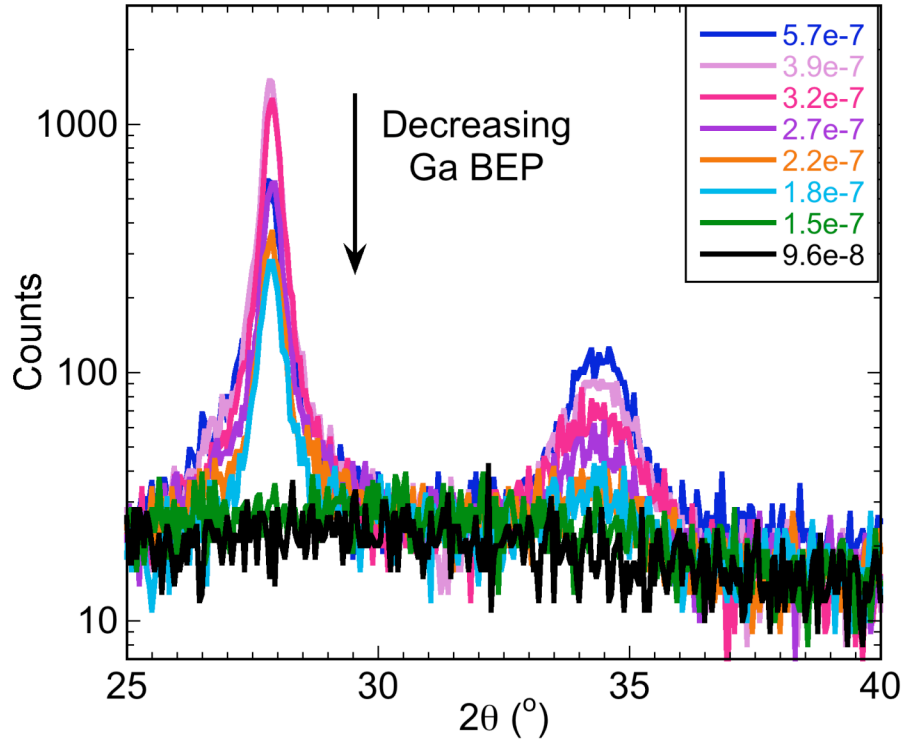


**Fig 3.10** XRD patterns of  $\text{GaN}_{1-x}\text{As}_x:\text{Mg}$  as a function of Ga BEP.

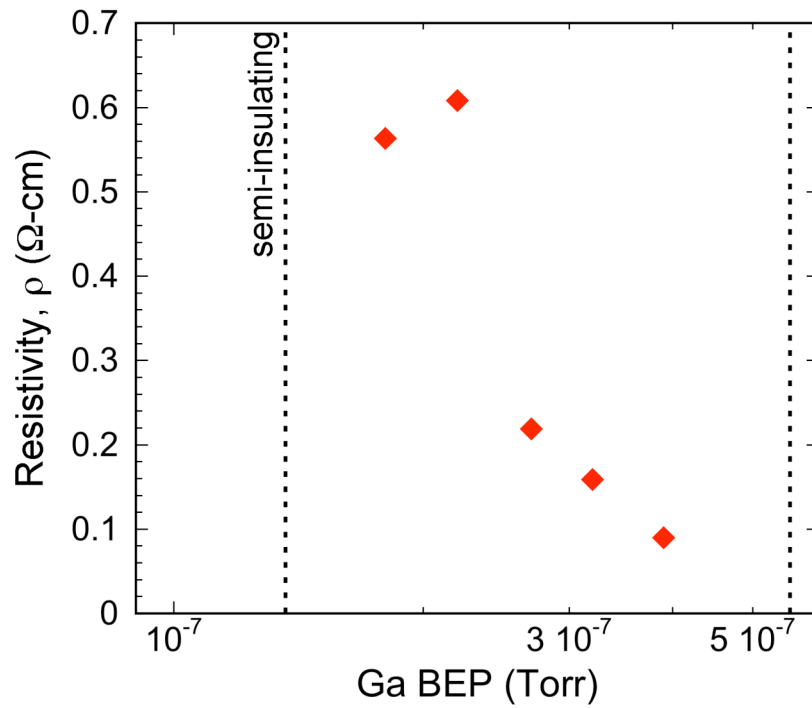


**Fig 3.11** Resistivity of  $\text{GaN}_{1-x}\text{As}_x:\text{Mg}$  as a function of Ga BEP.

## 4 Local structure of GaNAs

Amorphous materials are characterized by a lack of long-range order due to bond length disorder and the low formation energy of a dangling bond defect. Both of these structural factors can impede the ability to control electrical properties via doping due to Anderson localization from bond length disorder and the creation of mid-gap states from dangling bonds. *Ab initio* molecular dynamics calculations for amorphous GaN have suggested that the highly electronegative nitrogen may result in a lower density of mid-gap states (Stumm, 1997). Because of this, it was considered possible that the a-GaN<sub>1-x</sub>As<sub>x</sub> could have a uniquely high degree of short-range order.

Extended x-ray absorption fine structure (EXAFS) is a chemically sensitive structural probe that allows for the determination of the key structural parameters of bond length disorder and coordination of amorphous materials (Stern, 1975). This technique has been used extensively to study the structural properties of amorphous semiconductors, such as a-Si (and its alloys with Ge, C, and H), a-Ge, and compound semiconductors such as a-GaAs (Haskel, 2003; El Khakani, 1995; Knights, 1977; Wakagi 1994 & 1994b; Ridgway, 1998; Mousseau, 1993). Now the technique of EXAFS has been used to study the local structure of As and Ga atoms in a-GaN<sub>1-x</sub>As<sub>x</sub> to further develop our understanding of these amorphous highly mismatched semiconductor alloys. The chemical selectivity of the technique allows for the decoupling of bonding between Ga-N and Ga-As to independently determine the bond length disorder and dangling bond densities associated with these two different chemical bonds in the alloy.

The composition of the films examined was  $x \sim 0.65, 0.45, 0.15,$  and 0 with thicknesses in the range of 150-510 nm. Wavelength dispersive x-ray analysis has shown high lateral composition uniformity and atomic force microscopy characterization revealed a flat surface without voids (Yu, 2009). X-ray diffraction, electron diffraction, and high-resolution transmission electron microscopy characterization have confirmed that the GaN<sub>1-x</sub>As<sub>x</sub> samples examined in this study are amorphous. A fine powder of semi-insulating GaAs spread thinly and uniformly on Kapton tape and a thin film of crystalline GaN grown on sapphire were used as reference samples.

EXAFS measurements at the As *K* edge (11.88 keV) and Ga *K* edge (10.38 keV) were performed at the Stanford Synchrotron Radiation Laboratory at beamline 4-1 using a Si(220) double crystal monochromator at  $\phi = 90^\circ$  to minimize glitches in the measured energy range. The monochromator was detuned 30% to reduce the intensity of second harmonics. The samples were immersed in a liquid helium cryostat and cooled to 20 K prior to data collection to reduce the influence of thermal vibrations, which reduce the EXAFS amplitude. The initial x-ray intensity was measured using a nitrogen filled ionization chamber. Due to the 500  $\mu\text{m}$  thickness of the sapphire or glass substrates, EXAFS data for the thin films was collected in a fluorescence geometry using a thirteen-element liquid nitrogen cooled germanium detector (Jaklevic, 1977). EXAFS of the powder GaAs sample was collected in transmission mode using an argon filled ionization chamber to measure the x-ray intensity after passing through the sample. Numerous scans were collected and averaged together for each sample. The number of scans collected was

dependent on the composition of the film with more scans for lower As content samples when examining the As *K* edge.

All EXAFS data processing and analysis was performed using the Horae software analysis suite (Ravel, 2005). The pre-edge, post-edge, and spline fitting were performed to extract the experimental EXAFS function,  $\chi(k)$ , and the photon energy was converted into photoelectron momentum ( $k$ ) using  $k = \sqrt{2m(E - E_0)/\hbar^2}$ , where  $E$  is the photon energy,  $E_0$  is the absorption edge threshold. The absorption edge threshold was selected as the maximum of  $d\mu(E)/dE$ , near the middle of the edge step.

The  $\chi(k)$  was Fourier transformed into  $r$ -space across a  $k$  range of 2-12  $\text{\AA}^{-1}$  or 2-13  $\text{\AA}^{-1}$  depending on data quality, using a Hanning window with a  $dk$  of 2  $\text{\AA}^{-1}$ . The number of independent points [ $N_I = (2\Delta k\Delta r)/\pi + 2$  where  $\Delta k$  and  $\Delta r$  are the fitting regions in  $k$  and  $r$ -space respectively] was kept well above the number of variables used in the fitting. An overall  $E_0$  shift fitting parameter was used to fit minor adjustments of  $k = 0$ . The fractional misfit  $R$  factor was used to evaluate the quality of the fit. The  $R$  factor is defined as the square of the difference between the data value and the fit value, reduced by the square of the data value. Analysis was completed using the single-scattering approximation, ignoring multiple-scattering paths (Newville, 1995). The lack of significant improvement in  $R$  factor when including multiple scattering was used as justification for only using single-scattering paths. This was especially true for the amorphous samples in which there was significant EXAFS data only for the first coordination shell due to the structural disorder.

The raw absorption data for the As *K* edge for c-GaAs collected in transmission mode and for a-GaN<sub>0.55</sub>As<sub>0.45</sub> collected in fluorescence mode are shown in Fig 4.1 & Fig 4.2. The extracted  $\chi(k)$  function for all As containing samples is shown in Fig 4.3 (points). The lines are the result of fits to the data. Uncertainty in background subtraction limits the lower usable  $k$  range to about 2  $\text{\AA}^{-1}$  and noise in the data limited the upper usable  $k$  range to approximately 13  $\text{\AA}^{-1}$ . Fits were determined by Fourier transforming the  $\chi(k)$  across a  $k$ -range of 2-13  $\text{\AA}^{-1}$  and simultaneously fitting  $k^w$ -weighted data ( $w = 1, 2, 3$ ) using a single set of structural parameters. For the c-GaAs sample  $\Delta r = 1-4.8 \text{\AA}^{-1}$  including the first three coordination shells, whereas for a-GaN<sub>1-x</sub>As<sub>x</sub> samples the fitting space was constrained to  $\Delta r = 1.6-2.6 \text{\AA}^{-1}$  to fit only the first coordination shell. To determine the amplitude reduction factor ( $S_0^2$ ) for the As *K* edge, the coordination of the c-GaAs sample was fixed at known values and an iterative fit was performed to define  $S_0^2 = 1.01$  (Ridgway, 1998).

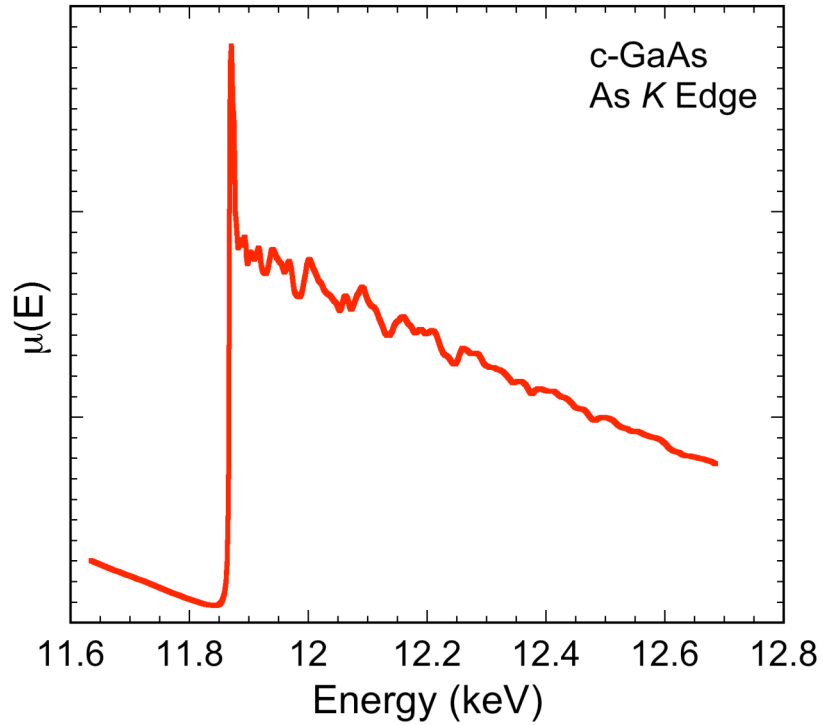


**Fig 4.1** Raw absorption coefficient data collected in transmission mode for powder c-GaAs at the As *K* edge at  $T = 20$  K.

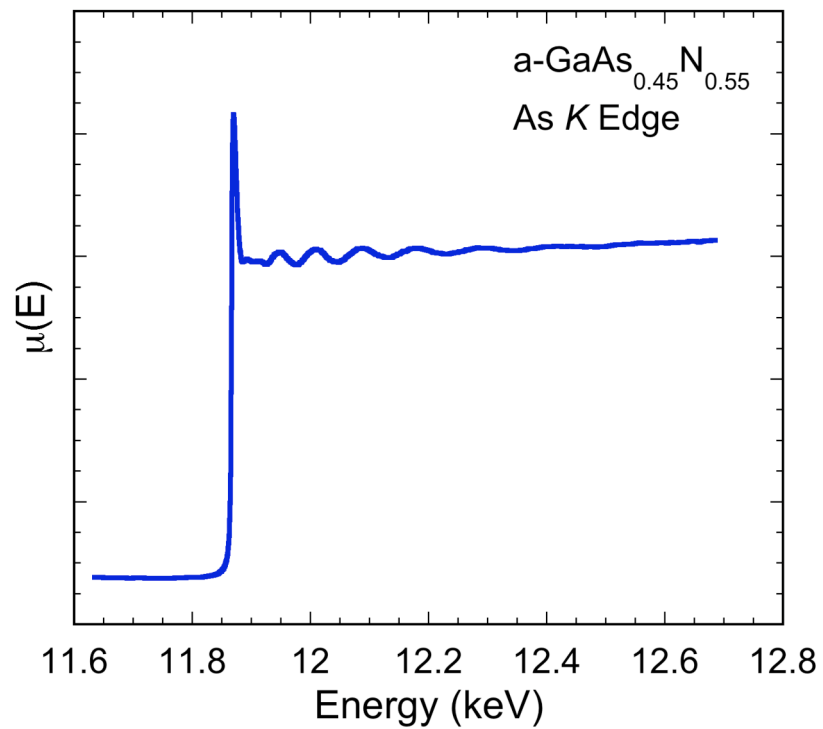


**Fig 4.2** Raw absorption coefficient data collected in fluorescence mode for a thin film of a-GaN<sub>0.55</sub>As<sub>0.45</sub> on a glass substrate at the As *K* edge at  $T = 20$  K.

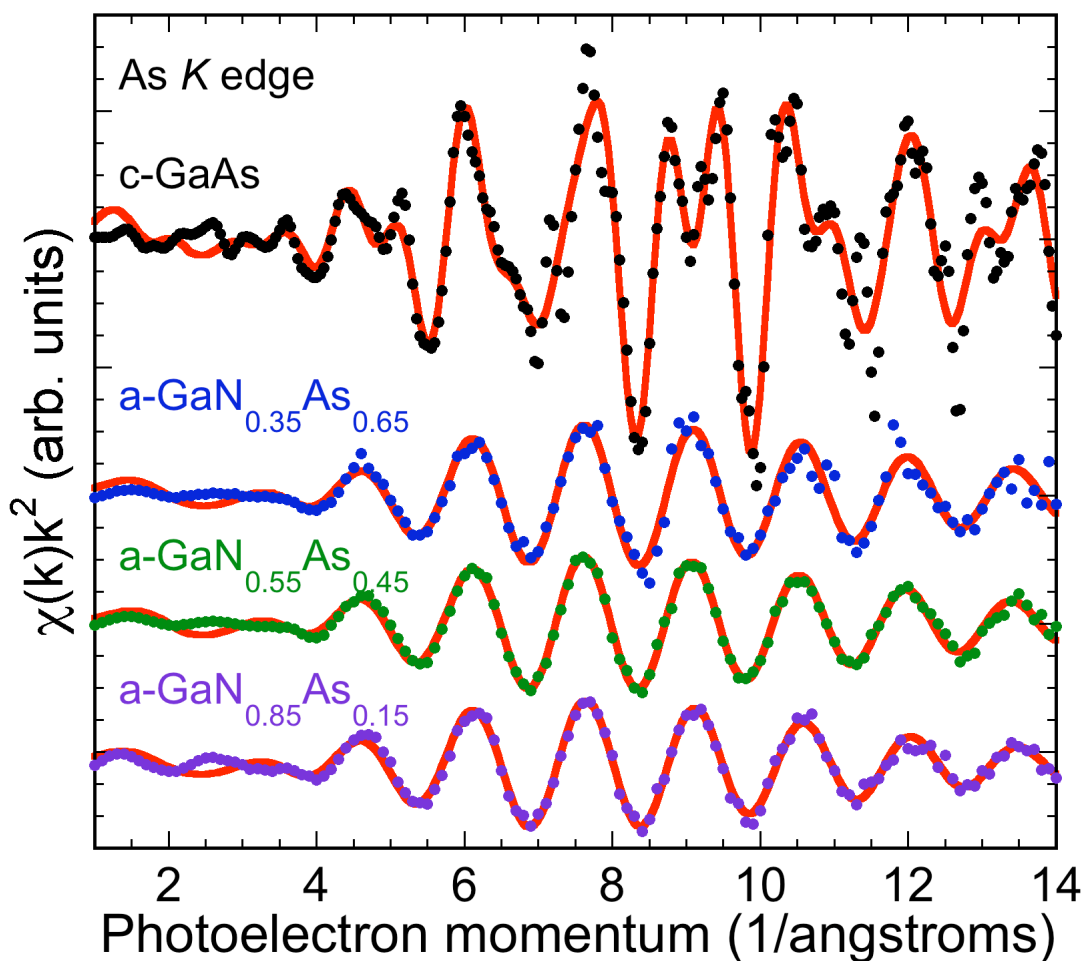


**Fig 4.3** EXAFS function data (points) extracted from absorption coefficient data weighted by  $k^2$  along with fits (lines) for c-GaAs and a-GaN<sub>1-x</sub>As<sub>x</sub> at different compositions from As K edge data. For amorphous samples 50% of data points are shown to enhance clarity.

The complex structure of the  $\chi(k)$  for c-GaAs is caused by the multiple coordination shells, which becomes evident in the Fourier transform. The  $\chi(k)$  of the amorphous samples contains only one frequency due to disorder dampening contributions from coordination shells beyond the nearest neighbors. Fig 4.4 compares the  $k^2$ -weighted Fourier transform of the c-GaAs reference sample (points) and the a-GaN<sub>0.55</sub>As<sub>0.45</sub> sample (points) along with their corresponding fits (lines). Scattering from the first, second, and third nearest neighbors of the absorbing As atom in c-GaAs are evident in the Fourier transform. The single frequency of the  $\chi(k)$  for the amorphous samples is converted to a single peak in  $r$ -space corresponding to the first nearest neighbor, in this case a Ga atom.

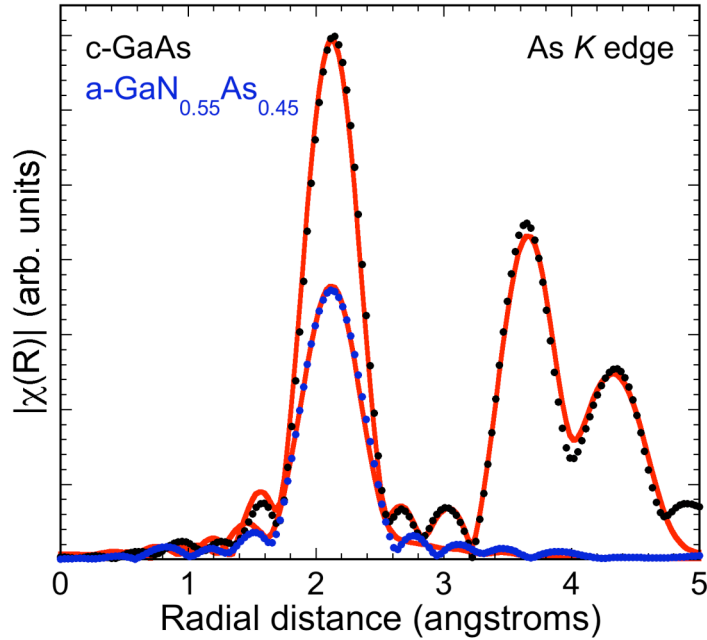


**Fig 4.4** Magnitude of Fourier transform of  $k^2\chi(k)$  for c-GaAs and a-GaN<sub>0.55</sub>As<sub>0.45</sub> for data (points) and fits (lines). Fitted region in  $r$ -space was 1-4.8 Å for c-GaAs and 1.6-2.6 Å for a-GaN<sub>0.55</sub>As<sub>0.45</sub>. For the amorphous sample, no EXAFS is detected beyond the first coordination shell.

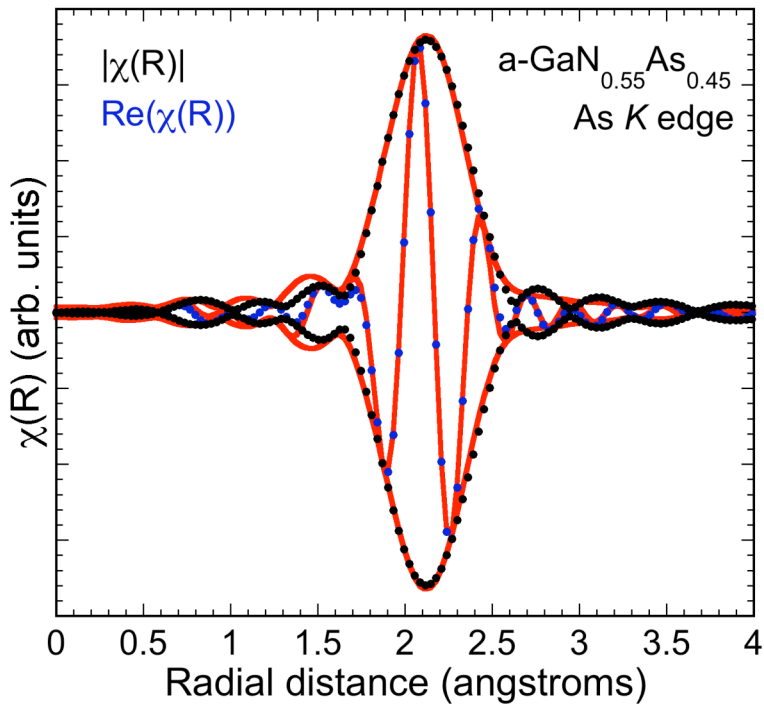


**Fig 4.5** Magnitude and real part of the Fourier transform of  $k^2\chi(k)$  for a-GaN<sub>0.55</sub>As<sub>0.45</sub> to show quality of fit.

The numerical evaluation of bond length ( $r$ ), coordination number ( $N$ ), and Debye-Waller disorder parameter ( $\sigma^2$ ) for the As environment for different samples is presented in Table 4.1 along with statistical parameters (reduced chi-squared ( $\chi_v^2$ ), and  $R$  factor) to show the quality of fit achieved. There is no significant change in bond length between crystalline and amorphous samples, both of which agree with c-GaAs reference values (Stevenson, 1994). The uncertainty in the bond length was approximately  $\pm 0.009$  Å. Compared with a crystalline coordination of four, the EXAFS analysis reveals a coordination of  $\sim 2.8$  for the amorphous samples. The coordination of the As atoms for these amorphous semiconductor alloys is significantly lower than the coordination of a-GaAs films formed by implantation amorphization and a-Si:H, which has been reported to be in the range of 3.6-3.8 (Ridgway, 1998). The density reduction observed in previous studies of these materials is most likely caused by the lower coordination of the As atoms (Yu, 2010). The  $\sigma^2$  parameter tends to increase with decreasing As content. This can be interpreted to mean that the higher nitrogen content further distorts the As local environment resulting in an increase in disorder. The  $N$  and  $\sigma^2$  parameters as a function of As content for the As environment are graphically summarized in Fig 4.6. The fit quality, as evaluated by the  $R$  factor, degraded slightly with decreasing As content as the density of absorbing atoms in the thin film decreased causing a slight decrease in the statistical quality of the data. Despite this degradation, all of the  $R$  factors are low enough to have high confidence in the fit quality.

**Table 4.1** Structural and statistical fit parameters from As *K* edge data for As-Ga distance in c-GaAs, and a-GaN<sub>1-x</sub>As<sub>x</sub> at T = 20 K.  $S_0^2 = 1.01$

x	$r(\text{\AA})$	$N$	$\sigma^2(\text{\AA}^2)$	$\chi_v^2$	$R$
1	2.44	4	0.0025(0.0004)	55	0.007
0.65	2.44	2.73(0.33)	0.0035(0.0007)	85	0.005
0.45	2.44	2.85(0.51)	0.0039(0.001)	280	0.008
0.15	2.43	2.81(0.59)	0.0047(0.001)	215	0.016

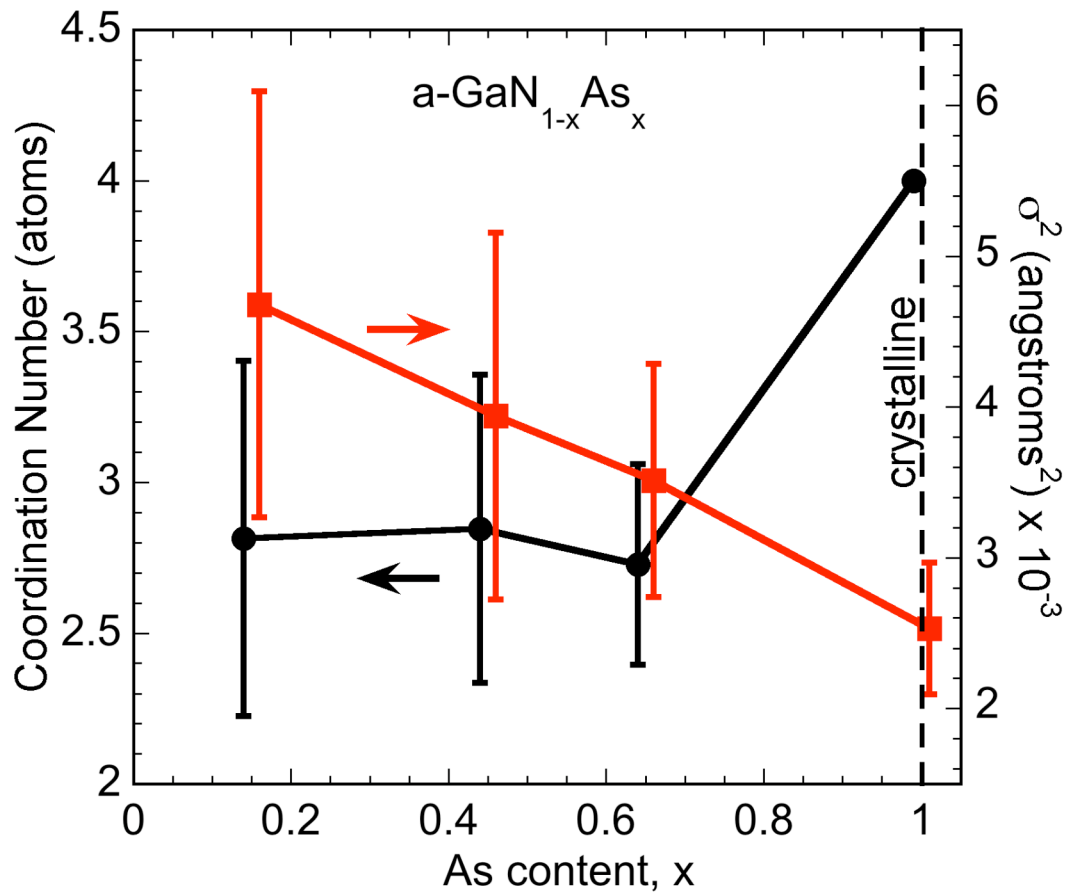


**Fig 4.6** Graphical representation of key structural parameters determined by EXAFS analysis for As atom local environment.

The Ga  $K$  edge was also examined under the same conditions as the As  $K$  edge in order to develop a deeper understanding of the local bonding environment. The  $\chi(k)$  data (points) for all of the samples examined along with the corresponding fits (lines) are shown in Fig 4.7. To determine  $S_0^2$  for the Ga  $K$  edge, a crystalline GaN thin film sample was used as a reference. The Ga atom local environment is complicated by the fact that Ga can be bonded to either nitrogen or arsenic. Therefore, two sets of structural parameters ( $r$ ,  $N$ ,  $\sigma^2$ ) were required to describe the bonding to nitrogen and arsenic, along with a constant describing the alloying fraction as determined from RBS analysis.

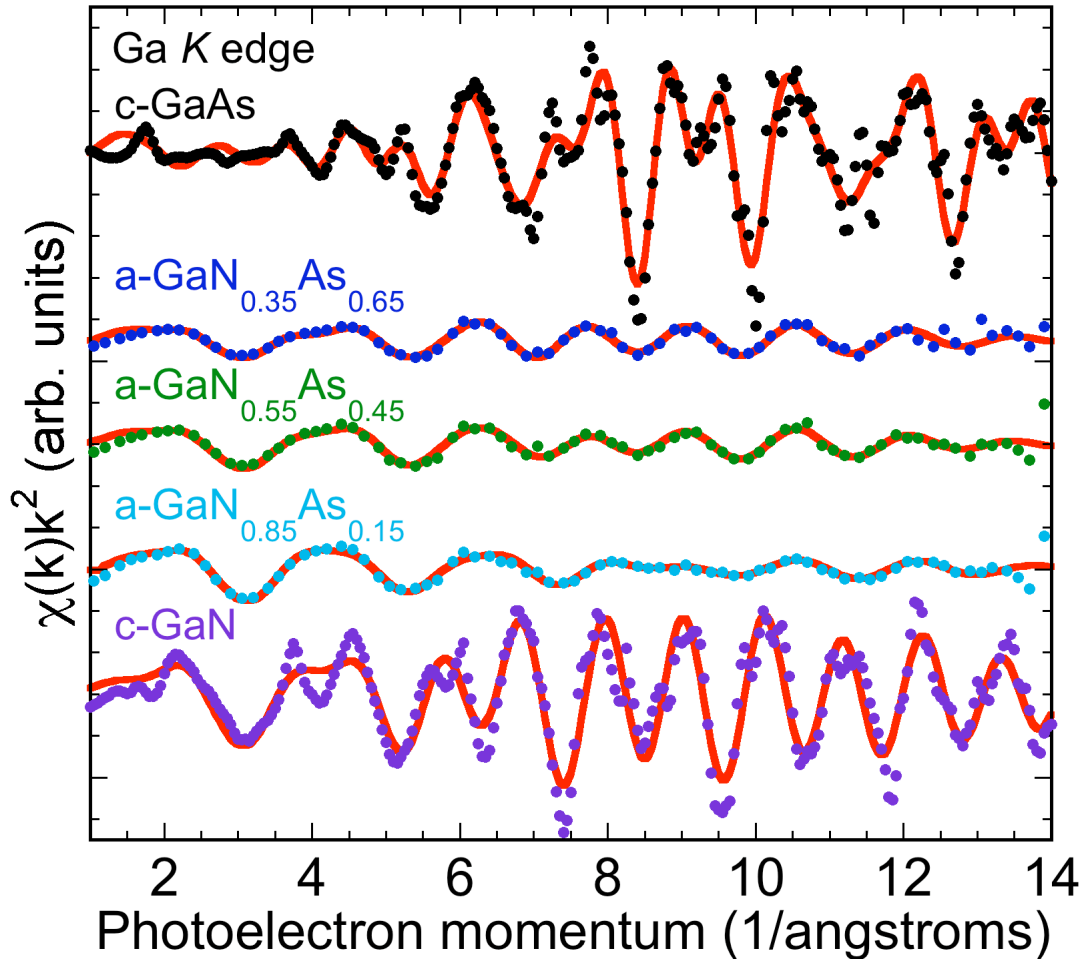


**Fig 4.7** EXAFS function data (points) extracted from absorption coefficient data weighted by  $k^2$  along with fits (lines) for c-GaAs, c-GaN, and a-GaN<sub>1-x</sub>As<sub>x</sub> at different compositions from Ga  $K$  edge data. For amorphous samples 30% of data points are shown to enhance clarity.

Although there appears to be only one frequency in the  $\chi(k)$  of the amorphous samples shown in Fig 4.7, the Fourier transform of  $\chi(k)$  for a-GaN<sub>0.55</sub>As<sub>0.45</sub> shown in Fig 4.8 clearly has two peaks at different radial distances. These two peaks correspond to Ga-N bonds at the shorter distance (1.92 Å) and Ga-As bonds at the longer distance (2.45 Å). The Ga-N bond length agrees with reference data and does not change with composition (Marasina, 1971). Once again the real part and the magnitude of the Fourier transform are

shown to demonstrate the quality of fit for the more complex bonding environment. The inset of Fig 4.8 shows the magnitude of the Fourier transform for the c-GaN reference. Multiple coordination shells are visible due to the long-range order present in the crystalline reference.

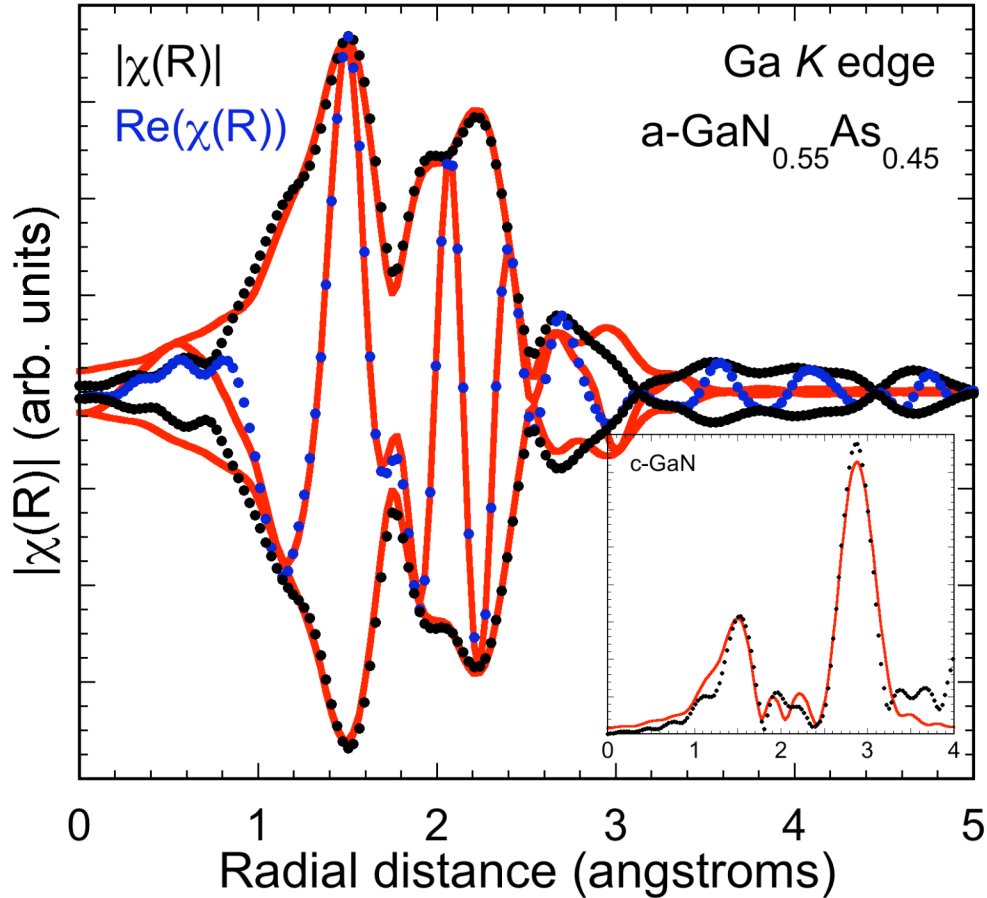


**Fig 4.8** Magnitude and real part of Fourier transform of  $k^2\chi(k)$  for a-GaN<sub>0.55</sub>As<sub>0.45</sub> for data (points) and fits (lines). Fitted region in  $r$ -space was 0.8-3.1 Å. (Inset) Magnitude of Fourier transform of  $k^2\chi(k)$  for c-GaN for data (points) and fit (line). Fitted region in  $r$ -space was 1.2-3.2 Å.

The relevant structural information determined from the EXAFS fitting is shown in Table 4.2 for Ga-N bonds and in Table 4.3 for Ga-As bonds. As was the case for the arsenic bonding, the radial distance of the coordination shells was not found to change appreciably with alloying content. This agrees with previous work examining the bond length of III-V alloys at different compositions, which showed a bimodal bond length distribution revealed by EXAFS despite the single lattice parameter from diffraction experiments (Mikkelsen, 1982 & 1983). The normalized coordination numbers for N-related bonds ( $N_N$ ) and As-related bonds ( $N_{As}$ ) were significantly lower than the crystalline reference samples. The normalized coordination numbers were weighted by the alloying content during the analysis such that a  $N_N$  and  $N_{As}$  of four would indicate that each Ga atom was on average bonded to two nitrogen atoms and two arsenic atoms for an

a-GaN<sub>0.50</sub>As<sub>0.50</sub> sample. The normalized coordination values are shown as a function of composition in Fig 4.9. The  $N_N$  of  $\sim 3.5$  was higher than  $N_{As}$  for all compositions of the amorphous phase, but  $N_{As}$  agreed with the coordination of As atoms determined in the previous section, which is a good validation of the analysis. The value of  $N_N$  was similar to  $N$  values reported in the literature for other amorphous semiconductors (Ridgway, 1998; Haskel, 2003).

**Table 4.2** Structural and statistical fit parameters from Ga  $K$  edge data for Ga-N distance in c-GaN, and a-GaN<sub>1-x</sub>As<sub>x</sub> at T = 20 K.  $S_0^2 = 0.63$

x	$r(\text{\AA})$	$N$	$\sigma^2(\text{\AA}^2)$	$\chi_v^2$	$R$
1	N/A	N/A	N/A	153	0.022
0.65	1.92	3.51(0.52)	0.0012(0.002)	44	0.011
0.45	1.91	3.52(0.34)	0.0025(0.0015)	66	0.014
0.15	1.92	3.11(0.23)	0.0025(0.0013)	171	0.013
0	1.92	4	0.0019(0.0025)	190	0.026

**Table 4.3** Structural and statistical fit parameters from Ga  $K$  edge data for Ga-As distance in c-GaAs, and a-GaN<sub>1-x</sub>As<sub>x</sub> at T = 20 K. Statistical parameters listed in Table II.  $S_0^2 = 0.63$

x	$r(\text{\AA})$	$N$	$\sigma^2(\text{\AA}^2)$
1	2.45	4	0.0007(0.0003)
0.65	2.45	2.77(0.58)	0.0045(0.001)
0.45	2.45	3.00(0.71)	0.0037(0.001)
0.15	2.42	2.28(1.69)	0.001(0.004)
0	N/A	N/A	N/A

The mean square disorder parameter for the Ga  $K$  edge analysis is shown as a function of composition in Fig 4.10. The  $\sigma^2$  parameter was significantly lower for N-related bonds compared to As-related bonds and similar to the  $\sigma^2$  value for the crystalline reference samples. There is a third feature in the Fourier transform of the a-GaN<sub>0.55</sub>As<sub>0.45</sub>  $\chi(k)$  shown in Fig 4.8 at  $\sim 2.7$   $\text{\AA}$ , which corresponds to the second nearest neighbor of Ga atoms bonded to nitrogen (a Ga atom in the second coordination shell). This feature is visible due to the lower disorder of the Ga-N bond compared to the Ga-As bond.

The lower density of N-related dangling bonds and lower mean square disorder of N-related bonds can be explained by the higher electronegativity of the N atom (Gordy, 1956). The higher electronegativity compared to As results in a stronger bond with higher energetic driving force for formation. This causes the material to preferentially satisfy N-related bonds over As-related bonds resulting in lower N-related dangling bond densities. The stronger Ga-N bond is also a tighter bond with less mean square deviation about the equilibrium value.

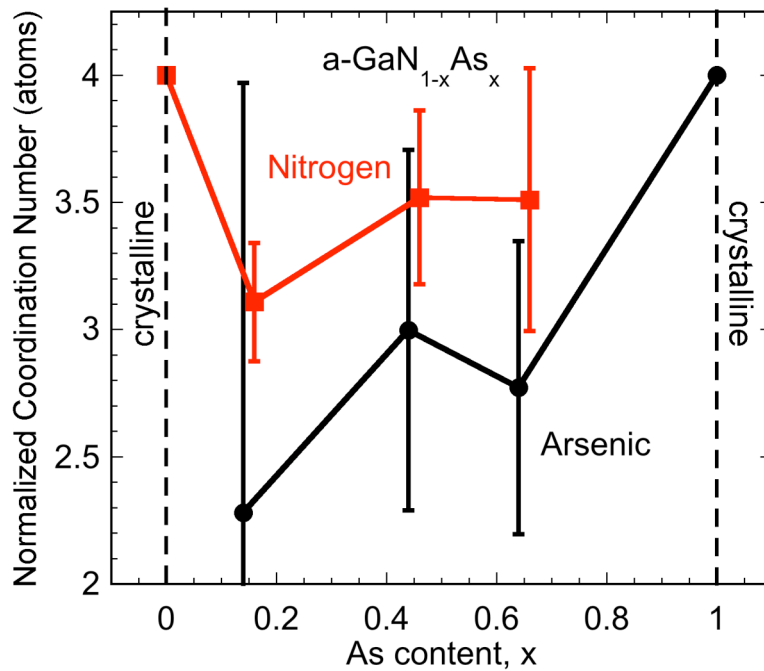


**Fig 4.9** Graphical representation of Ga coordination number determined by EXAFS analysis for first nitrogen shell (squares) and first arsenic shell (circles). The coordination number shown is multiplied by the alloying content to determine the actual number of nitrogen or arsenic atoms bonded to a given Ga atom.

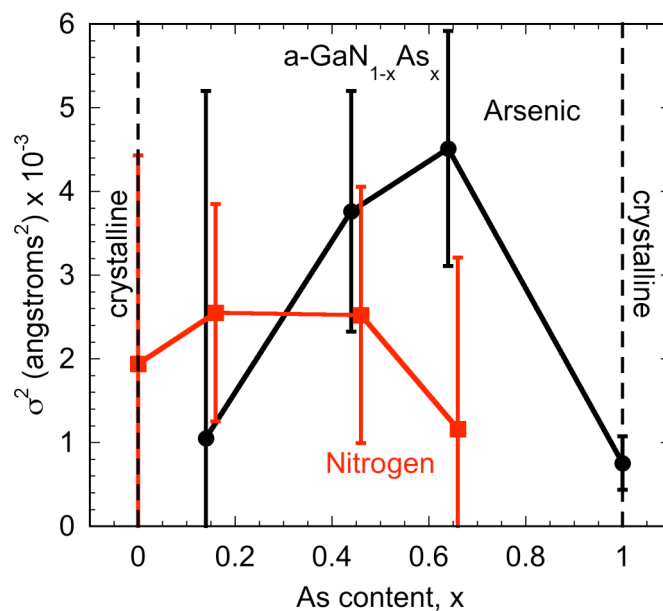


**Fig 4.10** Graphical representation of Ga  $\sigma^2$  determined by EXAFS analysis for first nitrogen shell (squares) and first arsenic shell (circles). The results suggest that there are fewer dangling bonds and less bond length disorder due to nitrogen in the amorphous alloy.

## 5 Amorphous GaNBi

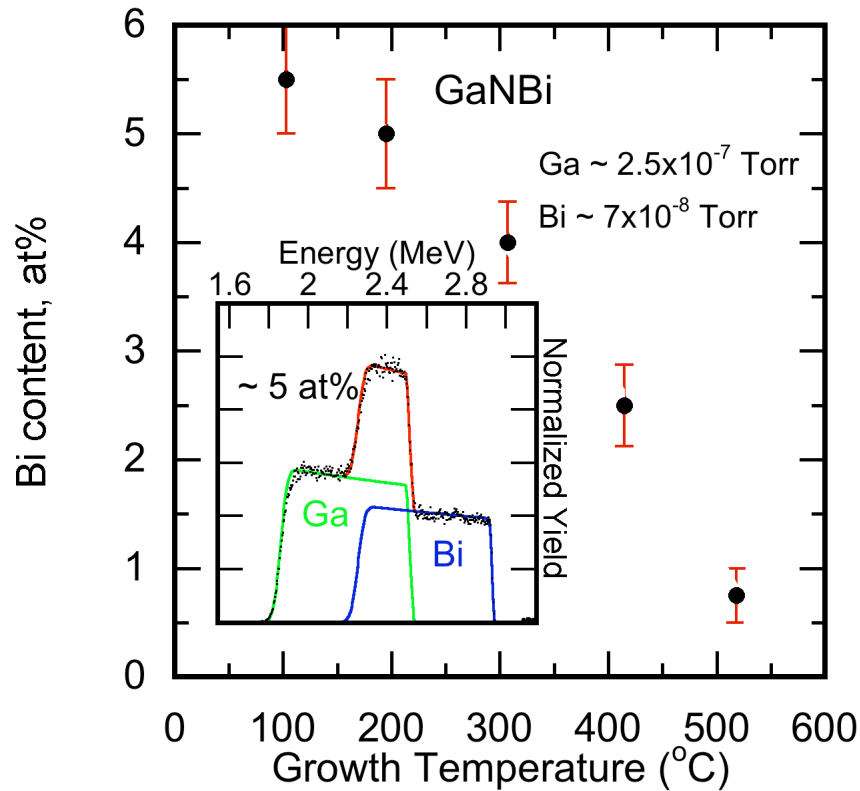
### 5.1 Growth and structure

Incorporating bismuth into semiconductor alloys is a challenging task, especially if it is a nitride or phosphide material due to the mismatch between these anions. Extensive work has been conducted on As-rich  $\text{GaAs}_{1-x}\text{Bi}_x$  HMAs where the electronic bands are strongly restructured due to the isoelectronic substitution of a host anion with a mismatched anion (Francoeur, 2003; Bertulis, 2006; Fluegel, 2006; Alberi, 2007). As-rich  $\text{GaN}_x\text{As}_{1-x-y}\text{Bi}_y$  has been studied for photovoltaic applications for the development of a 1 eV band gap material that is lattice matched to GaAs (Janotti, 2002; Huang, 2005; Tixier, 2005). In addition, Bi in Group III-V semiconductors has been used as a surfactant during growth to improve surface morphology (Foxon, 2002; Tixier, 2003). Given the electronegativity, N (3.0) and Bi (1.8), as well as atomic radius, N (75 pm) and Bi (155 pm), mismatches are the largest among all Group V elements, a dramatically different electronic band structure is expected to result from an N-rich  $\text{GaN}_{1-x}\text{Bi}_x$  alloy (Gordy, 1956).

Attempts to incorporate significant amounts of Bi into GaN have not been successful (Novikov, 2003). Therefore, the GaNBi films were grown using a similar approach as that used to grow the  $\text{GaN}_{1-x}\text{As}_x$  alloys, in particular, a low substrate temperature during growth. The films were grown on c-plane sapphire substrates using plasma-assisted molecular beam epitaxy. The growth temperature range spanned  $\sim 80 - 670^\circ\text{C}$ . The nitrogen ( $\text{N}_2$ ) beam equivalent pressure (BEP) was kept constant at  $\sim 1.7 \times 10^{-5}$  Torr with active nitrogen provided by a RF plasma source. The Ga BEP was varied between  $1.7 \times 10^{-7} - 3.1 \times 10^{-7}$  Torr, which modified the III:V ratio. The Bi BEP was used to control the Bi content of the film and varied from  $0 - 1.5 \times 10^{-7}$  Torr.

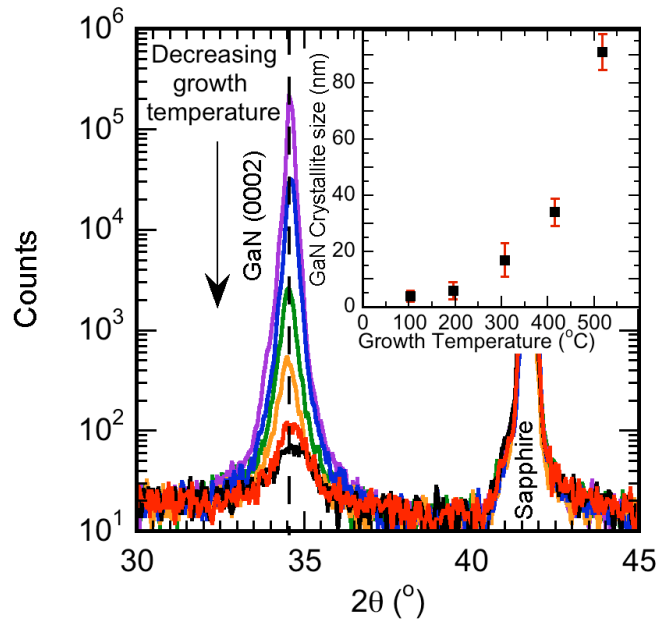
The composition, depth uniformity, and thickness of these films was characterized using RBS using a 3.04 MeV  $\text{He}^{2+}$  beam to detect oxygen contamination. The detectable limit of oxygen by this method is  $\sim 1$  at%. Atomic percentages of bismuth are used in this report due to the ambiguity of the bonding environment of the Bi atoms (e.g. possible Bi clusters), especially at high Bi concentrations. The structure of the low-temperature grown films was examined by XRD using a powder x-ray diffractometer. The microstructure of the GaNBi films was investigated TEM, SAD, and HR-TEM.

Fig 5.1 shows the monotonic increase in Bi concentration in the GaNBi films as a function of decreasing growth temperature with a representative RBS spectrum in the inset. The amount of Bi in the film appears to saturate for a given BEP, but this could be overcome by increasing the Bi flux. No measurable Bi ( $< 0.01\%$ ) can be detected for samples grown at a temperature above  $670^\circ\text{C}$ .



**Fig 5.1** The bismuth composition in GaNBi measured by RBS as a function of LT-MBE growth temperature. The III-V ratio was approximately 1:1 and the films were homogeneous in the growth direction within the resolution limit of RBS. Inset contains a representative RBS spectrum for a film with ~ 5 at% Bi. The blue, green, and red lines correspond to the Bi, Ga, and total simulated contributions to the spectrum.

The XRD patterns in Fig 5.2 show the presence of a GaN phase with decreasing crystallinity with lowering growth temperature. There is no shift in the GaN (0002) peak indicating low Bi incorporation into this crystalline phase, in contrast with the less mismatched N-rich GaN<sub>1-x</sub>As<sub>x</sub> system (Yu, 2009). Since no other XRD peaks of a new crystalline phase were observed, the Bi is most likely distributed in an amorphous GaNBi alloy phase. Due to the high atomic scattering factor of Bi, XRD should be able to detect crystalline Bi precipitates in the atomic % range. The monotonic decrease of the GaN (0002) peak intensity and increase in the peak width as growth temperature decreases suggest that the fraction and size of these GaN crystals decrease with decreasing growth temperature. The crystallite size was estimated using the Scherrer equation, and the result is contained within the Fig 5.2 inset (Cullity, 2001). The breadth of the GaN (0002) peak from the highest temperature growth was attributed to instrumental broadening and was subtracted from the breadth of the other peaks. At the lowest growth temperature (T ~ 100°C) GaN nanocrystals (~ 5 nm diameter) are present in an amorphous GaNBi matrix.



**Fig 5.2** XRD patterns from the GaNBi films grown at various temperatures. Crystalline GaN with no Bi incorporated is present even at the lowest growth temperature. GaN Crystallite size as a function of growth temperature determined from peak breadth contained in inset.

The structure of the GaNBi films grown at different temperatures was examined using cross sectional TEM, as shown in Fig 5.3. For films grown at 400°C, a columnar growth morphology occurred, with columns of oriented GaN and Bi segregated to the column boundaries. As the growth temperature decreases to 200°C, the columnar morphology transitions to a granular morphology with small GaN crystallites. The TEM results highlight the difficulty of incorporating Bi into crystalline GaN.

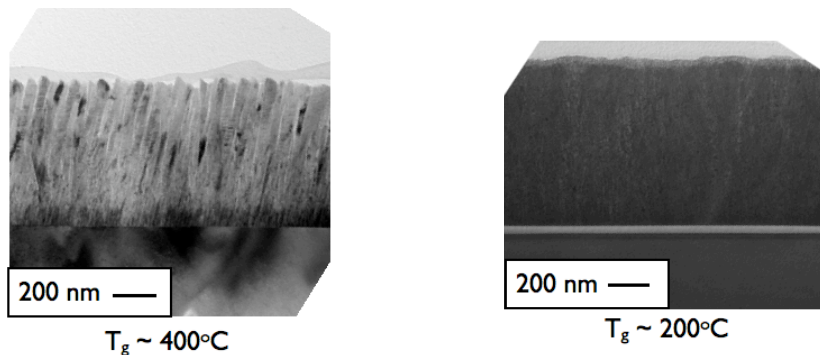


**Fig 5.3** Cross-sectional TEM images of GaNBi films grown at 400°C or 200°C. The morphology of the crystalline GaN in the film transitions from columnar to granular as the temperature decreases.

The growth optimization process was continued in an attempt to form a homogeneous GaN<sub>1-x</sub>Bi<sub>x</sub> alloy phase by growing at a low temperature of 80-90°C and varying the Ga and Bi BEP. Modifying the Ga BEP had a dramatic effect on the III:V ratio of the alloy, oxygen content, and optical absorption. In this context, the III:V ratio is defined as the atomic concentration of Ga divided by the sum of the atomic concentrations of Bi and N. Fig 5.4 shows how the III:V ratio in the GaN<sub>1-x</sub>Bi<sub>x</sub> layer measured by RBS increases with increasing Ga BEP for a given Bi BEP of  $7.2 \times 10^{-8}$  Torr, corresponding to ~6.5 at% Bi (or ~11 mol% GaBi) incorporated in the film. It is shown that a stoichiometric III:V ratio of unity within +/- 3% can be obtained for a narrow range of Ga BEP. The change in oxygen content in the bulk of the film is shown in Fig 5.5. The oxygen content increases with decreasing Ga BEP most likely due to the columnar growth, despite the relative cleanliness of the MBE growth chamber remaining constant. When a III:V ratio of unity or higher is reached, oxygen incorporation is suppressed.

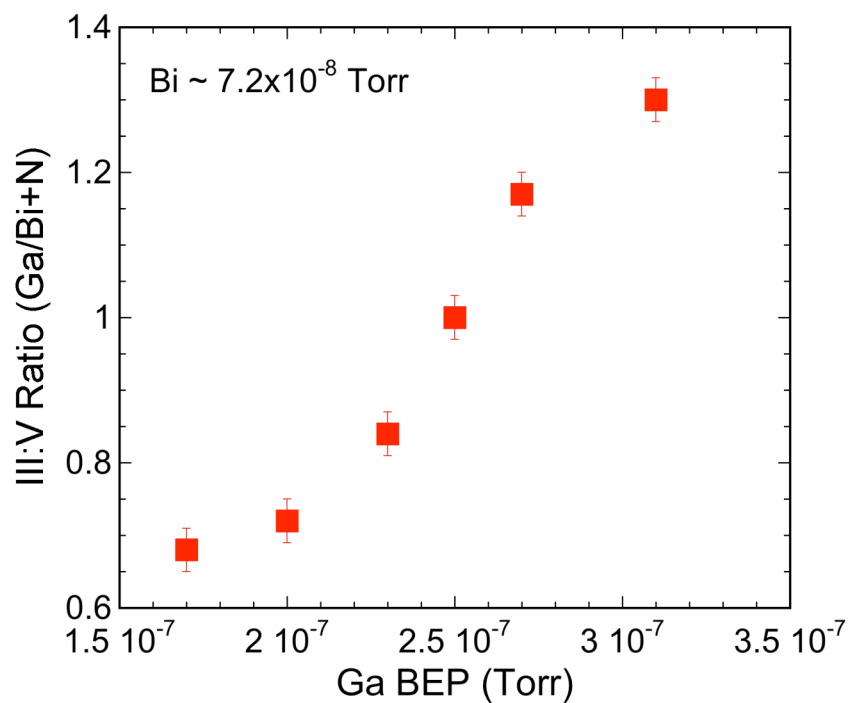


**Fig 5.4** III:V ratio in GaNBi layers, defined as the atomic concentration of Ga divided by the sum of the atomic concentration of Bi and N measured by RBS as a function of Ga BEP during growth.

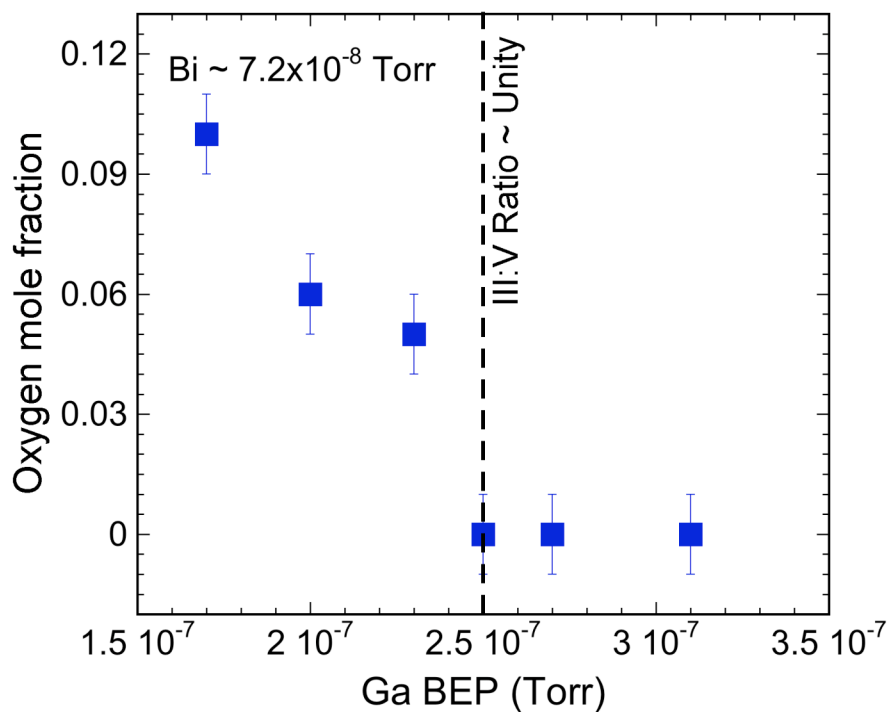


**Fig 5.5** The oxygen content in the bulk of the film as determined by resonance RBS. Note that oxygen incorporation is suppressed when RBS determined III:V  $\geq 1$ .

In addition to varying the bismuth content in the GaNBi alloy by varying the growth temperature as shown in Fig 5.1, the alloy composition can also be controlled by changing the Bi BEP during growth (Fig 5.6). Up to 12.5 at% Bi (or 25 mol% of GaBi) was achieved for the highest Bi BEP while maintaining a III:V ratio of approximately unity within +/- 3%. Even for the high concentration of ~ 12.5 at% Bi, the composition depth profile was uniform. In principal, higher Bi contents could be achieved; however for the current growth temperatures Bi surface segregation and depth non-uniformity was observed for Bi contents above 12.5 at% Bi.

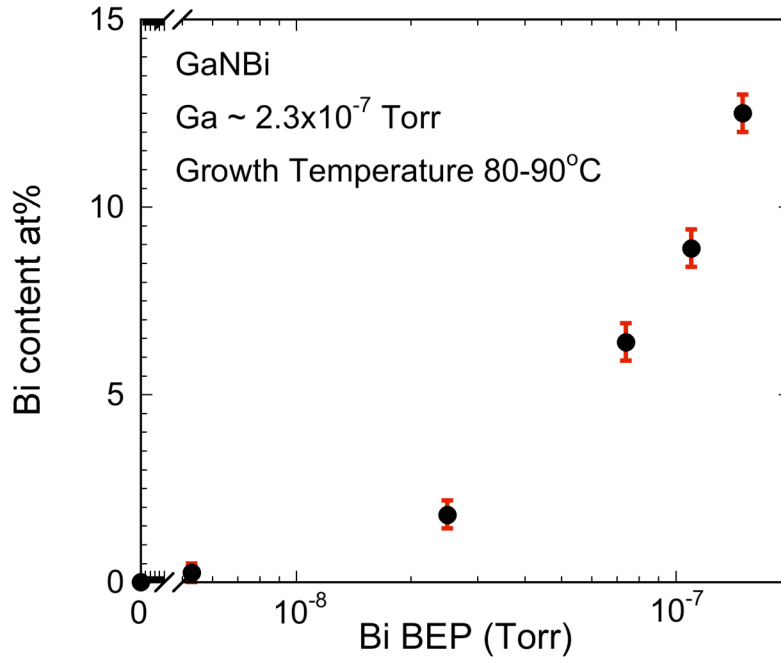


**Fig 5.6** The change in bismuth concentration as a function of Bi BEP. Even at high Bi at%, the composition profile is uniform indicating minimal segregation of Bi to the surface.

The result of increased Bi BEP is a decreased intensity of the GaN (0002) observed in XRD, as shown in Fig 5.7(a). There is no shift of this diffraction peak so we conclude no significant amount of Bi is incorporated into crystalline GaN despite the very low growth temperature. No other diffraction peaks are present. At a Bi BEP of  $7.4 \times 10^{-8}$  Torr, corresponding to a film composition of 6.5 at% Bi, the GaN (0002) diffraction peak is no longer detectable in conventional XRD using  $K_{\alpha}$  x-rays generated from a Cu tube source. More sensitive experiments to determine the structure of these alloys were carried out using transmission electron microscopy. The SAD pattern [Fig 5.7(b)] shows diffuse rings with positions corresponding to crystalline GaN. The high resolution electron microscopy [Fig 5.7(c)] reveals that there are nanocrystallites < 5 nm in diameter present – most likely cubic GaN (Liliental-Weber, 2012). Even at higher Bi BEP ( $1.1 \times 10^{-7}$  Torr), there are still nanocrystallites present. Despite the very low growth temperature, a homogenous phase of purely amorphous GaNBi could not be formed. Instead, there are GaN nanocrystallites embedded in an amorphous GaNBi matrix. Due to

the low energy absorption observed described in the next section, the optical absorption spectra still reflect the optical properties of the amorphous GaN<sub>1-x</sub>As<sub>x</sub> is shown in Fig 5.7(d) and (e); the broad diffraction rings and salt/pepper contrast indicative of a homogeneous amorphous phase is clear (Yu, 2010). It is interesting to note the difficulty of forming homogenous GaN<sub>1-x</sub>As<sub>x</sub> alloy system which is more readily grown. A recent investigation of the structure of the GaN<sub>1-x</sub>As<sub>x</sub> thin films using the TEM techniques of Z-contrast and electron energy loss spectroscopy has shown that there are small Bi-rich precipitates for samples with more than 6.5 at% Bi (Liliental-Weber, 2012). However, these precipitates are not connected, and there is still Bi in the amorphous matrix phase in lower concentration.

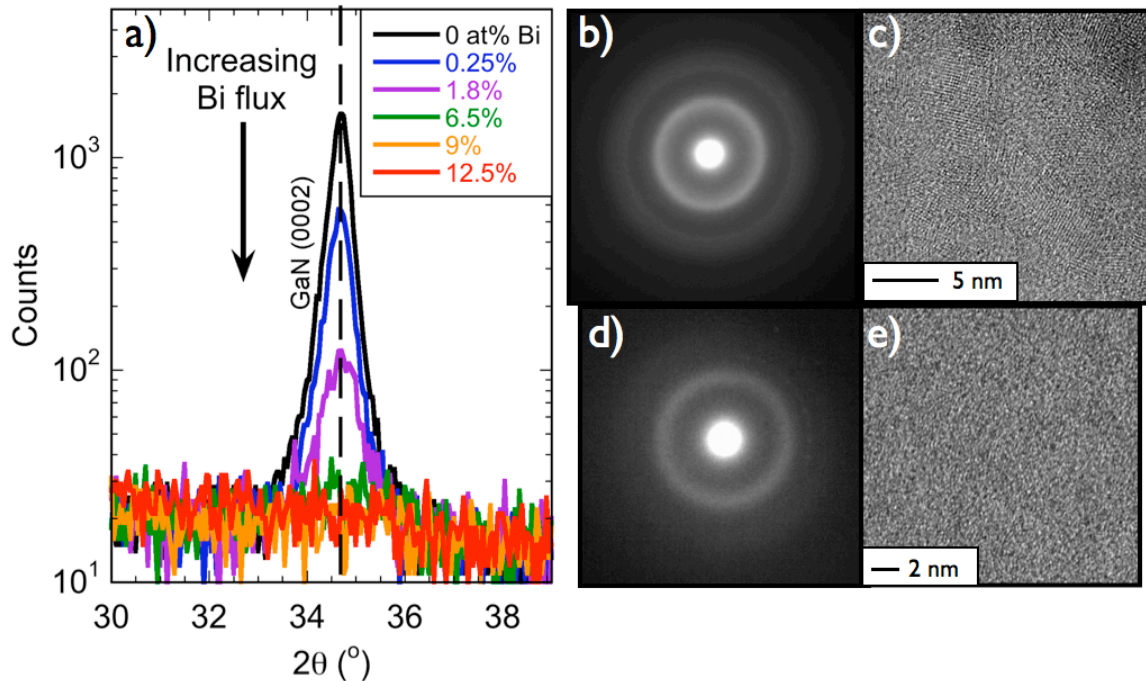


**Fig 5.7** (a) XRD patterns for different GaN<sub>1-x</sub>As<sub>x</sub> samples grown at low temperature, each with a different Bi flux and therefore Bi content. No incorporation of Bi into c-GaN was detected. At higher Bi contents the GaN (0002) peak was not visible. The (b) SAD pattern shows diffuse rings, but (c) HR-TEM imaging revealed nanocrystallites < 5 nm in diameter. For comparison, a (d) SAD and (e) HR-TEM image of amorphous GaN<sub>0.55</sub>As<sub>0.45</sub> grown on a glass substrate by LT-MBE is shown. Note the “salt/pepper” contrast of the HR-TEM image that is indicative of the amorphous phase.

## 5.2 Optical and electrical properties

As a first test of the chemical interaction between Bi and GaN, the optical absorption of the films was investigated. Fig 5.8 shows the effect of Bi content on the absorption characteristics of the material. A low-energy tail of relatively weak sub-band-

gap absorption is observed in GaN and the low at% Bi GaNBi (0.75 at%). The appearance of the Fabry-Perot oscillations indicates that the films are smooth and uniform, but they also limit the accuracy of the absorption measurement to absorption coefficients higher than  $\sim 10^4 \text{ cm}^{-1}$ . The absorption spectra in the samples with at% Bi  $\geq 2.5$  clearly show an onset of strong absorption ( $>10^4 \text{ cm}^{-1}$ ) at photon energies ranging from about 1.5 eV for 2.5 at% Bi to 1 eV for 5.5 at% Bi. Taking into account unavoidable absorption edge broadening effects of the order of 0.2 eV, the actual average absorption edge is located close to 1.2 eV for 5.5 at% Bi (Mayer, 2010).

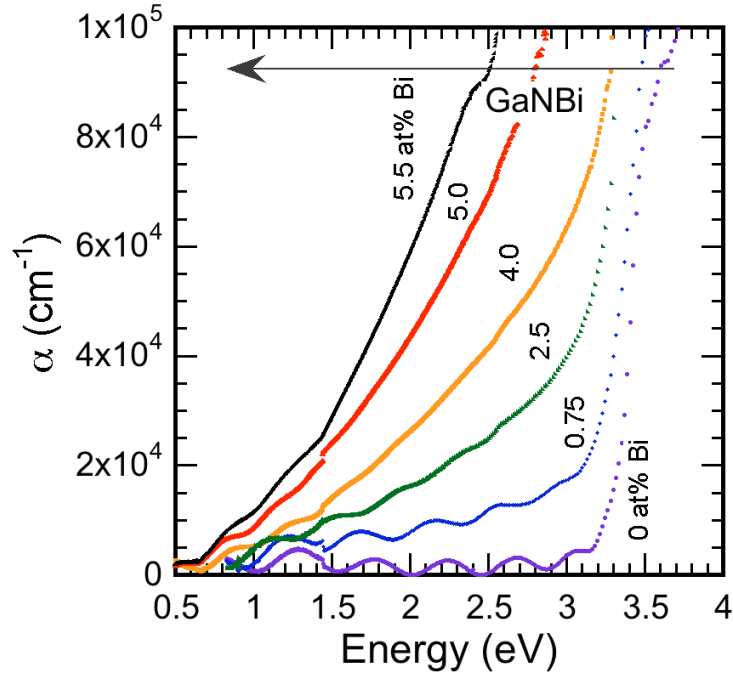


**Fig 5.8** The absorption spectra for GaNBi films grown at different growth temperatures. The composition of each film is given in the figure.

The observed optical absorption spectra can be qualitatively understood in terms of the band anticrossing (BAC) model of HMAs. Previous experiments have determined that the bismuth energy level ( $E_{Bi}$ ) is located 0.1 eV above the valence band edge of GaP (Trumbore, 1966). Applying the transitivity rule of semiconductor band offsets, we can predict that  $E_{Bi}$  will be near mid-gap in GaN at 1.7 eV above the valence band edge (Vurgaftman, 2003). Similar to the case of As in GaNAs or Se in ZnOSe, the localized Bi states form a narrow fully occupied band through the anticrossing interaction with the extended states of the valence band of GaN matrix (Wu, 2004; Mayer, 2010). Consequently the lowest energy optical transitions start at about 1.7 eV at low Bi contents. The absorption edge energy decreases with increasing Bi concentration due to two effects: a downward shift of the conduction band towards GaBi, and the widening of the Bi-derived midgap band. Following the arguments of Alberi *et al.*, the conduction band offset between GaN and GaBi amounts to about 2.3 eV. Therefore for GaNBi with 5.5 at% Bi, the conduction band edge and thus also the absorption edge shift, downward

by at least 0.25 eV. The remaining 0.25 eV part of the total shift of the absorption edge from the bismuth level energy,  $E_{Bi} = 1.7$  eV to about 1.2 eV can be attributed to the anticrossing-induced widening of the Bi-derived band. According to the band anticrossing model, the width of the Bi-derived band is equal to  $(\sqrt{E_{Bi}^2 + 4C^2x} - E_{Bi})/2$ . A coupling constant  $C = 2$  eV is required to account for the band widening of 0.25 eV. This value is quite reasonable compared with  $C = 1.6$  eV found in the significantly less mismatched  $\text{GaAs}_{1-x}\text{Bi}_x$  HMA (Alberi, 2007). This qualitative agreement between experiment and the BAC model confirms the previous findings in  $\text{GaN}_{1-x}\text{As}_x$  alloys that have shown applicability of the model to the analysis of the absorption edge of amorphous HMAs (Yu, 2010).

Fig 5.9 shows the optical absorption spectra for a GaN reference sample grown at low temperature ( $\sim 80^\circ\text{C}$ ) and a series of samples grown with similar Bi BEP but varying Ga BEP and therefore III:V ratio. Despite the films having very similar Bi concentrations of  $\sim 6.5$  at% Bi as determined from RBS, the optical absorption spectra are dramatically different. We found that the maximum shift in the absorption edge occurs when a III:V ratio in the film of unity is achieved. This suggests that when the RBS determined III:V ratio  $< 1$ , a homogeneous GaNBi alloy is not formed. For the growth of crystalline dilute  $\text{GaAs}_{1-x}\text{Bi}_x$ , As-rich conditions reduce the concentration of substitutional Bi (Oe, 1998; Yoshimoto, 2003; Henini, 2007). It is possible that this principle extends to the GaNBi alloys for which N-rich conditions lead to less incorporation of Bi into an alloy phase and therefore less optical absorption shift.

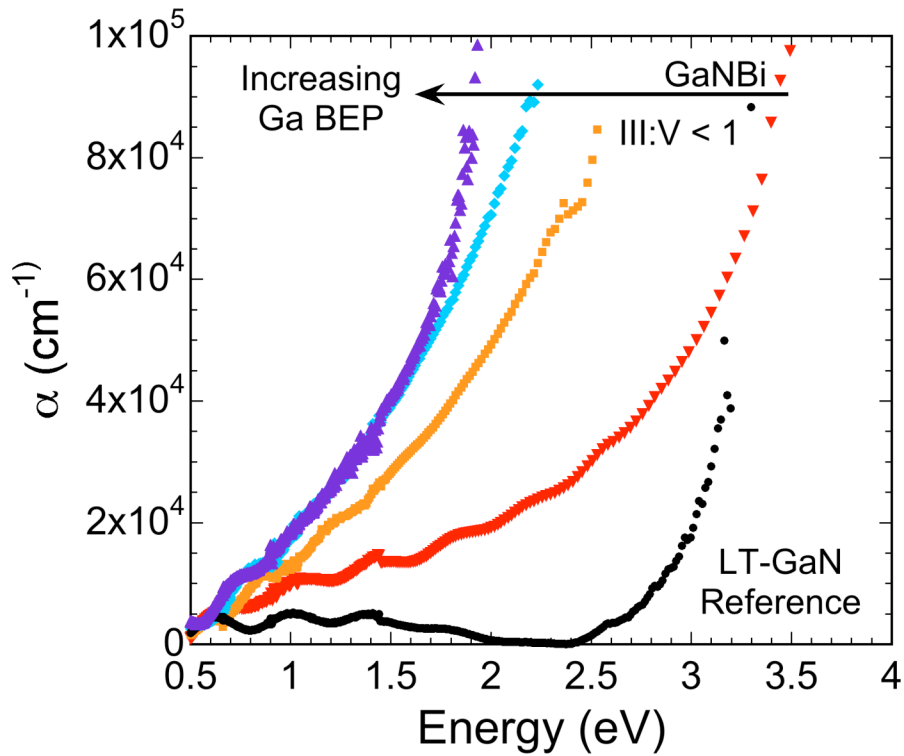


**Fig 5.9** Optical absorption spectra as a function of Ga BEP for a series of samples grown under similar Bi BEP and growth temperature. The circles represent the absorption

spectra for a LT-MBE grown GaN film. As the Ga BEP increases, the incorporation of Bi into GaNBi increases until a III:V ratio of unity is reached for the left most spectrum (triangles).

Unlike the undoped amorphous  $\text{GaN}_{1-x}\text{As}_x$  alloys that are highly insulating, as-grown unintentionally doped GaNBi alloys grown at low temperature (80-90°C) are conducting. The direct-current conductivity was measured using the four-point van der Pauw method and pressed indium contacts made after a brief HCl rinse to remove any surface oxide layer. The contacts were determined to be ohmic from the linear relationship between current and voltage. The temperature dependence of the conductivity was investigated using a liquid-helium cryostat. Thermopower (Seebeck coefficient) measurements were used to determine the majority carrier type instead of the Hall effect since it is the preferred method for characterizing carrier type in disordered systems (Mott, 1979). The thermopower was measured using a home-built setup with pressed indium contacts and a temperature gradient of 2°C produced by local heaters while the sample was inside a liquid nitrogen cryostat.

An examination of the electrical transport properties revealed an interesting trend as changing the Bi BEP varied the Bi content. The conductivity increased from  $\sim 4.0 \times 10^{-3}$  S/cm for pure LT-MBE grown GaN to  $\sim 144$  S/cm for GaNBi with 12.5 at% Bi. The temperature dependence of the conductivity,  $\sigma(T)$ , was found to decrease with increasing Bi content as shown in Fig 5.10. The  $\sigma(T)$  of the highest Bi content film behaves as a degenerately doped semiconductor with very little thermal activation at low temperatures. This result suggests that the increased conductivity is due to a higher concentration of free charge carriers.

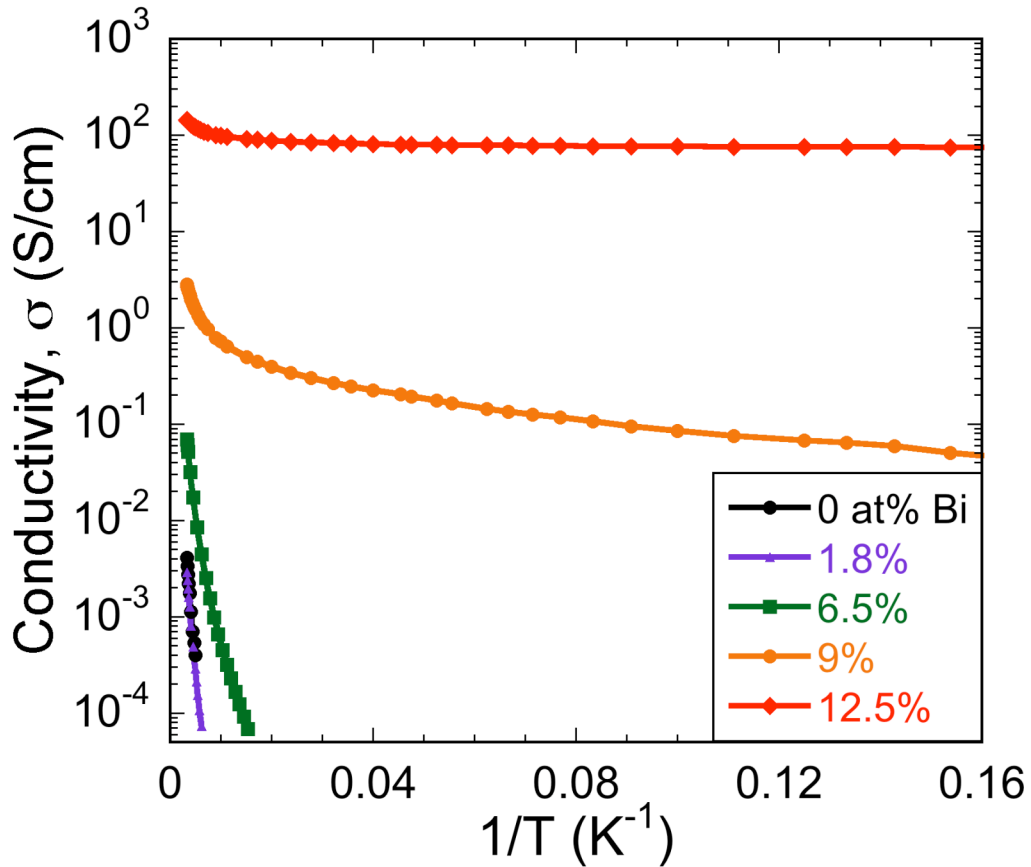


**Fig 5.10** Temperature dependence of the conductivity of GaNBi with varying Bi content. The room temperature conductivity increases and the conductivity temperature dependence decreases with increasing Bi content.

The thermopower as a function of temperature,  $S(T)$ , was used to determine the majority carrier type and the results are shown in Fig 5.11. The positive value clearly signifies the holes are the majority carriers, and the decreasing magnitude with increasing Bi content suggests an increasing hole concentration. Since bismuth metal has a negative thermopower near  $-55 \mu\text{V/K}$ , a connected network of metal clusters cannot be the cause of the conductivity or thermopower (Damodara Das, 1987). This is also consistent with TEM results, which showed that the Bi-rich clusters are isolated. The magnitude of  $\sim 10$ - $20 \mu\text{V/K}$  is typical for degenerately doped semiconductors, which agrees with the results of  $\sigma(T)$ .

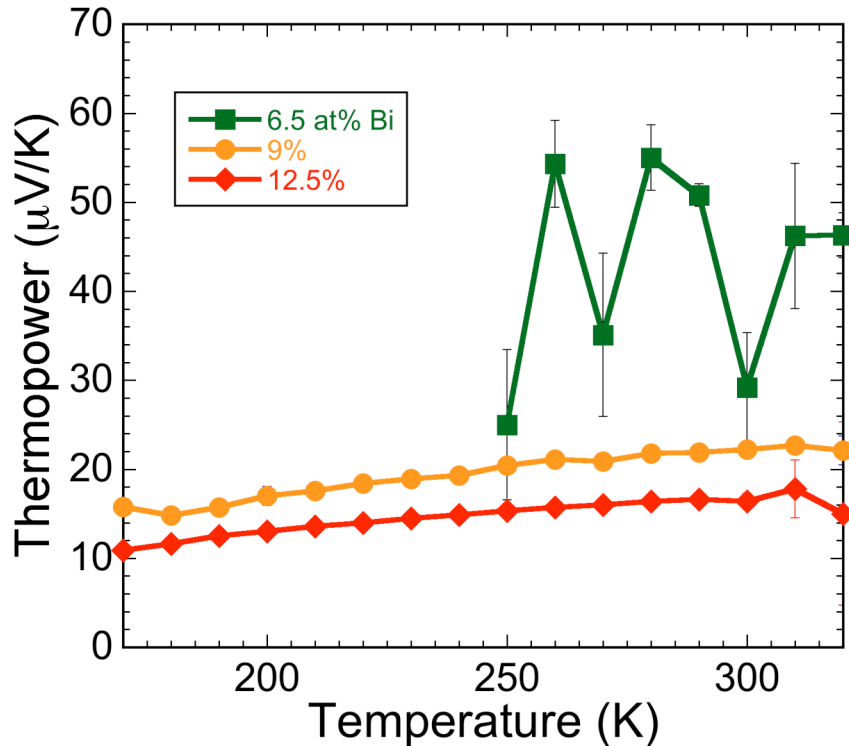


**Fig 5.11** Temperature dependence of the thermopower of GaNBi with varying Bi content. The positive value indicates holes are the majority carrier. The data for the sample with 6.5 at% Bi has more variation due to the higher resistance of the sample.

One lingering question of this work is the cause of high *p*-type conductivity for the GaNBi films with high Bi content. This is particularly interesting due to the tendency of GaN to be native *n*-type due to nitrogen vacancies and/or oxygen impurities (Van de Walle, 2004). One possible explanation is the movement of the valence band to higher energy due to a Bi-derived band at approximately mid-gap. The higher valence band edge energy would then affect defect formation energies and perhaps make acceptor defects more prevalent (Walukiewicz, 2001). However, this explanation needs to be quantitatively verified. The next section describes our work to investigate the movement of the band edges, which may play a role in modifying the conductivity.

The nitrogen partial density of states (DOS) of the valence band (VB) and conduction band (CB) can be determined using soft x-ray emission (SXE) and x-ray absorption (XAS) spectroscopies. In addition, overlapping and aligning the spectra with respect to core energy levels allows for the direct measurement of the absolute positions of the VB and CB edges. To investigate the effect of bismuth incorporation on the density of states of GaNBi, the nitrogen *K*-edge (near 400 eV) was examined at the Advanced Light Source on beam line 8.0.1. The SXE was measured using a Tennessee/Tulane grating spectrometer with an energy resolution of ~0.6 eV; the XAS was measured in total fluorescence yield detection mode with an energy resolution of ~0.2 eV.

The nitrogen partial density of states of III:V stoichiometric GaNBi films without oxygen grown at different temperatures was examined using SXE and XAS to probe the valence and conduction bands, respectively (Duda, 1998). Hybridization of 2*p* nitrogen

states with Bi states via Ga atoms would result in a modification of the nitrogen partial density of states and provides further evidence for the formation of a GaN<sub>2</sub>Bi related phase as opposed to chemically separate GaN and Bi phases. The SXE and 45° incident XAS spectra of the nitrogen *K*-edge are shown in Fig 5.12 & Fig 5.13. For the XAS spectra, the pre-edge linear background was subtracted and the absorption step edge was normalized to unity at 430 eV. In the SXE spectra, the elastic emission peak near 398.5 eV was used to calibrate the detector energy to the monochromator energy of the XAS spectra, which allows both to be plotted together and the absolute positions of the band edges to be determined.

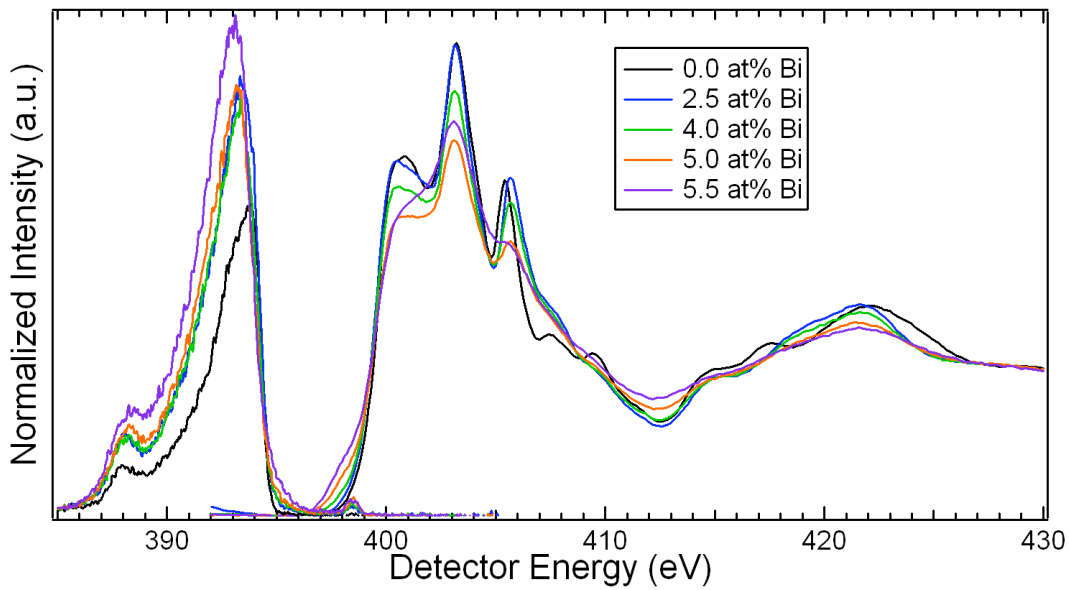


**Fig 5.12** The nitrogen *K*-edge SXE (left side) and total fluorescence yield XAS (right side) of GaNBi films with various Bi contents. The threshold-excited elastic emission peak near 398.5 eV was used to align the SXE spectra to the XAS.

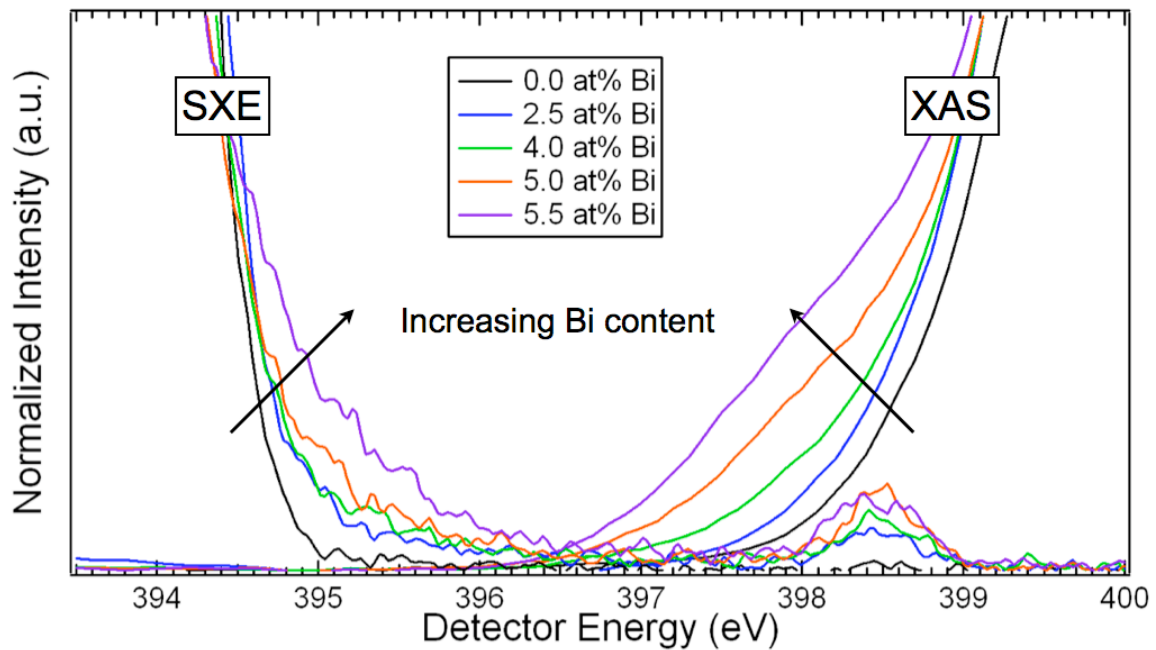


**Fig 5.13** Magnified view of the SXE and XAS of GaNBi with various Bi contents highlighting the changes to the band edge positions.

In the wide view of the spectra shown in Fig 5.12, the overall features of the SXE and XAS spectra can be observed. In a homogenous amorphous system, the sharp features of the XAS spectra should be broadened due to the lack of long-range periodicity as was reported for a-GaN<sub>1-x</sub>As<sub>x</sub> in Yu, 2010. The presence of peaks in the XAS spectra for GaN<sub>1-x</sub>Bi<sub>x</sub> films of various compositions suggests that a significant fraction of nitrogen in the film is in the form of crystalline GaN. However, the peaks tend to broaden and begin to wash out as the Bi content increases from 0 at% to 5.5 at%. Examining the XAS at different incident angles (10°, 45°, and 75°) suggests that intermediate Bi concentrations show increasing orientational disorder. For higher Bi concentrations the loss of some anisotropy suggests decreasing long-range order and/or an increasing fraction of amorphous phase. This is consistent with the TEM observations described earlier (Liliental-Weber, 2012).

The increasing overall SXE valence band emission and peak shift to lower energy for greater Bi content in Fig 5.12 is a reflection of the loss of threshold-excited *k*-selectivity due to the presence of in-gap states and/or loss of crystallinity (but not due to loss of orientational order in a polycrystalline phase) (Strocov, 1995). For crystalline GaN (and randomly ordered polycrystalline GaN), nitrogen *K*-edge threshold excitation occurs at the conduction band minimum at the  $\Gamma$ -point and hence restricts the possible valence band emission also from only the same  $\Gamma$ -point due to the lack of intermediate state scattering paths the excited electron to other *k*-points (Strocov, 1995). The emission *k*-selectivity suppresses the overall intensity of the SXE spectra relative to above-threshold excitation and a relative intensity shift towards higher energy is indicative of the direct gap location of the VB maximum. With the introduction of (*k*-independent) localized gap states and a decrease of long-range order, the special  $\Gamma$ -point selectivity for threshold x-ray excitation is destroyed and the valence band x-ray emission for *k*-points throughout the Brillouin zone (BZ) is allowed. The result is the overall intensity increase and lineshape shift back to lower energy more reflective of the full BZ-averaged nitrogen partial density of states. Due to the *k*-selectivity effect, the relative experimental intensities of the 398.5 eV excited SXE spectra in Fig 5.12 were preserved and not individually normalized to the same maximum value.

Taking a close look at the band gap region of the SXE and XAS spectra in Fig 5.13, the effect of Bi on the band edge positions can be determined. There is a dramatic difference in the behavior of the valence band edge (VBE) and the conduction band edge (CBE) with increasing Bi content. At 2.5 at% Bi, a weak high-energy foot is observed in the SXE. The VBE jumps from ~395 eV to ~396.5 eV which is approximately mid-gap of GaN whereas the CBE only moves slightly to lower energy by ~0.2 eV. As the Bi content increases to 5.5 at%, the VBE remains in a similar position but the amplitude of the SXE increases indicating increased hybridization between N and Bi. The CBE gradually shifts to lower energy as the Bi content increases until the gap region is almost eliminated. The appearance of a near zero gap could be due to simultaneous x-ray absorption and emission from a partially occupied Bi-derived band near the mid-gap energy position of GaN.

The abrupt movement of the VBE to mid-gap agrees qualitatively with the expected location of the Bi impurity level and the BAC model. According to the BAC model, upon isoelectronic substitution of an anion with a metal-like highly mismatched

element, the impurity states hybridize with the valence band causing an abrupt shift of the VBE to higher energy (Walukiewicz, 2008). This effect has been extensively studied in the  $\text{GaN}_{1-x}\text{As}_x$  system in which the band gap is dramatically reduced from 3.4 eV to 2.6 eV for  $x \sim 0.01$  due to the movement of the valence band (Wu, 2004). This effect has also been studied in the dilute  $\text{GaAs}_{1-x}\text{Bi}_x$  alloys (Alberi, 2007).

The efficient  $p$ -type doping of GaNBi alloys can be understood in terms of the amphoteric defect model, which relates the  $p$ -type dopability to the location of the valence band relative to the Fermi level stabilization energy,  $E_{FS}$  — an energy reference common to all semiconductors and located at about 4.9 eV below the vacuum level (Morkoç, 1994; Walukiewicz, 2001). GaN is difficult to dope  $p$ -type because the valence band lies as low as 2.8 eV below  $E_{FS}$ . As mentioned above, the partial replacement of N with Bi leads to a rapid upward shift of the valence band edge in the resulting GaNBi alloy. Thus the valence band edge in GaNBi is located only about 1.3 eV below  $E_{FS}$ , making this material easier to be doped  $p$ -type. The large shift of the valence band edge to higher energy would greatly reduce the formation energy of acceptor-like native defects and may be responsible for the  $p$ -type conductivity observed.

## 6 Conclusions and Outlook

Highly mismatched semiconductor alloys are difficult to synthesize due to the miscibility gap caused by differences in electronegativity and atomic radius. However, by applying the technique of low-temperature molecular beam epitaxy, the HMA  $\text{GaN}_{1-x}\text{As}_x$  has been successfully grown across the composition range. The low-temperature of film growth reduces the surface and bulk diffusivity of deposited atoms, preventing them from adopting lower energy sites in segregated crystalline phases. The intermediate composition alloys are amorphous but still exhibit systematic shifts in their band gap and band edges. The amorphous alloys exhibit remarkable stability against high temperature perturbations, remaining amorphous for long-term furnace anneals at  $600^\circ\text{C}$  despite phase segregating during growth if at substrate temperatures above  $400^\circ\text{C}$ . In addition, the amorphous alloys resist phase segregation for rapid thermal anneals above  $700^\circ\text{C}$ . Ultra-fast annealing of intermediate-composition, amorphous  $\text{GaN}_{1-x}\text{As}_x$  with a pulsed laser allows for the incorporation of up to 8 at% N into GaAs, which is similar to the most nitrogen incorporated into GaAs during optimized molecular beam epitaxy growth.

The amorphous  $\text{GaN}_{1-x}\text{As}_x$  alloys are a promising candidate material system for thin film electronics due to their large absorption coefficient and band gap tunability. Their amorphous structure allows them to be deposited on inexpensive glass substrates or even potentially plastic substrates. Despite these positive aspects, there are significant challenges to the technical application of amorphous  $\text{GaN}_{1-x}\text{As}_x$ . Control over the electronic properties remains a pressing concern. A large swath of growth parameter space was investigated by varying the growth temperature, As BEP, and Ga BEP. No homogeneously amorphous conducting films were successfully grown. Indeed, as the Ga BEP was reduced, the crystallinity and conductivity decreased until an amorphous but semi-insulating, film was grown.

The conclusion from local structure analysis was a high concentration of dangling bonds. These dangling bonds are most likely inhibiting the attempts to control the electronic properties of the material. An investigation into how hydrogen interacts with the material would be useful to establish whether or not hydrogen will combine with the dangling bonds. The passivation of dangling bonds in amorphous silicon by hydrogen was a key step in the development of amorphous silicon technology and may be useful for the successful application of amorphous III-V semiconductor alloys as well.

Despite the success of the low-temperature molecular beam epitaxy technique to synthesizing homogenous  $\text{GaN}_{1-x}\text{As}_x$ , the technique cannot overcome the miscibility gap in all systems. When LT-MBE is extended to the extremely mismatched  $\text{GaN}_{1-x}\text{Bi}_x$  system, the formation of homogeneous material is not guaranteed. Despite the lack of homogeneity and presence of segregated GaN crystallites, there are monotonic changes in optical and electrical properties with changes in bismuth content, which can be qualitatively explained by invoking the BAC model. At high bismuth contents, the resulting films become highly conducting and *p*-type despite bismuth metal and low quality GaN generally being *n*-type. For the better matched  $\text{GaN}_{1-x}\text{Sb}_x$  material system, there are promising results that homogeneous amorphous alloys can be grown.

## 7 Appendix

### 7.1 Effects of point defects on thermal and thermoelectric properties of InN

The study of group III-nitrides is motivated by the wide bandgap range of their alloys from the ultra-violet to the infrared ( $E_{g,\text{AlN}} = 6.1$  eV,  $E_{g,\text{GaN}} = 3.4$  eV,  $E_{g,\text{InN}} = 0.64$  eV), allowing for applications in a wide range of devices from optoelectronics to photovoltaics (Wu, 2009). Since the discovery of the narrow bandgap of InN from high-quality films in 2002, there has been vigorous research in the optoelectronic properties of InN and In-rich  $\text{In}_{1-x}\text{Ga}_x\text{N}$  alloys (Wu, 2002; Veal, 2010). Measurements of the Seebeck coefficient of *p*-type InN have been used to determine hole concentrations by circumventing issues of surface Fermi level pinning in the conduction band (Miller, 2010). High-energy particle irradiation has been used to study the effects of point defects on the electrical and optoelectronic properties (e.g. carrier mobility, photoluminescence) of In-rich alloys (Yu, 2009b).

However, despite this vast progress, thermal properties of high-quality InN have not been investigated. The thermal conductivity of a material has become an increasingly important issue in the thermal management of high power and/or miniaturized devices. The cation/anion mass ratio of InN is the highest among all group III-V materials, which directly causes a wide phonon bandgap and narrow acoustic phonon band in InN (Wu, 2009). This high In/N mass ratio also implies a high sensitivity of its thermal conductivity to In-related point defects (Klemens, 1960). The thermal and thermoelectric properties of InN and the effect of irradiation-introduced native point defects on these properties have been examined.

The single-crystal InN films examined in this study were grown by molecular-beam epitaxy on *c*-sapphire substrates with a GaN buffer layer (Lu, 2000). The 500-2100 nm thick InN layers were not intentionally doped. They have background electron concentrations between  $8 \times 10^{17} \text{ cm}^{-3}$  and  $3 \times 10^{18} \text{ cm}^{-3}$ , and mobility between 1500 and  $1045 \text{ cm}^2/\text{Vs}$ . Their high mobility and a strong photoluminescence peak at  $\sim 0.7\text{eV}$  indicate high crystal quality and low impurity levels in these films. The exact film thicknesses were determined by Rutherford backscattering spectrometry with a 2.13 MeV  $\text{He}^{2+}$  beam. The irradiation was performed using a 2.13 MeV  $\text{He}^{2+}$  beam with a current between 40-150 nA generated by a Pelletron tandem accelerator. The ion beam was defocused to an area of  $40 \text{ mm}^2$  to cover the entire sample with doses ranging between  $6.5 \times 10^{13}$  and  $1 \times 10^{16} \text{ He}^{2+}/\text{cm}^2$ . Simulations using SRIM (the Stopping and Range of Ions in Matter) software predicted that the concentration of defects generated by the ion beam is relatively uniform (Fig 7.1 inset), and the ions would penetrate the entire thickness of the InN film, leaving end of range damage in the sapphire substrate.

Out-of-plane thermal conductivity measurements were conducted at room temperature using time-domain thermoreflectance (TDTR) (Paddock, 1986). Details of the measurement setup are described in Cahill, 2003. The modulation frequency of the pump beam was fixed at 10 MHz. The radii of the pump and probe beams were  $15 \mu\text{m}$  at the sample surface and the total laser power of 30 mW caused a  $< 5$  K temperature increase. The samples were prepared for TDTR by coating the films with a  $\sim 100$  nm

thick magnetron sputtered Al film. Data analysis procedures are described in Cahill, 2004.

The thermal conductivity of the as grown and irradiated films is plotted in Fig 7.1. The pristine InN thermal conductivity was determined to be 120 W/m·K along the c-axis direction, more than twice the previously reported 45 W/m·K for InN grown by nitrogen microwave plasma chemical vapor deposition (Krukowski, 1998). Our measured value is in better agreement with the theoretical lattice thermal conductivity of InN of ~180 W/m·K at room temperature, calculated using  $\kappa_{\text{theoretical}} = C_v l v / 3$ , where  $C_v$  is the molar specific heat,  $v$  is the Debye-averaged acoustic phonon velocity along the c-axis, and  $l = a / (\alpha_v \gamma T)$  is the phonon mean free path. The interatomic spacing  $a$  is half the c lattice parameter,  $\alpha_v$  is the volume thermal expansion coefficient, and  $\gamma$  is the Grüneisen parameter (Berman, 1976; Zubrilov, 2001; Williams, 1998). The thermal conductivity measured from high-quality films is expected to be closer to the theoretically predicted value and the measurements confirm this prediction.

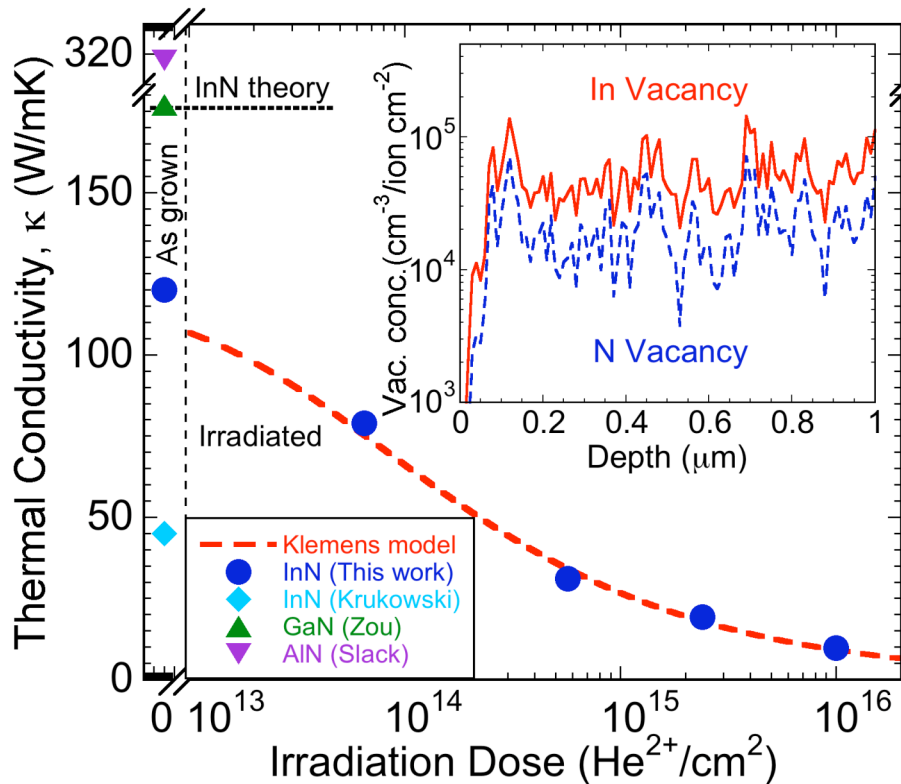


**Fig 7.1** Thermal conductivity of InN as a function of  $\text{He}^{2+}$  irradiation dose compared to theoretical prediction from Eq.(1). A fitting parameter of  $\beta=0.13$  was used to correlate the SRIM-predicted indium point defect concentration and the actual phonon-scattering defect concentration. Previously reported thermal conductivities of GaN, AlN and InN are included as a reference. Inset is SRIM calculated In and N vacancy concentration as a function of depth.

The thermal conductivity is rapidly reduced by irradiation and the behavior can be explained using the Klemens model for point defect thermal resistance (Klemens, 1960). For point defect dominated phonon scattering, the thermal conductivity is dependent on the concentration of point defects that create a mass difference at the lattice sites. This is described by a point defect scattering relaxation time,  $\tau = 1/A\omega^4$ , where  $\omega$  is the phonon frequency. The parameter  $A$  depends on the dominant type of defects, which for this study are point defects generated by displacement of atoms due to the impinging  $\text{He}^{2+}$  ions. For point defects,  $A$  is given by  $C_{vac}\Omega(3\Delta M/M)^2/4\pi v^3$ , where  $C_{vac}$  is the defect concentration per unit cell,  $\Omega$  is the unit cell volume, and  $\Delta M/M$  is the relative change in mass for one defect per unit cell. Although defect clusters can form through various defect reactions, their overall contribution to the thermal conductivity reduction is expected to be minimal due to their low concentration at the irradiation doses considered [15, (White, 1993).

The general form of thermal conductivity at  $k_B T > \hbar\omega_D/3$  is approximated as [6]

$$\kappa(\omega_0) = \kappa_0 \frac{\omega_0}{\omega_D} \arctan\left(\frac{\omega_D}{\omega_0}\right) \quad (1)$$

where  $\kappa_0$  is the pristine lattice thermal conductivity and  $\hbar\omega_D/k_B = 660\text{K}$  is the Debye temperature (Wu, 2009).  $\omega_0 \propto 1/\sqrt{A}$  and represents the frequency where the Umklapp scattering and point defect scattering rates are equal. Both vacancy and interstitial point defects are formed during irradiation, which have the same  $\Delta M/M$ . Due to the small  $\Delta M$  for nitrogen vacancies/interstitials and their lower concentration predicted by SRIM (Fig 7.1 inset), indium vacancies and interstitials are considered the dominant cause of the thermal conductivity reduction.

A single fitting parameter,  $\beta$ , was used to determine the relation between the theoretically predicted number of point defects using the Monte Carlo method of SRIM and the concentration of defects required to account for the thermal conductivity reduction ( $C_{vac-experimental} = \beta C_{vac-SRIM}$ ). The model fit shown in Fig 7.1 was achieved using  $\beta=0.13$ . The non-unity value of  $\beta$  can be caused by vacancy-interstitial annihilation that can occur both during and after irradiation, and other effects from defect clusters not explicitly considered (Williams, 1998). SRIM only models a simple cumulative process that does not account for energetic bombardment that displaces an atom back to its original lattice position (dynamic annealing). A dynamical Monte Carlo simulation would be needed for a more quantitative explanation of the nonunity value of  $\beta$ .

In Fig 7.1 the thermal conductivity of InN is also compared to those of other group III-nitrides, GaN (177 W/m·K) and AlN (319 W/m·K) (Zou, 2002; Slack, 1987). As expected, due to the heavier mass of the indium atom, and therefore lower sound velocity of InN, the thermal conductivity of InN is the lowest of the three. We note that even at the highest electrical conductivity ( $\sigma \sim 3200/\Omega\text{cm}$ ), the electronic thermal conductivity is still much lower than the lattice thermal conductivity (estimated to be 1.7 W/m·K from the Wiedemann-Franz Law).

The electron concentration ( $n$ ) and mobility ( $\mu$ ) of the InN films as characterized by Hall effect are shown in Fig 7.2. As reported previously, the electron concentration of InN increases with native defect concentration due to its low-lying conduction band edge which makes native defects donor-like (Walukiewicz, 2003). The electron generation rate

( $R_e$ ) for  $\text{He}^{2+}$  ions was determined to be  $\sim 3500 \text{ cm}^{-1}$  based on a linear correlation between electron concentration and irradiation dose ( $n = R_e \times \Phi$ ), which agrees well with previous reports of  $\text{He}^+$  irradiation (Jones, 2006). As expected, the mobility decreases with irradiation due to carrier scattering from these charged defects.

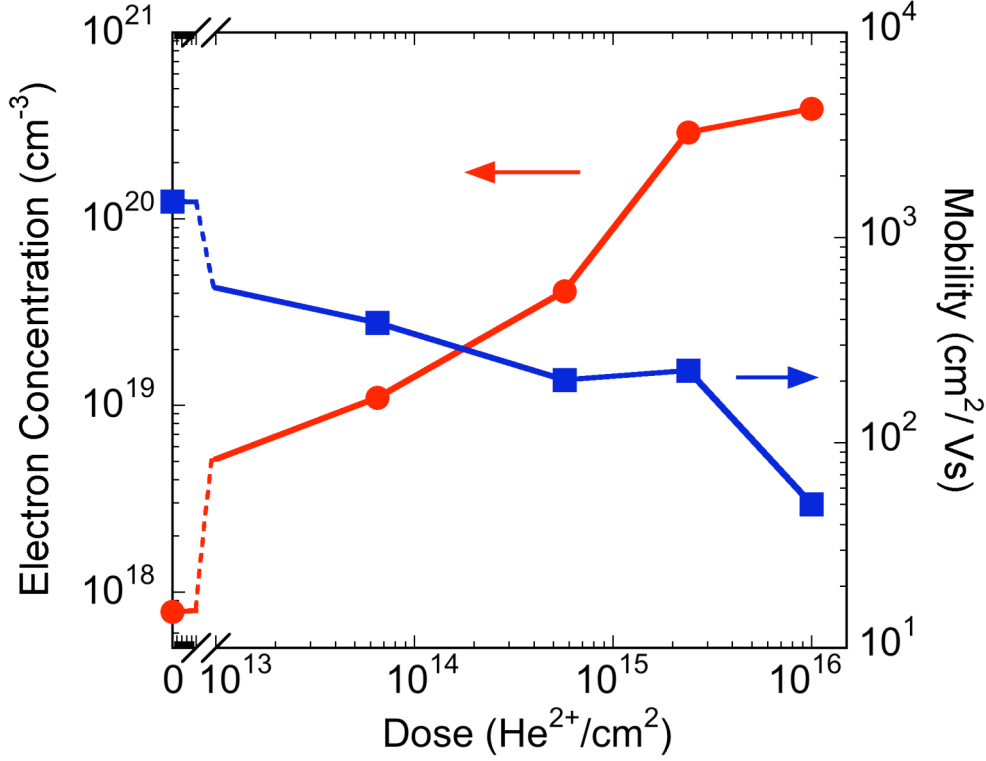


**Fig 7.2** Free electron concentration and mobility of InN as a function of  $\text{He}^{2+}$  irradiation dose.

The Seebeck coefficient is plotted as a function of electron concentration in Fig 7.3. In the degenerate doping limit, the Seebeck coefficient can be expressed as (Seeger, 2002).

$$S_{\text{Degenerate}} = -\frac{k_B}{e} (r + 3/2) \frac{\pi^2}{3} \frac{k_B T}{\zeta} \quad (2)$$

where  $\zeta$  is the Fermi energy and  $r$  is the power law index relating the relaxation time to energy for free charge carriers ( $\tau \propto \epsilon^r$ ). The non-parabolicity of the InN conduction band was taken into account in calculating the electron density dependence of  $\zeta$  (Wu, 2009). The model agrees reasonably well with the experimental data at electron concentrations greater than  $\sim 10^{19} \text{ cm}^{-3}$  for which the degenerate approximation applies. At low electron concentrations, the experimental data deviate from Eq.(2) due to breakdown of the degenerate doping approximation and a relatively larger contribution from electrons in the surface accumulation layer (Yim, 2007). The Seebeck coefficient was calculated using an  $r$  value of  $-1/2$  or  $+1$ , which correspond to electron scattering dominated by phonons or ionized impurities, respectively. The dependence of the Seebeck coefficient

on irradiation-generated electrons is similar to previous studies of as grown InN with variable electron concentrations (Miller, 2009).

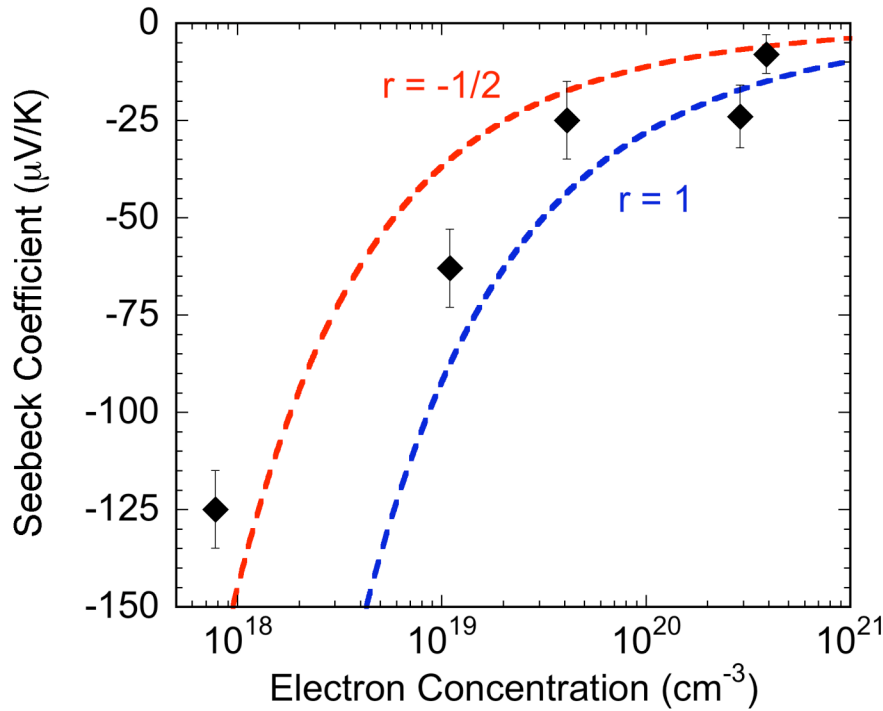


**Fig 7.3** Seebeck coefficient of irradiated InN as a function of free electron concentration. The dashed lines are calculated from a non-parabolic band model of the Seebeck coefficient in the degenerate doping approximation with different  $r$  values.

The three thermoelectric parameters were used to calculate the thermoelectric figure of merit,  $ZT = S^2\sigma/\kappa$ , as a function of irradiation dose. The  $ZT$  of pristine sample was 0.007 and stayed within 30% of this value after the irradiation doses considered. The  $ZT$  of most materials typically decreases with irradiation due to a greatly reduced electrical conductivity (Theilig, 1996). InN is unique in that irradiation results in an increase in electrical conductivity in addition to the greatly reduced thermal conductivity. These positive contributions to  $ZT$  are not completely canceled by the lower Seebeck coefficient. This result suggests that in addition to being a radiation-resistant photovoltaic material (Wu, 2009), the thermoelectric properties of InN are also radiation-resistant.

In summary, high energy ion irradiation to be a viable method for controlling the thermal, electrical, and thermoelectric properties of InN by introducing point defects. The thermal conductivity of high-quality InN was determined to be 120 W/m·K and the effects of point defects introduced by He<sup>2+</sup> irradiation were examined. The Seebeck coefficient of the irradiated films agreed with the theoretically predicted values based on carrier concentration and effective mass. The thermoelectric figure of merit of InN was found to be insensitive to irradiation.

## 7.2 Mathematica calculations for thermal conductivity modeling

---

### Modeling Effect of Native Defects on InN Thermal Conductivity

Alejandro Levander - 9/14/2010

#### ■ Setting up constants and parameters for InN

```
(*Constants*)
m0c2 = 0.51 * 106; (*m0*c2 in units of eV, m0 is electron mass in vacuum*)
hbarc = 1973; (*hbar*c in units of eV*Angstrom*)
kB = 1.3806504 * 10-23; (*Boltzmann constant in J/K*)
h = 6.62606896 * 10-34; (*Planks constant in J*s *)
c = 299 792 458; (*speed of light m/s*)
hbar = h / (2  $\pi$ );
cm = 10-2;
nm = 10-9;

(*InN Parameters*)
 $\kappa_0$  = 120; (*intrinsic thermal conductivity assuming no
defects from as grown thermal conductivity measurement W/mK*)
 $v$  = ( 12102 5170 )1/3; (* phonon speed in InN from Ioffe (m/s)*)
 $\Theta_D$  = 660; (*Debye temperature in (K) from J. Wu review *)
LatticeA = 0.3533; (*a lattice parameter from J. Wu review (nm)*)
LatticeC = 0.5693; (*c lattice parameter from J. Wu review (nm)*)
 $\Omega$  = LatticeA2 LatticeC Sin[60 Degree] nm3; (*Unit cell volume in m3*)
 $\omega_D$  = kB  $\Theta_D$  / hbar; (*Debye frequency*)
 $\rho$  = 6.81; (*InN density in g/cm3 from J. Wu review*)
Inmass = 114.818 * 6.02 10-23; (*mass of a In atom*)
Nmass = 14.0067 * 6.02 10-23;
UCmass = 2 Inmass + 2 Nmass; (*mass of unit cell in g*)
InVac = 4.78 104; (*SRIM calculated vacancy concentration per dose in vac/cm3*)
```

■ **Modeling Thermal Conductivity**

$$\Delta M = UC_{\text{mass}} - In_{\text{mass}};$$

$$Cv[\beta, Dose] := 2 In_{\text{Vac}} \beta Dose \text{ cm}^{-3} \Omega;$$

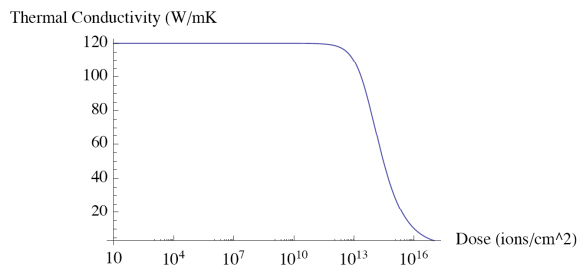
$$A[\beta, Dose] := Cv[\beta, Dose] \Omega \left( \frac{3 \Delta M}{UC_{\text{mass}}} \right)^2 \left( \frac{1}{4 \pi \nu^3} \right);$$

$$B = \frac{k_B \omega D}{2 \pi^2 \nu \kappa_0};$$

$$\omega_0[\beta, Dose] := \sqrt{\frac{B}{A[\beta, Dose]}};$$

$$\kappa[\beta, Dose] := \frac{\kappa_0 \omega_0[\beta, Dose]}{\omega D} \text{ArcTan}\left[\frac{\omega D}{\omega_0[\beta, Dose]}\right];$$

```
LogLinearPlot[\kappa[10-1, Dose], {Dose, 101, 1017},
  AxesLabel -> {"Dose (ions/cm2)", "Thermal Conductivity (W/mK)", PlotRange -> All]
```



■ **Compare to experimental values**

```
SetDirectory["/Users/Alejandro/Documents/Graduate School/Projects/InN Thermal Conductivity/Thermal Conductivity"];
```

(\*Read experimental data from file as  $\kappa$  vs. Dose\*)

```
dataxy = ReadList["InN-kappa.txt", {Number, Number}];
```

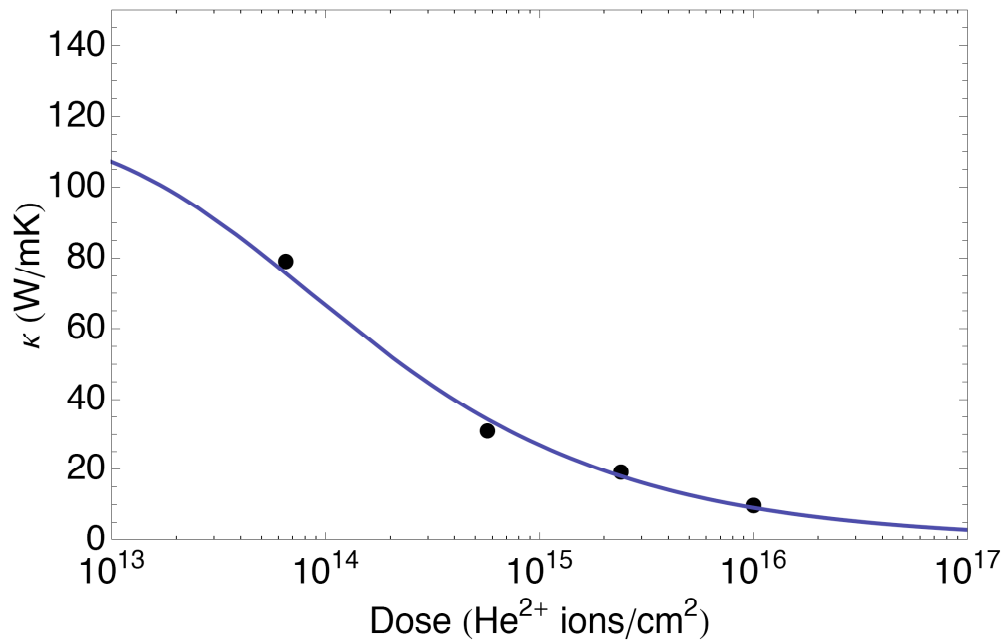
```
xdata = dataxy[[All, 1]]; (*array of x data, Dose*)
```

```
ydata = dataxy[[All, 2]]; (*array of y data,  $\kappa$  *)
```

```

fitplot = LogLinearPlot[κ[.13, Dose], {Dose, 100, 1018},
  AxesLabel → {"Dose (ions/cm2)", "Thermal Conductivity (W/mK)"},
  PlotRange → {{1013, 1017}, {0, 150}}, PlotStyle → {Thick}];
dataplot = ListLogLinearPlot[dataxy, AxesLabel → {"Dose (ions/cm2)", "κ (W/mK)"},
  DisplayFunction → Identity, PlotStyle → {PointSize[.018], Black},
  PlotRange -> {{1013, 1017}, {0, 150}}];
Show[dataplot, fitplot, Frame → True,
  FrameLabel → {"Dose (He2+ ions/cm2)", "κ (W/mK)"},
  LabelStyle → Directive[FontFamily → "Helvetica", 18], AxesLabel → True]

```



### 7.3 Junction thermoelectrics: silicon-nickel superlattice

Enhancing the Seebeck coefficient through the engineering of thermoelectric materials is essential to obtain higher values of  $zT$  in advanced thermoelectrics. In order to maximize the Seebeck coefficient, the asymmetry of the differential conductivity about the Fermi energy must be maximized (Vashaee, 2004). One method to induce this asymmetry is the insert energy barriers in the path of the charge carriers. The hot electrons can pass over the barrier, leaving the cold electrons behind, increasing the asymmetry of the differential conductivity. This essentially combines the physics of thermoelectrics and thermionics (Mahan, 1998). Fig 7.4 shows a schematic of the energy filtering technique applied to an  $n$ -type semiconductor in a thermoelectric cooling situation. The applied negative bias repels electrons and the hot electrons pass through the energy filter. The heat from the hot electrons is then rejected on the other side. An energy band diagram on the left side of Fig 7.5 shows the process of electron energy filtering in more detail. The principal of energy filtering of electrons has been used to explain Seebeck coefficient enhancements in nanostructured bulk PbTe thermoelectrics (Martin, 2009) and advanced III-V InGaAs/InGaAlAs:ErAs superlattices (Zeng, 2007).

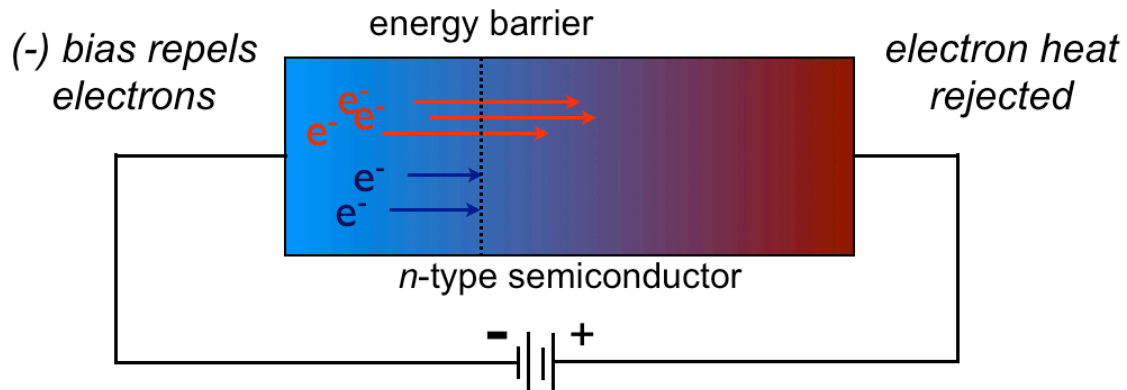


**Fig 7.4** Schematic of electron energy filtering in  $n$ -type semiconductor.

The degree to which the charge carrier is scattered by the interface at the energy-filtering junction has been theoretically predicted to affect the efficiency of energy filtering (Vashaee, 2004). If the carrier is not scattered by the junction, the carrier must have sufficient momentum in the direction perpendicular to the interface, in this case, the  $z$ -direction. In this situation, lateral momentum is conserved and energy filtering is less efficient. If however, through engineering of the junction interface, the charge carrier is scattered, then only the total carrier momentum must be greater than the barrier height. This situation describes a non-conservation of lateral momentum and the energy filtering is more efficient. The  $k$ -space diagram on the right side of Fig 7.5 describes these two situations. If lateral momentum is non-conserved, all carriers that fall within the red region can pass through the filter, however if lateral momentum is conserved, only carriers to the right of the dashed line in the red region can pass through the barrier.

Despite having sufficient total energy, a large portion of carriers are reflected at the barrier leading to less efficient energy filtering.

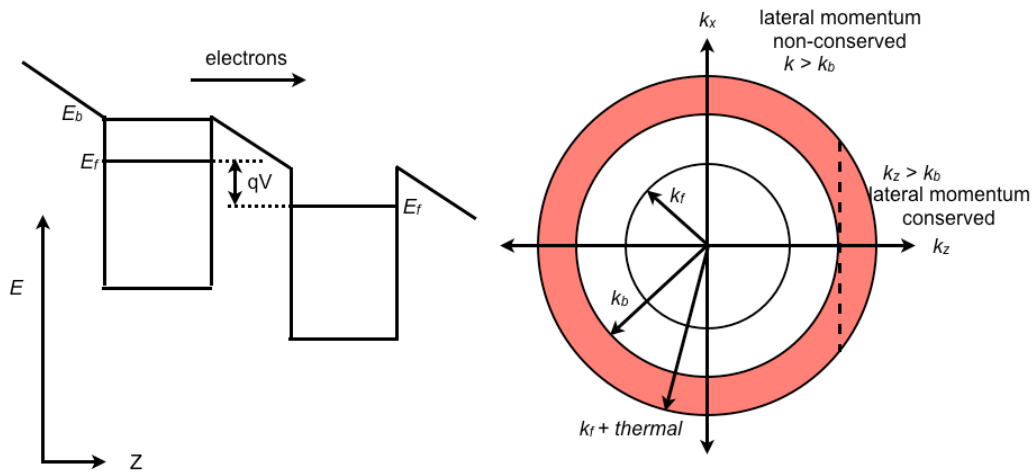


**Fig 7.5** Energy diagram for electron energy filtering superlattice (left).  $k$ -space diagram showing various key energies in  $k$ -space and the concept of lateral momentum conservation (right).

The Si/Ni interface has been proposed as a test system for electron energy filtering thermoelectrics due to the significant amount of microfabrication methods and techniques developed to process silicon. The barrier height at the n-Si/Ni interface is approximately 0.65 eV (Ottaviani, 1981). This is significantly larger than the ideal barrier height of  $3-5 k_b T$  where  $T$  is the operating temperature of the thermoelectric (Vashaee, 2004). However, the Si/Ni system can still be used as a material system for demonstrating and understanding the physics of electron energy filtering.

The Si/Ni test structure was fabricated using a silicon-on-insulator substrate template and microfabrication techniques. A schematic of the overall device is shown in the top of Fig 7.6. Photolithography was used to pattern stripes across the Si device layer. These exposed Si stripes were then etched using isotropic reactive ion etching in a  $SF_6 + O_2$  plasma. The silicon was etched down to the buried oxide layer, removing any potential for electrical conduction across the device layer. The vacant stripes were then filled with nickel by sputtering metal deposition. An SEM image of nickel filled trench is shown in the bottom of Fig 7.6.

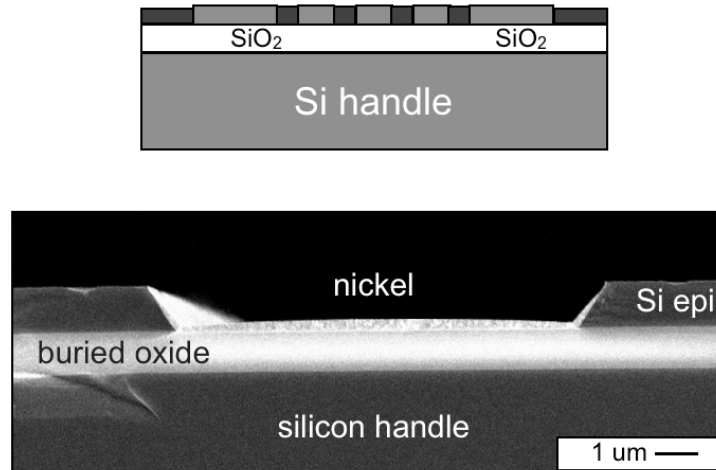


**Fig 7.6** Schematic of 2D top-down fabricated Si/Ni junction structure using SOI (top). SEM image of SOI trench filled with sputter deposited nickel.

The current-voltage characteristics of the Si/Ni junction structures are shown in Fig 7.7. The 100xN refers to the width of the Ni stripes (100μm) and the number of stripes (N = 1, 3, or 5). The S-D refers to electrical contact being made on two nickel pads ('source' and 'drain') on opposite sides of the device layer above the buried oxide. The structures exhibit double Schottky barrier behavior with current saturating with both positive and negative bias. As the number of junctions increases, the resistance of the overall device increases and the saturation current decreases.

A key requirement for accurately testing the thermoelectric properties of this structure is that the buried oxide must be electrically insulating. However, as Fig 7.8 shows, the buried oxide was conductive on an order similar to the test structure atop the oxide. Thus, current could readily flow from device layer through the buried oxide to the silicon handle before returning to the other side, bypassing the energy filtering Si/Ni junctions. The I-V curves with open symbols refer to measurements taken with contact on one of the Ni pads on the device layer and a back contact on the silicon handle wafer ('gate'). The S-G current is only about half as much as the S-D current, and thus the experiment had to be abandoned due to an inability to restrict the current to the device layer with the Si/Ni junctions.

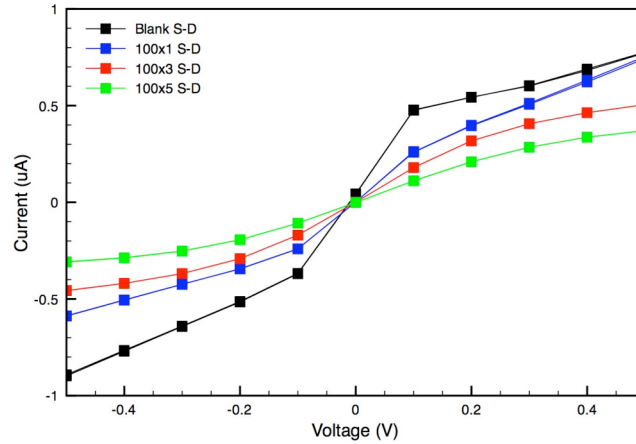


**Fig 7.7** I-V curves from S-D of Si/Ni junction structures with varying numbers of periods.

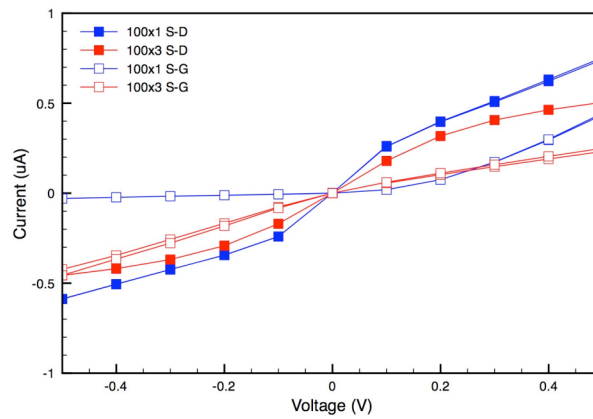


**Fig 7.8** I-V curves of two different Si/Ni junction structures measured from S-D (filled) and S-G (empty).

Although the SOI device structure was flawed, there is still potential for this material system using silicon-on-sapphire (SOS) substrates. In this case, the silicon device layer is grown on a specific plane of sapphire that results in epitaxial growth. The sapphire substrate is highly insulating and will restrict current to the Si/Ni junction structure on the device layer.

## 8 References

- Ager III, J. W., et al., *Phys. Stat. Sol. B* **245**, 873 (2008).  
Alberi, K., et al., *Appl. Phys. Lett.* **91**, 051909 (2007).  
Berman, R., *Thermal Conduction in Solids* Clarendon Press p. 47 (1976).  
Bertulis, K., et al., *Appl. Phys. Lett.* **88**, 201112 (2006).  
Cahill, D. G., et al., *J. Appl. Phys.* **93**, 793 (2003).  
Cahill, D. G., *Rev. Sci. Instrum.* **75**, 5119 (2004).  
Carlson, D. E. and Wronski, C. R., *Appl. Phys. Lett.* **28**, 671 (1976).  
Cullity, B. D. and Stock, S. R., *Elements of X-Ray Diffraction*, 3<sup>rd</sup> Ed., Prentice-Hall Inc., 167-171 (2001).  
Damodara Das, V. and Soundararajan, N., *Phys. Rev. B* **35**, 5990 (1987).  
Duda, L. C., et al., *Phys. Rev. B* **58**, 1928 (1998).  
El Khakani, M. A., et al., *Phys. Rev. B* **51**, 4903 (1995).  
Fluegel, B., et al., *Phys. Rev. Lett.* **97**, 067205 (2006).  
Foxon, C. T., et al., *Phys. Stat. Sol. (a)* **192** 441 (2002).  
Francoeur, S., et al., *Appl. Phys. Lett.* **82**, 3874 (2003).  
Gordy, W. and Orville Thomas, W. J., *J. Chem. Phys.* **24** 439 (1956).  
Hargreaves, H., Thompson, M. J., and Turner, D., *J. Non-Cryst. Sol.* **35-36**, 403 (1980).  
Haskel, D., et al., *Phys. Rev. B* **67**, 115207 (2003).  
Henini, M., et al., *Appl. Phys. Lett.* **91**, 251909 (2007).  
Ho, I., Stringfellow, G. B., *J. Cryst. Growth* **178**, 1 (1997).  
Huang, W., et al., *J. Appl. Phys.* **98**, 053505 (2005).  
Jaklevic, J., et al., *Solid State Comm.* **23**, 679 (1977).  
Janotti, A., Wei, S.-H., and Zhang, S. B., *Phys. Rev. B* **65**, 115203 (2002).  
Jones, R. E., et al., *Physica B* **376-377**, 436-439 (2006).  
Kakalios, J., Street, R. A., *Phys. Rev. B* **34**, 6014 (1986).  
Klemens, P. G., *Phys. Rev.* **119**, 507 (1960).  
Knights, J. C., Hayes, T. M., and Mikkelsen Jr., J. C., *Phys. Rev. Lett.* **39**, 712 (1977).  
Krukowski, S., et al., *J. Phys. Chem. Solids* **59**, 3 289 (1998).  
Kucheyev, S. O., Williams, J. S., Pearton, S. J., *Mater. Sci. Eng. R* **33**, 51 (2001).  
Liliental-Weber, Z., et al., *Phys. Sta. Sol. C submitted* (2012).  
Lu, H., et al., *Appl. Phys. Lett.* **77**, 2548 (2000).  
Luque, A., Marti, A., *Phys. Rev. Lett.* **78**, 5014 (1997).  
Mahan, G. D., Sofo, J. O., Bartkowiak, M., *J. Appl. Phys.* **83** 4683 (1998).  
Marasina, L. A., *Inorg. Mater.* **7**, 1444 (1971).  
Martin, J., et al., *Phys. Rev. B* **79** 115311 (2009).  
Mayer, M. A., et al., *Appl. Phys. Lett.* **97**, 022104 (2010).  
Mikkelsen Jr., J. C. and Boyce, J. B., *Phys. Rev. Lett.* **49**, 1412 (1982).  
Mikkelsen Jr., J. C. and Boyce, J. B., *Phys. Rev. B* **28**, 7130 (1983).  
Miller, N., et al., *Physica B* **404**, 4862-4865 (2009).  
Miller, N., et al., *J. Appl. Phys.* **107**, 113712 (2010).  
Mireles, F. and Ulloa, S. E., *Phys. Rev. B* **58**, 3879 (1998).  
Morimoto, A., et al., *J. Appl. Phys.* **53** 7299 (1982).

Morkoç, H., et al., *J. Appl. Phys.* **76**, 1363 (1994).

Mott, N. F. and Davis, E. A., *Electronic Processes in Non-crystalline Materials*. Oxford University Press, (1979).

Mousseau, N. and Thorpe, M. F., *Phys. Rev. B* **48**, 5172 (1993).

Newville, M., et al., *Physica B* **208**, 154 (1995).

Nordheim, L., *Ann. Physik* **9**, 607 (1931).

Novikov, S. V., et al., *J. Cryst. Growth* **247**, 35 (2003).

Novikov, S. V., et al., *J. Cryst. Growth* **311**, 3417-3422 (2009).

Novikov, S. V., et al., *J. Vac. Sci. Tech. B* **28**, C3B12 (2010).

Oe, K. and Okamoto, H., *Jpn. J. Appl. Phys.* **37**, L1283 (1998).

Ottaviani, G. and Tu, K. N., *Phys. Rev. B* **24** 3354 (1981).

Paddock, C. A., Eesley, G. L., *J. Appl. Phys.* **60**, 285 (1986).

Paul, W. H., et al., *J. Non. Cryst. Solids* **164**, 1-10 (1993).

Ravel, B. and Newville, M., *J. Syn. Rad.* **12**, 537 (2005).

Richardson, D., Hill, R., *J. Phys. C: Sol. Sta. Phys.* **5**, 821 (1972).

Ridgway, M. C., et al., *J. Appl. Phys.* **83**, 4610 (1998).

Robertson, J., *Phys. Rev. B* **33**, 4399 (1986).

Seeger, K., *Semiconductor Physics*, Springer, (2002).

Segui, Y., Carrere, F., and Bui, A., *Thin Solid Films* **92** 303 (1982).

Shan, W., et al., *Phys. Rev. Lett.* **82**, 1221 (1999).

Slack, G., et al., *J. Phys. Chem. Solids* **48**, 7 641-647 (1987).

Sorrell, C. C., Sugihara, S., Nowotny, J., *Materials for Energy Conversion Devices*, Woodhead (2005).

Spear, W. E., et al., *Appl. Phys. Lett.* **28**, 105 (1976).

Spear, W. E., *Adv. in Phys.* **26** 811 (1977).

Stern, E. A., Sayers, D. E., and Lytle, F. W., *Phys. Rev. B* **11**, 4836 (1975).

Stevenson, A. W., *Acta Cryst.* **A50**, 621 (1994).

Street, R. A. and Winer, K., *Phys. Rev. B* **40**, 6236 (1989).

Strocov, V. N., et al., *Phys. Rev. B* **72**, 085221 (1995).

Stumm, P. and Drabold, D. A., *Phys. Rev. Lett.* **79**, 677 (1997).

Stutzmann, M., Biegelsen, D. K., and Street, R. A., *Phys. Rev. B* **35**, 5666 (1987).

Tawada, Y., Okamoto, H., and Hamakawa, Y., *Appl. Phys. Lett.* **39**, 237 (1981).

Theilig, Th., Heinz, B., Ziemann, P., *J. Low Temp. Phys.* **105**, 933 (1996).

Thompson, A. G., Woolley, J. C., *Can. J. Phys.* **45**, 255 (1967).

Tixier, S., et al., *J. Cryst. Growth* **251**, 449 (2003).

Tixier, S., et al., *Appl. Phys. Lett.* **86**, 112113 (2005).

Trumbore, F. A., Gershenzon, M., and Thomas, D. G., *Appl. Phys. Lett.* **9**, 4 (1966).

Uesugi, K., Morooka, N., and Suemune, I., *Appl. Phys. Lett.* **74**, 1254 (1999).

Van de Walle, C. G. and Neugebauer, J., *J. Appl. Phys.* **95**, 3851 (2004).

Vashaee, D., and Shakouri, A., *J. Appl. Phys.* **95** 3 (2004).

Veal, T. D., McConville, C. F., Schaff, W. J., eds., *Indium Nitride and Related Alloys*, CRC Press (2010).

Vurgaftman, I. and Meyer, J. R., *J. Appl. Phys.* **94**, 3675 (2003).

Wakagi, M., Ogata, K., and Nakano, A., *Phys. Rev. B* **50**, 10666 (1994).

Wakagi, M. and Maeda, Y., *Phys. Rev. B* **50**, 14090 (1994b).

Walukiewicz, W., et al., *Phys. Rev. Lett.* **85**, 1552 (2000).

Walukiewicz, W., *Physica B*, **302-303**, 123 (2001).

Walukiewicz, W., *Physica B* **302**, 123 (2003).  
Walukiewicz, W., et al., *Physics of Dilute III-V Nitride Semiconductors and Material Systems: Physics and Technology*, edited by A. Erol, Springer-Verlag, Ch. 3 (2008).  
White, D. P., *J. Appl. Phys.* **73**, 2254 (1993).  
Williams, J. S., *Laser Annealing of Semiconductors*, Academic Press (1982).  
Williams, J. S., *Mat. Sci. Eng. A* **253**, 8 (1998).  
Wu, J., et al., *Appl. Phys. Lett.* **80**, 21 3967 (2002).  
Wu, J., et al., *Phys. Rev. B* **70**, 115214 (2004).  
Wu, J., *J. Appl. Phys.* **106**, 011101 (2009).  
Yang, J., Banerjee, A., and Guha, S., *Appl. Phys. Lett.* **70**, 2975 (1997).  
Yim, J. W. L., et al., *Phys. Rev. B* **76**, 041303(R) (2007).  
Yoshimoto, M., et al., *Jpn. J. Appl. Phys.* **42**, L1235 (2003).  
Yu, K. M., et al., *Appl. Phys. Lett.* **80**, 3958 (2002).  
Yu, K. M., et al., *J. Appl. Phys.* **94**, 1043 (2003).  
Yu, K. M., et al., *Phys. Rev. Lett.* **91**, 246403 (2003b).  
Yu, K. M., et al., *Nuc. Instr. and Met. B* **261**, 1150 (2007).  
Yu, K. M., et al., *J. Appl. Phys.* **106**, 103709 (2009).  
Yu, K. M., *Phys. Stat. Solidi. A*, **206**, 6 1168-1175 (2009b).  
Yu, K. M., et al., *Appl. Phys. Lett.* **97**, 101906 (2010).  
Zeng, G., et al., *J. Appl. Phys.* **101** 034502 (2007).  
Zhang, S. B., Wei, S., *Phys. Rev. Lett.* **86**, 1789 (2001).  
Zhukov, A. E., *Semicond. Sci. Tech.* **16**, 413 (2001).  
Zou, J., et al., *J. Appl. Phys.* **92**, 2534 (2002).  
Zubrilov, A., *Properties of Advanced Semiconductor Materials GaN, AlN, InN, BN, SiC, SiGe*, John Wiley & Sons Inc., p. 49-66 (2001).